



**Effect of synthesis parameters on the structural
characteristics and photo-catalytic activity of
ordered mesoporous titania**

Dissertation

zur Erlangung des Doktorgrades

doctor rerum naturalium (Dr. rer. nat.)

der Mathematisch-Naturwissenschaftlichen Fakultät

der Universität Rostock

vorgelegt von

Ahmed Mudhafar Mohammed

geb. am 07. November 1979, Mosul, Irak

Rostock, 2018

Gutachter:

1. Prof. Dr. Peter Langer, Institut für Chemie, Universität Rostock, Germany
2. Prof. Dr. Jennifer Strunk, Leibniz Institut für Katalyse, Rostock, Germany

Einreichung der Dissertation: 23.08.2018

Tag der öffentlichen Verteidigung: 13.11.2018

Die vorliegende Arbeit entstand in der Zeit von Juli 2014 bis August 2018 im Leibniz-Institut für Katalyse e.V. (LIKAT), Rostock.

Eidesstattliche Erklärung

Hiermit erkläre ich, dass diese Arbeit bisher von mir weder an der Mathematisch-Naturwissenschaftlichen Fakultät der Universität Rostock noch einer anderen wissenschaftlichen Einrichtung zum Zwecke der Promotion eingereicht wurde. Ich erkläre auch, dass ich diese Arbeit selbständig angefertigt und ohne fremde Hilfe verfasst habe, keine außer den von mir angegebenen Hilfsmitteln und Quellen dazu verwendet habe und die den benutzten Werken inhaltlich und wörtlich entnommen Stellen als solche kenntlich gemacht habe.

Ahmed Mudhafar Mohammed

Rostock, August 2018

Danksagung

Zuallererst möchte ich meine Worte des Dankes/ Dankesworte mit “الحمد لله رب العالمين” beginnen. Mit diesem arabischen Satz – ausgesprochen als “Alhamdo le-llah rab al-alameen” – danke ich “ALLAH”, meinem Gott. In diesem Sinne: “Alhamdo le-llah rab al-alameen”, sowohl für die Erlangung meines Doktorgrades, als auch allumfassend für alles in meinem Leben.

Tatsächlich erfuhr ich nie stärkere Unterstützung als durch meinen Betreuer Prof. Dr. Peter Langer. Ihm gebührt mein größter Dank für die Eröffnung der Möglichkeit, in Deutschland zu studieren und für seine freundschaftliche Begleitung und seinen Zuspruch. Für all dies danke ich ihm sehr.

In Hinblick auf das wissenschaftliche Thema möchte ich Dr. Norbert Steinfeldt für seine Betreuung, Unterstützung und seine Anregungen/ Überarbeitungen während meiner Zeit als Promotionsstudent meinen Dank aussprechen. Er verhalf mir dazu, eine unabhängige Person zu sein.

Insbesondere bin ich Dr. Jennifer Strunk für ihre Unterstützung und wissenschaftlichen Ratschläge dankbar.

Die größte Wertschätzung gilt allen derzeitigen und ehemaligen Mitgliedern unserer Forschungsgruppe: Dr. Heike Ehrich, Michael Sebek, Manuela Pritzkow, Dr. Elka Kraleva, und Karl Iffländer – zum einen für ihre Hilfsbereitschaft während meiner Arbeit und zum anderen für die freundliche Atmosphäre.

Tiefe Dankbarkeit kommt Michael zu. Gerne denke ich an die gemeinsame Laborarbeit zurück.

Dank gebührt zudem Dr. Ashour Ahmed, Reinhard Eckelt und Dr. Hanan Atia für ihre Hilfe und Förderung während meines Studiums.

Ich möchte Dr. Carsten Kreyenschulte, Dr. Henrik Lund, Dr. Jabor Rabeah, Dr. Nils Rockstroh, Dr. Sergey Sokolov, Dr. Stephan Bartling und Dr. Tim Peppel für die Durchführung der analytischen Messungen und für ihre Mithilfe in der Interpretation der Ergebnisse danken.

All meinen ehemaligen Lehrern, Professoren und Kollegen der Universität in Mosul bin ich dankbar.

Nicht zuletzt bin ich meiner Mutter und meinem Vater zu Dank verpflichtet, den Menschen meines Herzens. Womit auch immer ich ihnen begegne, ihr Wohlwollen ist mir sicher. In diesem Kontext kann ich ebenso die Hilfe, welche meine Frau für mich erbracht hat, nicht hoch genug wertschätzen – danke meine geliebte Frau. Zudem möchte ich meinen geliebten Kindern Omar, Fatimah und Ali, meiner lieben Schwester und meinen lieben Brüdern danken.

Allen Mitgliedern meiner Familie danke ich für ihre andauernde Unterstützung und ihre Ermutigung.

Ahmed

Acknowledgment

Before anything, I would like to start my acknowledgment with “الحمد لله رب العالمين”. This is Arabic sentence which means that I thank my God “ALLAH” and can be pronounced as Alhamdo le-llah rab al-alameen. So Alhamdo le-llah rab al-alameen not only for finishing my Ph.D. but for everything in my life.

In the fact, I didn't find people supported me like my supervisor Prof. Dr. Peter Langer. It is my pleasure to thank him so much for giving me the opportunity to study in Germany and for his kind supervision and encouragement. I am really grateful to him for everything.

With respect to the scientific issue, I would like to introduce my acknowledgement to Dr. Norbert Steinfeldt for his supervision, support, and revisions throughout my time as Ph.D. student. He planted inside me how to be independent person.

I am especially grateful to Prof. Dr. Jennifer Strunk for her support and scientific advices.

I would like to express the deepest appreciation to all the current and former members of our research group Dr. Heike Ehrich, Michael Sebek, Manuela Pritzkow, Dr. Elka Kraveva, and Karl Iffländer for their helpfulness throughout my work and for the friendly atmosphere.

Profound gratitude goes to Michael. I have very fond memories with him in the lab work.

I would like to introduce my acknowledgement to Dr. Ashour Ahmed, Mr. Reinhard Eckelt, and Dr. Hanan Atia for their helping and encouragement throughout my study.

I would like to thank Dr. Carsten Kreyenschulte, Dr. Henrik Lund, Dr. Jabor Rabeah, Dr. Nils Rockstroh, Dr. Sergey Sokolov, Dr. Stephan Bartling and Dr. Tim Peppel for performing the analytical measurements and for their assistance in the interpretation of the results.

I acknowledge all my previous teachers, professors, and colleagues in University of Mosul.

I must express my gratitude to the dearest people to my heart, they are my mother and father. Whatever I introduce to them, absolutely I cannot return back their favors to me. In the same context, I'm unable to return back sacrifices of my wife for me, so thanks my beloved wife. Also I would like thank my beloved children Omar, Fatimah and Ali, my dear sister, and my dear brothers.

To all of my family members, I would like to thank their continued support and encouragement to me.

Ahmed

Dedication

*To whom my Lord commanded me to
be very kind and obedient,
my dear parents,
I would like to dedicate them product
of this effort.*

AHMED

لمن اوصاني بهم ربي

أن أكون مطيعاً وباراً بهم

والديّ الغاليين

أحب أن أهدي لكم ثمرة جهدي

أحمد

*Im Namen von Allah, der mir den
rechten Weg wies,
widme ich diese Arbeit meinen Eltern
als Dank*

AHMED

Abstract

In this dissertation, pristine ordered, metal- (Fe, Co, and Ni), and nonmetal- (N) doped ordered mesoporous titania were synthesized via co-precipitation using the evaporation–induced self-assembly method (EISA) combined with the liquid crystal templating pathway (LCT). In addition, for un-doped mesoporous TiO₂, various parameters were systematically varied including solvent evaporation temperature, surfactant extraction conditions, molar surfactant/titanium ratio, and titanium source. In order to investigate the doping effect on the structural characteristics, different analysis and characterization techniques were employed to characterize and describe structural, morphological and physicochemical properties of the synthesized materials. These techniques involved SAXS, TEM, XRD, XPS, EPR, UV/Vis DRS, ATR-IR, TG/DSC, and N₂ physisorption. Moreover, the photocatalytic activity of the synthesized materials was evaluated in the photodegradation of phenol under various irradiation sources.

Zusammenfassung

In der vorliegenden Arbeit wurde geordnetes mesoporöses sowie geordnetes Metall- (Fe, Co und Ni) und Nichtmetall-dotiertes (N) mesoporöses Titandioxid durch eine verdampfungs- induzierte Selbstanordnung in Kombination mit einem Flüssigkristalltemplat hergestellt. Bei der Herstellung des undotierten Titandioxids wurden verschiedene Herstellungsparameter wie z.B. die Lösungsmittelverdampfungstemperatur, die Bedingungen der Tensidextraktion, das molare Tensid/Titanverhältnis und die eingesetzte Titanverbindung systematisch variiert. Um den Einfluss der Präparationsparameter und der Dotierung auf die strukturellen, morphologischen und physikalisch-chemischen Eigenschaften zu ermitteln, wurden die hergestellten Proben mittels verschiedener, sich ergänzender Methoden charakterisiert. Folgende Methoden kamen dabei zum Einsatz: SAXS, TEM, XRD, XPS, EPR, UV/Vis DRS, ATR-IR, TG/DSC, und N₂-Physisorption. Die Testung der photokatalytischen Aktivität der hergestellten Materialien erfolgte am Beispiel der Phenolzersetzung unter Verwendung unterschiedlicher Bestrahlungsquellen.

List of Abbreviations

Ammonium hydroxide	NH ₄ OH
Amphiphilic block co-polymers	ABCs
Annular Bright Field	ABF
Atomic absorption spectroscopy	AAS
Attenuated total reflection infrared spectroscopy	ATR-IR
Beta titanium dioxide	β-TiO ₂
Bismuth	Bi
Brunauer–Emmett–Teller (BET) theory	BET
Carbon dioxide	CO ₂
Cetyl trimethyl ammonium bromide	CTAB
Cobalt acetate	Co(CH ₃ COO) ₂
Cobalt chloride hexahydrate	CoCl ₂ ·6H ₂ O
Concentration of phenol	C ₀ (M)
Conduction band	CB
Copper	Cu
Copper ion (I)	Cu ¹⁺
Copper nitrate trihydrate	Cu(NO ₃) ₂ ·3H ₂ O
Degree Celsius	°C
Titanium dioxide P25, nanopowder, ~21 nm	P25
Differential scanning calorimetry	DSC
Dimethyl formamide	DMF
Drag reduction system	DRS
Electron paramagnetic resonance	EPR
Entrepreneurs' Organization	EO
Energy dispersive X-ray spectrometer	EDXS

Evaporation induced self-assembly	EISA
Ferrous sulphate heptahydrate	$\text{FeSO}_4 \cdot \text{H}_2\text{O}$
High Angle Annular Dark Field	HAADF
High performance liquid chromatography	HPLC
Hydrazine	N_2H_4
Hydrochloric acid	HCl
Hydrolytic sol-gel method	HSG
Hydroxyl ion	OH^-
Hydrogen peroxide	H_2O_2
Hydroxyl radical	OH^\bullet
International Center of Diffraction Data	ICDD
International Union of Pure and Applied Chemistry	IUPAC
Integral breadth in radians	β
Iron(III)chloride	FeCl_3
Iron(III)nitrate	$\text{Fe}(\text{NO}_3)_3$
Initial concentration of phenol at the time	C_t
Kubelka-Munk function	$F(R)$
Liquid crystal templating	LCT
Methane	CH_4
Methyl orange	MO
Methylene blue	MB
Nickel(II)chloride	NiCl_2
Nonhydrolytic sol-gel route	NSG
One-dimensional structure	1D
Oxidized nitrogen	NO_x
Phenol	$\text{C}_6\text{H}_5\text{OH}$
Polystyrene	PS

Polyacrylamide	PAM
Polyethylene glycol	PEG
Polytetrafluoroethylene	PTFE
Potassium hexafluorotitanate	K_2TiF_6
Positive hole	h^+_{VB}
Powder X-ray diffraction	XRD
Poly(ethylene oxide)	PEO
Poly(propylene oxide)	PPO
Pulsed laser deposition	PLD
Rate constant	k
Room temperature	RT
Scanning electron microscope	SEM
Scanning transmission electron microscopy	STEM
scattering vector (nm^{-1})	q
Small-angle X-ray scattering	SAXS
Stearidonic acid	SDA
superoxide	$\text{O}_2^{\bullet-}$
Tetrabutyl titanate	$\text{C}_{16}\text{H}_{36}\text{O}_4\text{Ti}$
Tetrahydrofuran	THF
Three dimensional structures	3D
Thermogravimetric analysis	TGA
Ti-aquo	$[\text{Ti}(\text{OH}_2)]_4^+$
Ti-hydroxo	$[\text{Ti}-\text{OH}]_{(4-1)}^+$
Titania	TiO_2
Titanium alkoxides	$\text{Ti}(\text{OR})_4$
Titanium butoxide	$\text{Ti}(\text{O}^i\text{Bu})_4$
Titanium chloride	TiCl_4

Titanium ion (IV)	Ti^{4+}
Titanium isopropoxide	$\text{Ti}(\text{Pr}^i\text{O})_4$
Titanyl oxalate complex	$[\text{TiO}(\text{C}_2\text{O}_4)_2]^{2-}$
Transmission electron microscopy	TEM
Triblock copolymer Pluronic	P123
Tricobalt tetraoxide	Co_3O_4
Two-dimensional structure	2D
Ultraviolet irradiation	UV
Ultraviolet/Visible light spectroscopy	UV/Vis
Valence band	VB
X-ray photoelectron spectroscopy	XRD
wavelength (nm)	λ
Zero-dimensional structure	0D

Table of Contents

1	Introduction.....	1
1.1	Titanium dioxide	1
1.2	Porous materials	2
1.2.1	Mesoporous titanium dioxide powder	2
1.2.2	Doping mesoporous titanium dioxide powder	5
1.2.2.1	Metal-doped mesoporous titanium dioxide powder.....	6
1.2.2.2	Nitrogen doped mesoporous titanium dioxide powder	8
1.3	Ordered mesoporous materials.....	10
1.3.1	Ordered mesoporous titanium dioxide powder.....	11
1.3.2	Doping ordered mesoporous titanium dioxide powder.....	16
1.3.2.1	Metal-doped ordered mesoporous titanium dioxide powder	16
1.3.2.2	Non-metal doped ordered mesoporous titanium dioxide powder	18
1.4	Principles of photocatalysis.....	18
1.5	Photoactivity of mesoporous titanium dioxide powder.....	19
1.5.1	Photoactivity of undoped-mesoporous titanium dioxide powder	19
1.5.2	Photoactivity of doped-titanium dioxide powder	20
1.5.2.1	Photoactivity of metal-doped mesoporous titanium dioxide powder ...	20
1.5.2.2	Photoactivity of non-metal-doped mesoporous titanium dioxide powder	22
1.6	Photoactivity of ordered mesoporous titanium dioxide powder	23
1.6.1	Photoactivity of pristine mesoporous titanium dioxide powder	23
1.6.2	Photoactivity of doped ordered mesoporous titanium dioxide powder	24
1.6.2.1	Photoactivity of metal-doped ordered mesoporous titanium dioxide powder	24
1.6.2.2	Photoactivity of non-metal-doped ordered mesoporous titanium dioxide powder	25
1.7	Photocatalytic mechanism.....	25

1.8	Phenol as pollutant	26
1.9	Objectives and structural planning	28
2	Experimental part.....	30
2.1	Material synthesis.....	30
2.1.1	Materials	30
2.1.2	Synthesis of pristine mesoporous titania.....	30
2.1.2.1	General synthesis procedure	30
2.1.3	Synthesis of metal-doped mesoporous titania.....	31
2.1.4	Synthesis of nitrogen-doped mesoporous titania	32
2.1.5	Photocatalytic degradation of phenol in aqueous solution	34
2.1.5.1	Experiments with a Mercury lamp	34
2.1.5.2	Experiments with a Xenon lamp	35
2.2	Characterization	36
2.2.1	Small-angle X-ray scattering (SAXS)	36
2.2.2	Transmission electron microscopy (TEM)	36
2.2.3	Powder X-ray diffraction (XRD)	37
2.2.4	X-ray photoelectron spectroscopy (XPS)	37
2.2.5	N ₂ physisorption measurement	38
2.2.6	UV-Vis spectroscopy (UV/Vis)	38
2.2.7	Electron paramagnetic resonance (EPR)	38
2.2.8	Attenuated total reflection infrared spectroscopy (ATR-IR)	38
2.2.9	Thermogravimetric analyses (TGA) and differential scanning calorimetry (DSC) measurements	38
3	Results and discussion	39
3.1	Pristine ordered mesoporous titanium dioxide.....	39
3.1.1	Variation of synthesis parameters.....	39
3.1.1.1	Evaporation temperature	39
3.1.1.2	Surfactant extraction conditions.....	48

3.1.1.3	Molar surfactant/titanium ratio	53
3.1.1.4	Changing of titanium source	55
3.1.2	Photocatalytic activity of the prepared materials.....	58
3.2	Doped ordered mesoporous titanium dioxide	61
3.2.1	Metal-doped ordered mesoporous titanium dioxide	61
3.2.2	Structural characteristics	61
3.2.3	Photocatalytic activity of metal doped mesoporous titanium dioxide	69
3.3	Nitrogen doped ordered mesoporous titania	74
3.3.1	Effect of the temperature	77
3.3.2	Influence of the heating rate	88
3.3.3	Influence of the presence of water vapor	91
4	Summary and Conclusions	95
5	Appendix.....	99
6	References.....	111

List of Figures

Figure 1. Schematic diagram showing the main methods for the synthesis of mesoporous TiO ₂ .	3
Figure 2. Schematic diagram showing the valence and conduction bands of un-doped and N-doped TiO ₂ .	9
Figure 3. Schematic diagram showing common sol-gel technique used in synthesis ordered mesoporous TiO ₂ .	13
Figure 4. Schematic diagram showing procedures synthesis of ordering mesoporous titania.	16
Figure 5. Comparison of energetic level of titania VB and CB band with the redox potential of different processes.	19
Figure 6. mechanism of <i>hν</i> 1: pristine, <i>hν</i> 2: metal-doped and <i>hν</i> 3: nonmetal-doped TiO ₂ photocatalysis .	26
Figure 7. Schematic diagram showing the probable degradation mechanism for phenol.	28
Figure 8. Schematic diagram showing structural planning of the dissertation.	29
Figure 9. Schematic diagram showing experimental set up for treatment of amorphous mesoporous TiO ₂ with gaseous ammonia.	32
Figure 10. Photos of the experimental set up used for the degradation of phenol with mesoporous titania using a) Mercury lamp and b) Xenon lamp.	35
Figure 11. Influence of the solvent evaporation temperature on the SAXS patterns recorded at different steps of material synthesis A) after ammonia treatment, B) after surfactant removal, C) after thermal treatment; and D) influence of single synthesis step on d100 spacing.	40
Figure 12. STEM-HAADF images of the material where the solvent was evaporated at 40 °C (A,B,C) and 70 °C (D,E,F), respectively; (A,D) after treatment of the sol with ammonia, (B,E) after surfactant extraction, and (C,F) after thermal treatment .	42
Figure 13. XRD powder patterns of samples synthesized with different evaporation temperature thermal treatment.	43
Figure 14. A) Adsorption-desorption isotherms of calcined titania materials synthesized with different evaporation temperature and B) Pore size distribution obtained by BJH method.	44
Figure 15. UV/Vis Spectra of samples synthesized with different solvent evaporation temperature after thermal treatment.	45
Figure 16. High resolution XPS spectra from calcined material synthesized with solvent evaporation temperature of 60 °C A) N 1s and B) C1s.	46
Figure 17. Influence of the repetition of synthesis mesoporous TiO ₂ on the SAXS patterns A) after ammonia treatment, B) after surfactant removal, C) after thermal treatment.	47
Figure 18. SAXS pattern of the sample synthesized without gel aging time of 15 h.	48
Figure 19. A) SAXS patterns and B) Nitrogen adsorption–desorption isotherms for the powders without surfactant P123 extraction (TiO ₂ -W) and with surfactant P123 extraction (TiO ₂ -E).	49

- Figure 20.** Simultaneous TG/DSC curves in compressed air atmosphere A) for the materials P123/Ti(OⁱPr)₄ (molar ratio: 0.0163) before and after extraction using ethanol (temperature of extraction: 78 °C, stirred at 300-rpm) and B) for P123/Ti(OⁱPr)₄ (molar ratio: 0.0163) after a) first, b) second, c) third, d) fourth extraction. 50
- Figure 21.** Simultaneous TG-DSC curves of the material molar ratio P123/Ti(OⁱPr)₄ (molar ratio: 0.0163) after two extraction at different temperatures, A(a-d): under N₂ and 19B(a-d): air atmosphere. 51
- Figure 22.** A) SAXS patterns and B) Nitrogen adsorption–desorption isotherms of the materials after calcination prepared with different extraction temperatures. 51
- Figure 23.** Influence of the number of extraction steps on the SAXS patterns A) after surfactant removal B) after calcination. 53
- Figure 24.** SAXS patterns of TiO₂ prepared with different molar P123/Ti(OⁱPr)₄ ratios (Tevap = 40 °C) A) after surfactant extraction (T_{extrac} = 78 °C (4 times)), B) after calcination. 54
- Figure 25.** SAXS patterns for the materials prepared with different mol ratio P123/Ti(OⁿBu)₄ after surfactant extraction A), and after thermal treatment B). 56
- Figure 26.** Influence of reaction time on phenol concentration for titania samples synthesized with different molar ratio of P123/Ti(OⁱPr)₄ under UV irradiation with 1.2 °/min. 58
- Figure 27.** Influence of reaction time on phenol concentration for titania samples synthesized with different solvent evaporation temperature at irradiation with white light A) and visible light, λ > 420 nm B). 59
- Figure 28.** Influence of reaction time on phenol concentration for titania samples synthesized with different surfactant extraction temperatures (4 times) - A) and with Ti(OⁿBu)₄ as Ti source - B); Xenon lamp, visible light λ > 420 nm. 60
- Figure 29.** SAXS patterns pristine and doped titania prepared with 0.5 (A, C, and E) and 5 mol% metal (B, D and F) after different synthesis steps: (A, B) after treatment with NH₃ gas - step c, (C, D) after treatment in boiling ethanol – step d, and (E, F) after thermal treatment at 450 °C – step e. 62
- Figure 30.** STEM-HAADF images of titania doped with 0.5 mol% metal after thermal treatment, A) Fe, B) Co, C) Ni. 63
- Figure 31.** STEM-HAADF images of titania samples doped with 5 mol% metal after thermal treatment, A) Fe, B) Ni. 64
- Figure 32.** XRD patterns of calcined mesoporous titania prepared with A) 0.5 and B) 5 mol% doping metal; a)- pristine, b) Fe, c) Co and d) Ni. 65
- Figure 33.** . Pore size distribution of doped mesoporous titania calcined at 450 °C, A) 0.5 mol% metal, and B) 5 mol% metal. 66
- Figure 34.** EPR spectra of the calcined mesoporous titania doped with iron (the spectra were recorded at 295 K). 67
- Figure 35.** UV-Vis diffuse reflectance spectra (DSR) of calcined un-doped mesoporous TiO₂ and doped mesoporous TiO₂ prepared with a) 0.5 and b) 5 mol% metal. 68
- Figure 36.** Degradation of phenol under UV irradiation as function of time, A) samples doped with 0.5 mol% metal and B) samples doped with 5 mol% metal. 71
- Figure 37.** Degradation of phenol under Xenon lamp as function of time samples doped with 0.5 mol% metal A) and B) samples doped with 5 mol% metal. 72

- Figure 38.** Influence of reaction time on phenol concentration for titania doped with 0.5 mol % Fe A) repeated synthesis (Xenon lamp without filter) and B) two tests of the same material under identical conditions ($\lambda > 420$ nm). 73
- Figure 39.** A) XRD powder patterns and B) SAXS patterns of am-TiO₂) and of TiO₂-Ar/O₂ (am-TiO₂ after heating under Ar, 22-450 °C/6.5 h followed from treatment under O₂ (450 °C, 2 h)). 74
- Figure 40.** STEM-HAADF A) of am-TiO₂ and B) of TiO₂-Ar/O₂ (am-TiO₂ after heating under Ar followed from treatment in oxygen atmosphere (Ar: 22-450 °C/6.5 h followed from treatment under O₂ atmosphere (450 °C, 2 h)). 75
- Figure 41.** A) UV/vis spectra and B) ATR-IR spectra of titania obtained after surfactant extraction (am-TiO₂) and after calcination (TiO₂-Ar/O₂, 22-450 °C/6.5 h, followed from oxygen treatment (450 °C, 2 h)). 76
- Figure 42.** HR XPS spectra from am-TiO₂, A) Ti2p, B) O1s, C) C1s, and D) N1s. 77
- Figure 43.** A) XRD powder patterns and B) SAXS patterns of am-TiO₂ samples heated under NH₃ atmosphere using different heating temperatures 350, 450, and 550 °C. 78
- Figure 44.** STEM-HAADF images of A) N-TiO₂-450NH₃ obtained after heating under NH₃ atmosphere at 450 °C and B) N-TiO₂-450NH₃/O₂ (sample was obtained after successive heating O₂ (450 °C, 2 h)). 79
- Figure 45.** Sample N-TiO₂-450NH₃ A) STEM-HAADF image with marked area used for spectrum C, B) HAADF overlaid with elemental maps of Ti, O, and N. C) The EELS spectrum showed the presence of nitrogen on the surface of TiO₂. 79
- Figure 46.** A) ATR-IR spectra of am-TiO₂ samples heated under NH₃ atmosphere using different heating temperatures and B) UV/vis absorption spectra. 80
- Figure 47.** HR XPS spectra from am-TiO₂ after heating in NH₃ to 450 °C, A) Ti2p, B) O1s, C) C1s, and D) N1s. 82
- Figure 48.** A) XRD patterns and B) SAXS patterns of samples calcined under NH₃ using different heating temperatures followed from successive oxygen treatment (450 °C, 2 h). 83
- Figure 49.** A) ATR-IR spectra and B) UV/Vis absorption spectra of samples heated under NH₃ using different heating temperatures followed from successive oxygen treatment (450 °C, 2 h). 84
- Figure 50.** HR XPS spectra from am-TiO₂ after heating in NH₃ to 450 °C (N-TiO₂-450NH₃) followed from successive treatment in oxygen atmosphere (450 °C/2 h), A) Ti2p, B) O1s, C) C1s, and D) N1s. 85
- Figure 51.** Degradation of phenol under Xenon lamp irradiation as function of time for samples heated under NH₃ at 450 °C A) white light and B) visible light ($\lambda > 420$ nm). 86
- Figure 52.** Degradation of phenol under Xenon lamp irradiation as function of time for samples heated under NH₃ at different heating temperatures followed from treatment in oxygen atmosphere (450 °C, 2 h), A) white light and B) visible light ($\lambda > 420$ nm). 87
- Figure 53.** A) XRD powder pattern of am-TiO₂ treated with ammonia at different heating rates (0.6, 1.2, and 2.4 °C/min) and B) SAXS patterns obtained after a successive treatment with oxygen (450 °C, 2 h). 88

Figure 54. A) SAXS patterns of am-TiO₂ treated with ammonia at different heating rates (0.6, 1.2, and 2.4 °C/min) and B) SAXS patterns obtained after a successive treatment with oxygen (450 °C, 2 h). 89

Figure 55. A) UV/vis spectra of am-TiO₂ treated with ammonia at different heating rates (0.6, 1.2, and 2.4 °C/min) and B) UV/vis spectra obtained after a successive treatment with oxygen (450 °C, 2 h). 90

Figure 56. Degradation of phenol as function of time under Xenon lamp irradiation for samples obtained using different heating rates (0.6, 1.2, and 2.4 °C/min) under NH₃ atmosphere followed from successive treatment under oxygen (450 °C, 2 h); A) white light and B) visible light $\lambda > 420$ nm. 91

Figure 57. A) XRD patterns and B) SAXS patterns of the am-TiO₂ after heating the sample under gas mixture of NH₃, N₂, and water vapor. 92

Figure 58. A) UV/vis spectra and B) phenol degradation of as function of time under Xenon lamp irradiation (white light) for samples heated under mixture of NH₃, N₂, and water vapor. 93

Figure 59. HR XPS spectra from am-TiO₂ after heating in NH₃ /N₂ /H₂O to 450 °C, A) Ti2p, B) O1s, C) C1s, and D) N1s. 94

List of Tables

Table 1. Amount of metal source that was used in the synthesis of metal doped titania.	31
Table 2. Summary of the structure characteristics for materials synthesized with different solvent evaporation temperatures (molar P123/Ti(O ⁱ Pr) ₄ ratio = 0.0163, calcination at 450 °C).	44
Table 3. Summary of the structure characteristics for materials synthesized with different molar P123/Ti(O ⁱ Pr) ₄ ratio after calcination.	52
Table 4. Summary of the structure characteristics for materials synthesized with different molar P123/Ti(O ⁱ Pr) ₄ ratio after calcination.	55
Table 5. Structural characteristics of titania prepared with Ti(O ⁿ Bu) ₄ .	57
Table 6. Characteristics of calcined TiO ₂ doped with 0.5 or 5 mol% metal.	66
Table 7. Comparison of pseudo first order rate constants in phenol degradation over doped mesoporous titania under UV irradiation.	71
Table 8. Comparison of pseudo first order rate constants in phenol degradation over doped mesoporous titania under Xenon lamp.	73
Table 9. General characteristics for samples obtained after heating under NH ₃ at different temperatures and after following treatment in oxygen flow (450 °C, 2 h).	81
Table 10. General characteristics of samples prepared with different heating rate under NH ₃ atmosphere and following treatment with oxygen (450 °C, 2 h).	89
Table 11. General characteristics for samples heated under a mixture of NH ₃ , N ₂ , and water vapor.	92

1 Introduction

1.1 Titanium dioxide

Titania or titanium dioxide (TiO_2) is one of the most popular semiconductor materials that attract great attention. Moreover, titania has been utilized over the past years as an excellent photocatalyst in a wide range of energy and environmental applications such as the photocatalytic degradation of air pollutants, air and water purification, water disinfection, medical applications, printing, optics, sensors, batteries, photoelectrochemical cell, energy conversion and water splitting [1-10]. This is because of its strong oxidizing power, photostability, chemical and biological inertness, excellent electronic and optical properties, environmentally friendly and low cost etc. [11-14]. It was first produced commercially in 1923 [15]. In 1972, it was first discovered by Fujishima and Honda as an active photocatalyst [16].

TiO_2 naturally exists in an amorphous or a crystalline phase. The crystalline titania have three different major crystallographic phases in nature involving anatase (tetragonal), rutile (tetragonal), and brookite (orthorhombic) [17]. Moreover, it has a special phase $\beta\text{-TiO}_2$ (monoclinic), which is less known compared to the others [18]. These forms exhibit different physical and chemical properties enabling different functionalities [19, 20]. Generally, in a photo-catalytic study anatase appears to have the highest photoactivity compared to the others due to the large surface area per unit mass and volume [21]. In addition, anatase exhibits an indirect band gap, which is smaller than its direct band gap [22]. Recent study showed that the high performance of photocatalytic reduction of CO_2 due to forming a heterojunction between two crystal phases, anatase and phase $\beta\text{-TiO}_2$. This could be promoted the separation of electron-hole pairs and prolong its lifetime [23].

Regarding the nanostructure, TiO_2 forms different geometric structural design such as spheres as a zero-dimensional structure (0D), fibers and tubes as one-dimensional structure (1D), nanosheets as a two-dimensional structure (2D), and interconnected architectures as three dimensional structures (3D) [9]. Moreover, it exhibits several morphologies such as powders, nanoparticles and films [24]. Diverse morphologies could result in various properties for different applications [25]. For photocatalytic and photovoltaic applications, high specific surface area, controllable pore size and morphology, and good interparticle connectivity for titania are desired properties [26, 27]. These vital properties could be

simultaneously achieved by using titania with an ordered crystalline mesoporous framework. Most of reported works on ordered mesoporous TiO₂ are focused on films [26, 28-32].

1.2 Porous materials

Mainly, porous materials can interact with wide range of chemical systems including atoms, ions, molecules, and nanoparticles at their surfaces and also through their bulk. This interaction leads to much attention and interest for porous materials. Moreover, the presence of pores in nanostructured materials can dramatically enhance their physical and chemical properties [33, 34].

According to convention of the International Union of Pure and Applied Chemistry (IUPAC), porous materials can be classified into three types based on their pore diameter. These are microporous (pore diameter < 2 nm), mesoporous (2-50 nm) and macroporous (> 50 nm) materials [35]. Mesoporous transition metal oxides are of great interest because they exhibit both intrinsic optical and electronic properties of transition metal oxides and the advantages of mesopores [24]. The mesoporous TiO₂ is one of the most important semiconductor materials (transition metal oxides) that shows a great potential in versatile applications. In recent years, mesoporous TiO₂ has received special attention for photocatalytic and photovoltaic application due to its high specific surface area, controllable pore size and morphology, and high antiparticle connectivity [26].

1.2.1 Mesoporous titanium dioxide powder

Mesoporous TiO₂ as photocatalyst has been synthesized by different methods such as sol-gel, hydrothermal, solvothermal, microwave, sonochemical, and electrodeposition synthesis (for details, see Figure 1) [3, 36]. Sol-gel technology have been used for the first time by Ebleman in 1846 [37]. This method is applied commercially in many applications, such as forming coatings on window glass, powders and fibers [38]. It is also used to synthesize photo-catalyst powders or thin films [17]. The chemistry involved in this method is based on inorganic polymerization reactions. Two important reactions, hydrolysis and condensation, are included here that lead to the formation of M-OH-M or M-O-M bridges. The sol-gel technology has major advantages such as inexpensive, easy to operate, ambient temperature of sol preparation and gel formation, better homogeneity, better control of the structure, including porosity and particle size, and the highly pure resulting product [39]. In contrast, the main disadvantage for this method is that the products are mostly amorphous and need hydrothermal treatment or calcination for the crystallization process [40]. In addition

titania suffers fast hydrolysis and condensation reactions resulting in poorly structured and even non-porous materials.

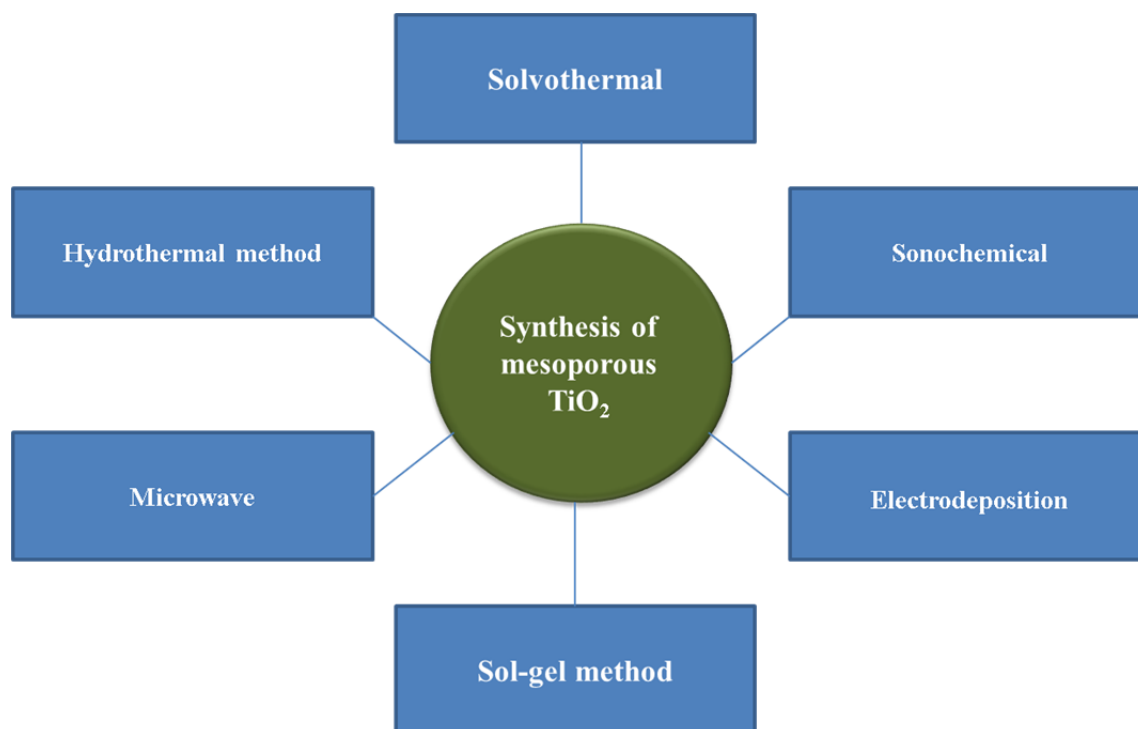


Figure 1. Schematic diagram showing the main methods for the synthesis of mesoporous TiO₂.

Furthermore, mesoporous TiO₂ has been synthesized by combining sol-gel chemistry with surfactants [41]. In this process, the micelle formation and their organization is driven by solvent evaporation that is known as evaporation induced self-assembly (EISA) [42]. EISA process is one of the most essential synthetic methods, which has extensively been employed for obtaining a wide variety of mesoporous morphologies (e.g., aerosol, monoliths, films, and powders) [43]. This is due to the use of very dilute initial conditions that leads to a gradual formation of the liquid crystalline mesophase upon the solvent evaporation [44]. During the sol-gel synthesis, it is not easy to control the reactivity of the titanium precursors due to their high tendency to hydrolyze and to form the TiO₂ precipitate without the mesopores formation [24, 42]. Therefore, controlling the sol-gel procedures is the most critical issue for this technique. The liquid crystal templating (LCT) mechanism clarifies this process with a stabilized non-ionic surfactant mesophase which is representing as a template for the condensation of the inorganic phase. The templates lead to spontaneous co-assembly of both materials in a mesostructured phase. The templates play key roles in modulating the mesostructure, surface area, pore size, and wall thickness and thermal stability of the mesoporous TiO₂ [34]. Effects of the surfactant concentration on synthesis of the mesoporous

titania were studied by Benkacem and his colleagues [45]. They noted that increasing of amount cetyl trimethyl ammonium bromide (CTAB) surfactant increased considerably titania pore diameters while decreased its porous volume and specific surface area. Titanium oxo-polymers can be obtained through hydrolysis and condensation of the titania molecular precursors such as titanium alkoxides Ti(OR)_4 [46].

Mainly, most works have been focusing on synthesis of the mesoporous TiO_2 . The first mesoporous TiO_2 powder with highly organized hexagonal pore structure has been synthesized by Antonelli and Ying in 1995. They employed the modified sol-gel method with the phosphate surfactant templating chemistry [47]. Mesoporous anatase with large pore size of $\sim 7\text{--}8$ nm and very narrow pore size distribution has been synthesized by Kartini et al. [48]. This has been performed via a neutral route of hydrothermally templated anatase seeds. This two-step process produces a material with a fully anatase crystalline domain. The block copolymer restrains the pore formation as well as the crystal growth. Tuning the hydrothermal temperature in the self-assembly process controls the pore size.

The roles of hydrochloric acid in the synthesis of mesoporous titania have been clarified by Anpo's group [49]. They explained three important roles including a) enhancing the interaction between inorganic framework and organic template, b) hindrance the gelatination of titania oligomers, and c) promotion the growth of crystalline particles. Moreover, they also explained the effects of H^+/Ti molar ratio on the formation of mesoporous structure and the phase transition. The high H^+/Ti ratio improved the mesopores and promoted the formation of rutile more than anatase after 623 K thermal treatment. Tanaskovic et al. [50] have synthesized the mesoporous titania with well-crystallized anatase phase by nonhydrolytic sol-gel process combined with solvothermal gel. Titania powder was obtained by calcination of the gel sample. They showed that increasing the gelation time does not increase the crystallinity of the dry gels. Moreover, they determined a correlation between the crystallite and the mesopore size: as the crystallite increase, intercrystallite voids increase. This explains the possibility of controlling the porosity by changing the crystallite size through varying the gelation temperature and time.

Swapana et al. [51] synthesized the mesoporous titania nanoparticles using simple and cost-effective sol-gel technique by ultrasonic irradiation. Ultrasonic irradiation reduced the sol-gel reaction time, led to uniform size distribution, and improved the phase purity. Their XRD results showed the formation of high purity anatase titania nanoparticles with a size of

19.9 nm. Their SEM analysis revealed the agglomeration of the titania nanoparticles. The synthesized titania showed an indirect bandgap of 3.25 eV for the anatase phase.

In 2016, Zi et al. [52] synthesized mesoporous titania by a new method of photodegradation to remove the organic surfactant template (CTAB). Their results showed the ability of UV light to degrade the surfactant template to form mesoporous titania with high surface area (203 m²/g). Further calcination treatment was done to transform the amorphous TiO₂ to the crystalline anatase phase.

Recently, Zhang and co-workers [40] fabricated mesoporous TiO₂ with high crystalline form and large surface area. This has been done by using a fast sol-gel method combined with two-step calcination process (powder was calcined at 500-700 °C in nitrogen, and then recalcined at 500 °C in air). They used polyacrylamide (PAM) and polyethylene glycol (PEG) as composite templates. Their results showed that PAM accelerated the gel rate. When calcined in nitrogen, PEG was converted into amorphous carbon that prevented the mesostructure from collapsing when titania heated to the temperature required to get high crystallinity and high specific surface between 78.5 - 110.7 m²/g area. The average crystallite sizes of samples is about 7-12 nm.

1.2.2 Doping mesoporous titanium dioxide powder

Doping technique refers to introducing the impurity atoms into the semiconductor lattice to improve the conductivity [53]. It is one the most promising techniques to extend the light-absorbing properties of TiO₂. In addition, the doping process leads to reduced electron-hole recombination rate, low band gap, improved TiO₂ morphology, high crystallinity, high surface area, and improved photocatalytic activity [54, 55]. TiO₂ anatase has a wide band gap of ca. 3.2 eV due to its activity only under the ultraviolet irradiation (UV) [56].

Considerable efforts have been employed towards different strategies to extend the visible light activity of TiO₂ via modification of its electronic and optical properties, as well as surface and interface modification, thereby enhancing its photocatalytic properties. These strategies include the controlling of the morphology and particle size, composite or coupling materials, transition metals doping, non-metals, noble metals deposition, and surface sensitization, etc. [53, 57]. Among these strategies, doping has been the most promising approach for modification the photo response of TiO₂.

1.2.2.1 *Metal-doped mesoporous titanium dioxide powder*

The doping of metal ions into TiO_2 matrix can be classified into three kinds, which includes the doping with transition metal ions, rare-earth metal ions, and poor metal ions (post-transition metals such as aluminum and bismuth) [57]. TiO_2 doped with various types of suitable transition metals (such as iron, cobalt, nickel etc.) can produce impurity states between the valance and conduction bands of TiO_2 . This decreases the band gap and thus increases the photo efficiency of TiO_2 [58]. Generally, mesoporous TiO_2 doped with metal has been synthesized by several methods including the sol-gel method, impregnation, metallization, precipitation, hydrothermal process, solvothermal synthesis, flame spray pyrolysis, ultra sound assisted methods, and addition of transition metal to the substrate solution.

There are a lot of scientific research articles focusing on the transition metal doped TiO_2 . Among these metals, Fe has attracted special attention due to its ionic radius of Fe^{3+} (0.64\AA) that is similar to that of Ti^{4+} (0.68\AA). This leads to an easier incorporation of Fe^{3+} into the TiO_2 crystal structure lattice. In 2005, Fe-doped mesoporous TiO_2 nanocrystalline powders and films were synthesized by Zhou et al. via the sol-gel method [59]. They employed tetrabutyl titanate (TBOT) ($\text{Ti}(\text{OC}_4\text{H}_9)_4$) as titanium precursor and ferric nitrate ($\text{Fe}(\text{NO}_3)_3$) as iron source. They showed that Fe-doping influenced the crystallization, specific surface area, pore structures and photocatalytic activity of mesoporous TiO_2 powders. Moreover, the sol-gel method and hydrothermal treatment have been employed to Fe-doped mesoporous TiO_2 powder by Anpo's group [60]. XRD, EPR, AAS, and XPS characterization demonstrated that Fe^{3+} could substitute Ti^{4+} in the TiO_2 lattice and its concentration decreased from the surface to the center of the doped TiO_2 . They found that the actual bulk Fe^{3+} content determined by AAS is a little lower than the nominal one and far lower than surface Fe^{3+} content determined by XPS. They supposed that firstly Fe^{3+} could be adsorbed mostly and strongly on the surface of TiO_2 dried gels due to their very large surface area and strong electrostatic interaction and then Fe^{3+} may diffuse gradually into the bulk during hydrothermal treatment.

Zhu et al. [61] have reported the synthesis of Fe-doped TiO_2 by using a facile nonhydrolytic sol-gel route (NSG) and hydrolytic sol-gel method (HSG). They used titanium chloride (TiCl_4) as titanium source and iron nitrate ($\text{Fe}(\text{NO}_3)_3$) as iron source. They demonstrated that the NGS method is superior the HSG owing to the controllable reaction rate and lack of surface tension. This ensures the formation of mesoporous and well-crystallized

anatase in the Fe-TiO₂ form. In 2012, Shouqiang et al. [62] synthesized Fe-doped mesoporous TiO₂ powder with specific surface area of 117.6 m²/g by the sol-gel method with Ti(SO₄)₂ as a raw material. Their results showed that Fe³⁺ and Fe²⁺ replaced Ti⁴⁺ and entered into the TiO₂ lattice.

Furthermore, effect of the titanium precursor type on the photocatalytic properties of the Fe-doped mesoporous TiO₂ powder and its physical properties has been studied by Goswami et al. [63]. They synthesized mesoporous Fe-doped TiO₂ nanoparticles with an anatase phase by the sol-gel method using a stable precursor potassium hexafluorotitanate (K₂TiF₆) as titanium source for the first time. Ferrous sulphate heptahydrate (FeSO₄·7H₂O) and ferric nitrate (Fe(NO₃)₃·9H₂O) have been used for doping TiO₂ with Fe (III).

Piumetti et al. [64] synthesized two metals (iron or vanadium)-doped mesoporous TiO₂ powder by slightly modifying the hydrothermal assisted sol-gel method. They inferred that inclusion of Fe³⁺ in the Fe-doped mesoporous TiO₂ takes place. Therefore, Fe³⁺ ions were present in the bulk as well as at the surface. In contrast, V ions were present basically only at the surface and did not enter the bulk of the V-doped mesoporous TiO₂. Moreover, Cu-doped mesoporous TiO₂ was prepared by Guo's group [65] via a hydrothermal method at relatively low temperatures without any calcination. Triblock copolymer Pluronic P123 has been used as a template, Tetrabutyl titanate (TBT) has been used a titanium precursor, and Cu(NO₃)₂·3H₂O has been used as a copper source. XRD and XPS results showed that the copper species existed with oxidation state of Cu¹⁺, which was attributed to the reduction effect of dihydroxylation during synthesis process. For doped sample with 1 Wt. % Cu-doped mesoporous TiO₂, the Cu¹⁺ was dispersed in mesoporous TiO₂ lattice as Cu¹⁺. Whereas, for doped sample with 3 Wt. % Cu, the Cu¹⁺ was dispersed in the form of micro-TiO₂ crystal with Cu₂O small clusters. They concluded that the excess copper could not replace Ti⁴⁺.

Recently, mesoporous anatase-brookite TiO₂ doped with different Fe/Ti molar ratios have been synthesized by Soo et al [66]. The results showed that the addition of Fe dopant into TiO₂ especially brookite phase has induced a red shift in the observed optical absorption which reduced the band gap from 2.97 eV to 1.59 eV. The prepared Fe doped mesoporous TiO₂ samples have an anatase-brookite and mesoporous structure with a large surface area. XRD results indicated that Fe³⁺ ions have been successfully inserted via interstitial substitution into the crystal structure of TiO₂ and thus occupied some of the TiO₂ lattice sites.

1.2.2.2 Nitrogen doped mesoporous titanium dioxide powder

Incorporation of non-metal atoms such as nitrogen, hydrogen, boron, carbon, fluorine, iodine, sulfur, and phosphorus into the TiO_2 structure is still one of the most popular and effective method to promote its photocatalytic efficiency. These atoms have orbitals of suitable energy to mix with the TiO_2 oxygen orbitals. In particular, nitrogen attracts great attention since nitrogen atoms can be introduced into the TiO_2 lattice due to its comparable atomic size to oxygen atom, small ionization energy, and high stability [54]. The mixing process includes mixing of N 2p states with O 2p states. The calculated densities of states showed that the substitutional N doping is more efficient in reducing the bandgap of titania compared to doping with other non-metal elements [67]. Generally, this incorporation leads to decrease of the electron-hole recombination rate in addition to reduction in the band gap by forming a mid-gap state (Figure 2). Moreover, this leads to better photocatalytic activity [68]. In 1986, Sato appeared to be the first researcher to synthesis a nitrogen-doped TiO_2 by calcination of titanium hydroxide. He found that the enhanced spectral sensitization of titanium dioxide was due to the presence of NO_x impurities that were formed from the used NH_4OH in the preparation [69].

A large number of recent physical and chemical variety methods have been utilized to incorporate nitrogen into the TiO_2 lattices. These methods are mainly based on two kinds of processes. One process can be ascribed as one-step direct incorporation of N atoms into TiO_2 lattice such as calcination, sol-gel method, ball milling, plasma or ion implantation, solvothermal method, hydrothermal method, electrochemical method, microwave, direct hydrolysis of organic /inorganic salts, and pulsed laser deposition (PLD) [70]. The second important synthesis process can be described as two-step oxidation of titanium nitride. This process could be done via different strategies such as sputtering method, thermal annealing, and plasma-enhanced micro arc oxidation [71]. All strategies can be classified into two main processes. The first one includes dry processes such as oxidation of titanium nitride powder in an oxygen gas flow, nitrification of TiO_2 powder in an ammonia gas flow, and anatase TiO_2 powder treated by plasma in N_2 gas or $\text{N}_2\text{-H}_2$ mixed gases. The second one involves wet processes such as sol-gel method, hydrothermal method, and solvothermal method [72].

The synthesis method plays a very important role to form nitrogen species. Various types of nitrogen species introduced in TiO_2 lattice, which lead to N-doped TiO_2 with different physical and chemical properties. Despite this, the mode of nitrogen doping in the TiO_2 lattice is unclear. The nitrogen species can be assigned as substitutional (Ti-N-Ti) and/or

interstitial N (Ti-O-N or Ti-N-O) atoms, including oxidized NO_x , hydrogen containing NH_x species, as well as carbon nitride-like fragments [73, 74]. The substitutional doping means oxygen replacement while interstitial doping means the addition of nitrogen into the TiO_2 lattice [70, 75]. Interstitial doping reduces the band gap of TiO_2 more than the substitutional doping (Figure 2).

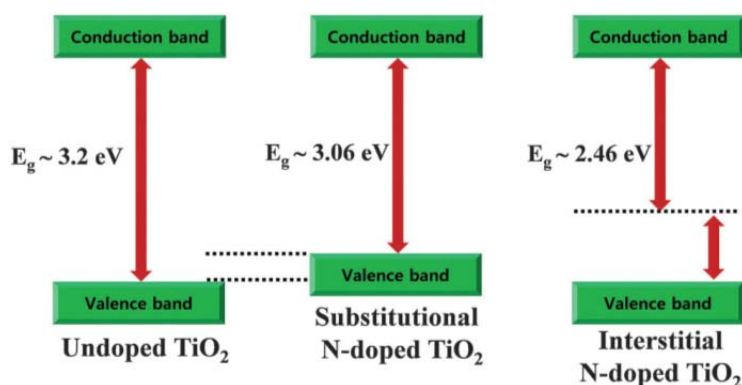


Figure 2. Schematic diagram showing the valence and conduction bands of un-doped and N-doped TiO_2 [70].

Over the past years, a number of studies have focused on influence of the experimental parameters of the sol-gel N-doping method on the photocatalytic activity of N-doped TiO_2 . Some studies have taken into account the TiO_2 precursors, nitrogen precursors, solvents, pH values, and post N-doping treatments [76]. Fang et al. have successfully synthesized mesoporous N-doped TiO_2 by the precipitation of titanyl oxalate complex ($[\text{TiO}(\text{C}_2\text{O}_4)_2]^{2-}$) by ammonium hydroxide ($\text{NH}_3 \cdot \text{H}_2\text{O}$) at low temperature followed by calcination at different temperatures. The doped N species located at the interstitial sites in TiO_2 led to reduction of the TiO_2 band gap. Moreover, they explored that N-doped TiO_2 calcinated at 400 °C has Brønsted acid sites arising from covalently bonded dicarboxyl groups [77].

N-doped Mesoporous TiO_2 powders were synthesized by Gibaud and co-workers via the sol-gel route either directly or by using the P123 templating agent and nitrogen doping from thiourea. Their EPR results showed that several paramagnetic species were found in these mesostructured samples mainly with oxygen radicals for calcinations at 400 °C. In contrast, nitrogen centers appeared for calcination temperature as high as 500 °C during 12 h [78].

Hui-Lei and his colleague synthesized N-doped mesoporous titania using PEG as template and dimethyl formamide (DMF) as nitrogen source. They explained that PEG played

an important role in the preparation process within mesoporous titania. The N-doped mesoporous titania possessed diameter of ca. 20 nm with anatase crystalline structure, and had absorption in the visible region [79].

Recently, Zalas has reported synthesis of the N-doped mesoporous titania by template-free solvothermal method that could be considered as a good and inexpensive method. The main advantage of template-free methods of mesoporous TiO_2 synthesis was environmental friendliness in connection with potentially cheaper way to obtain well defined mesostructure. He employed titanium tetra isopropoxide as titanium source, urea and nitric acid as nitrogen source. His results showed that the temperature treatment brought an increase in the crystallite sizes and a significant decrease in the specific surface area after calcination at 400 °C [80].

More recently, Huang and his colleagues synthesized N-doped anatase mesoporous TiO_2 through a sol-gel method, followed by cycle microwave-assisted hydrothermal method using three different types of nitrogen sources (diaminohexane, methylamine, and urea). They claimed that different sources lead to different degrees of doping. Moreover, at low doping concentration, the N atoms were found in the interstitial sites while at high doping concentration, the N atoms were incorporated into the TiO_2 lattice [81].

1.3 Ordered mesoporous materials

According to the arrangement of pores, mesoporous materials can be classified into two kinds including ordered and disordered materials based on IUPAC classification. Ordered mesoporous materials have uniform and regular arrangements of pore widths whereas, atomic arrangements are not ordered. They are obtained by templating pathways. However, disordered mesoporous materials have uniform channel width, but they are not regularly arranged i.e. neither the pore arrangements nor the atomic arrangements are ordered. Those are obtained by template-free methods [82]. The mesopores in mesoporous materials are isolated or interconnected that may have similar or different shapes and sizes [83]. Ordered mesoporous materials are important kind of functional materials. They have attracted intensive interest in various research areas such as catalysis, sensor, energy conversion and storage, environment remediation, and biomedical sciences [84]. In the fact for photocatalytic applications, the presence of ordered mesoporous in nanostructured materials promotes diffusion of the reactants and products throughout the channels. Moreover, it is offering more active sites for pollutant adsorption and consequently increasing the reaction speed [85, 86].

1.3.1 Ordered mesoporous titanium dioxide powder

Based on the nature of the templates and the spatial relationship between templates and products, there are two templating strategies to synthesize the ordered mesoporous TiO_2 . They include the soft-templating (endotemplate) and hard-templating (exotemplate) pathways. The soft-templating pathway implies the use of surfactants that forms micelles such as block copolymer. In contrast, the hard-templating pathway implies the use of porous solids such as silica or carbon [82, 86].

A process often applied for synthesis of well-ordered mesoporous titania is the evaporation-induced self-assembly (EISA) method [41]. This method is a simple and facile method to synthesize inorganic-organic highly uniform mesoporous materials in the form of powder and thin films using various surfactants [41]. It involves a cooperative assembly process between sol-gel species and supramolecular templates [87].

Previous studies have shown the effect of various synthesis parameters on the formation of ordered mesoporous titania using the EISA method. These parameters include nature and concentration of the surfactant, titanium precursor, the molar surfactant/titanium source ratio, the choice of solvent used, acid concentration, amount of water or hydrolysis ratio ($H = \text{H}_2\text{O}/M$, where M = metal such as Ti) and calcination temperature [41, 88-91]. The synthesis of ordered mesoporous TiO_2 is mainly affected by any change in the experimental setup [41].

The role of amount of water in the formation of ordering mesophase has been studied by Soler-Illia and his colleagues. They explained that low water content and strong chelation between metal centers and the non-ionic polar heads lead to polymer unfolding and thus to worm-like phases. However, larger quantities of water and acid added to the reaction bath weaken the coordination bonds that compose the hybrid interface. These resulting weak interactions (mainly hydrogen bonds) help in the folding of the templating agents, and yield more ordered mesophases [92].

Recently, several studies have focused on synthesis of the ordered mesoporous titania that was mostly synthesized by sol-gel chemistry using ionic or non-ionic surfactants as templates [3, 86]. The role of surfactant has been explained; the template acts as structure directing agent (SDA) in the synthesis of the porous materials. The presence of template is very important to control the shape and structure of the pores. In other words, the templates play key roles in modulating the mesostructure, surface area, pore size, wall thickness, and thermal stability of mesoporous TiO_2 . As well known, the surfactant molecular system consists of two regions including the hydrophilic (polar) and hydrophobic (non-polar) parts.

In aqueous media, the polar part of the surfactant molecule favorably interacts with water, while the non-polar part stays away from water molecules. The aggregates of surfactant molecules are called micelles. A self-assembly of these micelles through weak coordination bonds occur to form 3D or 2D nanostructure and helps in the pore generation [82]. Pluronic block copolymers are important kind of the surfactants, which are more suitable for the synthesis of the ordered mesoporous titanium oxides with large pore size, high surface area, and well-crystalline materials. The reason is that the tailor-made amphiphilic block copolymers (ABCs) exhibit high glass transition temperature, thermal stability, and high content of sp^2 hybrid carbon atoms [43]. Hexagonal ordered mesoporous TiO_2 material with an anatase phase and high surface area have been synthesized by Kao et al. This has been done by using a cationic surfactant cetyltrimethyl ammonium bromide ($\text{C}_{16}\text{TMABr}$) as a structure-directing agent and soluble peroxytitanates as Ti precursor through a self-assembly between the positive charged surfactant S^+ and the negatively charged inorganic framework I^- (S^+I^- type) [93]. Recently, Cao et al. synthesized hexagonal ordered mesoporous titania with thermal stability up to 700°C by combining the EISA method and template-carbonization strategy through. They used PEO-*b*-PMA(Az) as a structure-directing agent, titanium isopropoxide and titanium chloride (TiCl_4) as a titanium source, and tetrahydrofuran (THF) as the solvent. They confirmed that the template carbonation in nitrogen after ageing is the key step to obtain the ordered crystalline mesostructure [94]. In 2015, for the first time Veliscek-Carolan et al. reported synthesis of the ordered mesoporous titania powders using the block copolymer F127 as a template without the use of stabilizing agents via evaporation induced self-assembly (EISA). They demonstrated that the choice of template affects the growth and structure of Ti oligomers in the precursor solution due to the size of the EO blocks in the block copolymer templates. Moreover, the optimal evaporation temperature during EISA was dependent on the choice of template [95].

Moreover, Hung et al. have reported that titanium alkoxides have been utilized as titanium precursor for the synthesis of mesoporous TiO_2 because of their higher chemical stability and they are safe to handle [96]. As well as it gives a very good compositional and morphological control over the product properties, such as specific surface area and degree of aggregation [42].

The solvent was also an important parameter in changing the morphology and performance of the sol-gel-derived porous TiO_2 [96]. Ethanol has been chosen as a good solvent due to its surface wetting properties and the good solubility of all organic and

inorganic precursors [97]. HCl was preferred due to its volatility, which is required during the evaporation-assisted deposition [87].

Figure 3 summarizes the sol-gel technique used in the synthesis of ordered mesoporous TiO₂ via different strategies.

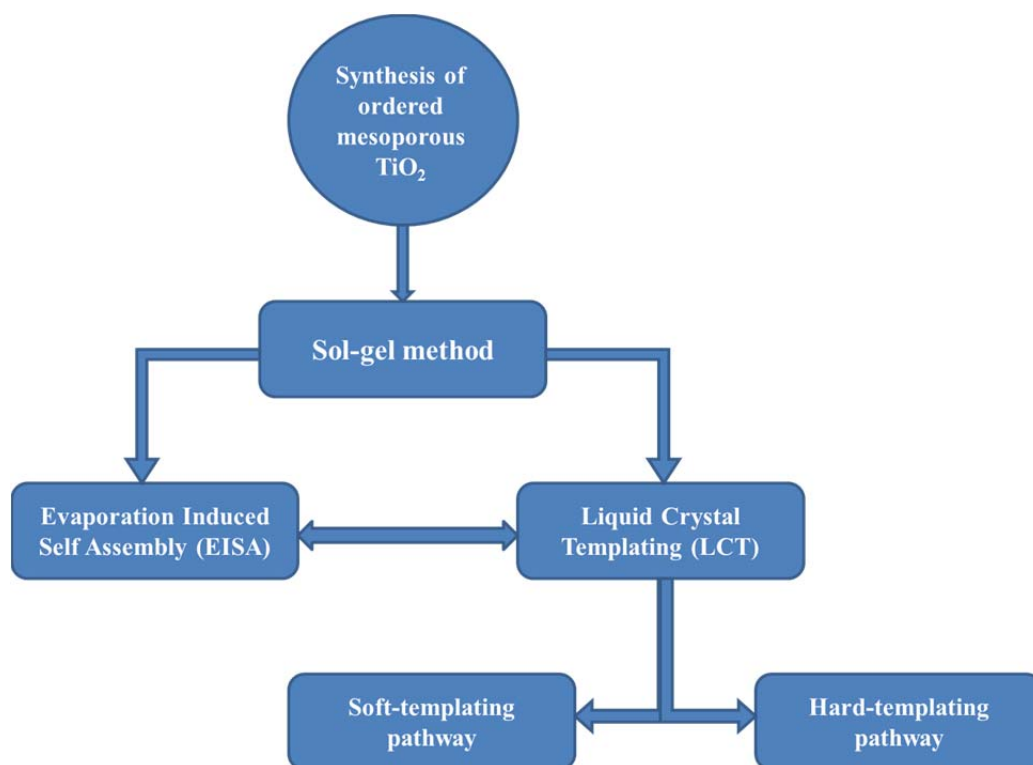
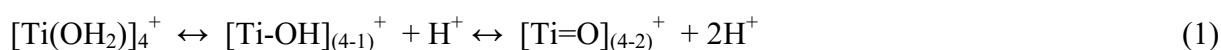


Figure 3. Schematic diagram showing common the sol-gel technique used in synthesis ordered mesoporous TiO₂.

Generally, the control of the titanium precursor hydrolysis and condensation was considered as one important key parameter for the formation of ordered mesoporous TiO₂ [89]. The hydrolysis reaction depends on the acidity of the medium, which can be defined as follows (Eq. (1)) [98]:



Inorganic titania species in water were found in a balance between Ti-aquo, Ti-hydroxo, and Ti-oxo complexes. The dominating complex is determined mainly by acidity, where the balance is shifted from oxo complexes at low acidity to hydroxo complexes at intermediate and aquo complexes at high acidity. The interchange between water and hydrochloric acid increases the condensation rate necessary for the formation of a stable inorganic framework. Previous study showed that Ti-OH₂⁺ groups are formed instead of Ti-OH at high hydrochloric

acid concentration. Because of charge repulsion between the groups, dehydration hardly occurs, and the Ti-O_6 octahedral prefers to share corners with each other [99]. Aquo-ligands are excellent leaving groups but poor nucleophiles, thus the condensation of titania will be severely hampered due to the lack of good nucleophiles, allowing the system longer time to self-assemble into an ordered mesophase [100]. For the reaction under acidic conditions, more hydrophilic groups (EO) head towards water. This leads to inhibition of the hydrolysis rate and balance of the condensation. The regulation of the hydrolysis and condensation is very useful in the synthesis of the ordered mesoporous TiO_2 .

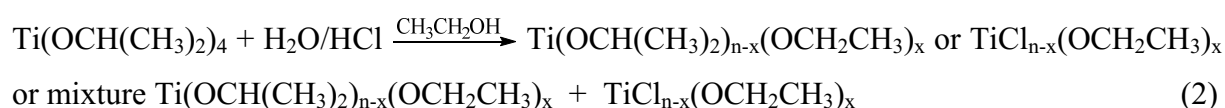
Chen et al. reported a method for the synthesis of well-ordered mesoporous bulk titania by the nonhydrolytic EISA method using TiCl_4 and $\text{Ti}(\text{O}i\text{Bu})_4$ as a titanium precursor and the polymer P123 as surfactant [101]. Their results explained that the molar ratio of $\text{TiCl}_4/\text{Ti}(\text{O}i\text{Bu})_4$ was paramount importance in tuning the sample's pore structure and the phase composition of anatase and rutile.

Although synthesis of ordered mesoporous TiO_2 films has been achievable, synthesis of ordered mesoporous TiO_2 powders in large quantities via evaporation induced self-assembly through EISA method remains challenging [95]. Rare cases of prepared ordered mesoporous TiO_2 powder were found stable. This is due to the main challenge to preserve the ordered mesostructure and high surface area after the surfactant removal during the framework crystallization processes at high temperature. This is mostly accompanied by porosity deterioration or structure collapse, because of the intrinsic crystallization of anatase phase [34]. Therefore, most of the reported work on mesoporous titania are focused on films [102], [103] because it is not easy to obtain ordered mesoporous TiO_2 powder. Figure 4 shows a simple schematic of sol-gel technique employed to synthesize ordered mesoporous structure TiO_2 .

Liu et al. synthesized ordered mesoporous titania by the EISA technique using liquid crystal as template LCT [104]. Moreover, they synthesized TiO_2 nanoparticles by sol-gel method without LCT. The polymer CTAB has been used as a template and tetrabutyl orthotitanate as a titanium source.

Zimny et al. presented a synthesis process where the EISA method was combined with the liquid crystal templating pathway (LCT) [89]. Advantages of this method in comparison to other methods [105, 106] are their relatively short preparation period (3 days), a simple and an effective route for synthesizing mesoporous titania with a high mesoporous ordering and thermal stability. The synthesis process consists of various chemical steps are summarized in

Figure 4. The first step includes dissolving a surfactant and a titanium precursor in ethanol in the presence of acid. This step is very important because it is the key to obtain ordered mesoporous structure. The copolymer P123 consists of two parts hydrophilic (polar) and hydrophobic (non-polar). After that, HCl will be added. In this step, the micelles are formed [107]. The high concentration of HCl allows to the control of hydrolysis-condensation reactions and avoids the precipitation of a titanium oxide phase, and the micelle will agglomerate. Upon dissolution in the presence of alcohol and HCl, the Ti precursor undergoes fast exchange reactions with alcohol and/or chloride ions, which make hydrolysis processes to proceed practically instantaneously [92]. These reactions can be schematically represented as follows (Eq. (2))*:



* The equation above is not stoichiometry.

Subsequently, starting of a polycondensation reaction between the formed Ti-species leads to the formation of discrete Ti-oxo-oligomers of general formula $[\text{TiX}_x(\text{OH})_y\text{O}_{2-(x+y)/2}]$ X: OR or Cl, clusters or small polymers [92]. The co-condensation of these subunits around the micelles is hindered by the presence of acid [49, 92]. The degree of condensation depends on the $[\text{H}_2\text{O}]:[\text{Ti}]$ and $[\text{H}^+]:[\text{Ti}]$ ratio [87]. The second step is the evaporation of solvent; the mixture has been placed under vacuum to evaporate the alcohols in order to form the hexagonal hybrid mesophase structure gel by agglomeration of micelles (more of polycondensation reactions). The third step is the treatment of the obtained gel with ammonia vapor to precipitate amorphous TiO_2 by induce more of polycondensation reaction. The fourth step is removal of surfactant by ethanol. Finally, the fifth step is the calcination of amorphous TiO_2 at high temperature to obtain crystalline TiO_2 .

It was shown that mesoporous ordering and pore size of the formed amorphous titania framework obtained after surfactant extraction can be controlled by the molar surfactant/titanium precursor ratio and the surfactant concentration [90].

Different methods were reported to transform the amorphous titania framework into crystalline titania domains while the mesostructure is preserved intact, such as conventional calcination conditions (under Ar or N_2 then O_2) and flash induction calcination (induction furnace) [90, 108-110].

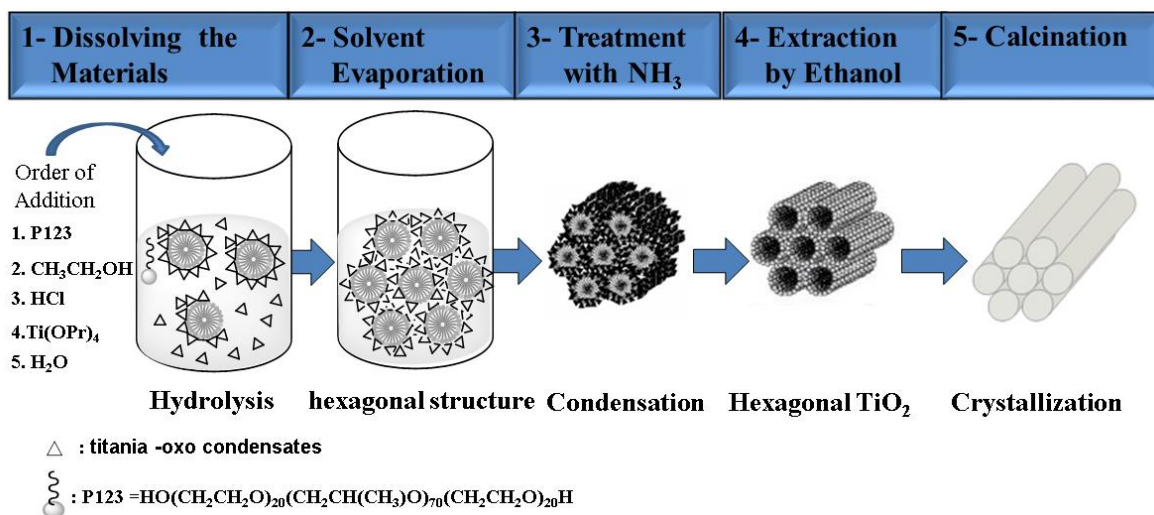


Figure 4. Schematic diagram showing procedures synthesis of ordering mesoporous titania (the draws in step 3 and 4 were taken from [89]).

1.3.2 Doping ordered mesoporous titanium dioxide powder

The term doping has been defined and introduced in the previous sections. Very little work about doping ordered mesoporous titanium dioxide powder in comparison with mesoporous titanium dioxide. This work will be summarized in the following.

1.3.2.1 Metal-doped ordered mesoporous titanium dioxide powder

Metal doped mesoporous TiO₂ powder is an important area of research, however relatively very little is known about metal doped ordered mesoporous TiO₂. In 1999, cobalt doping into the mesoporous structure was reported for the first time in this system, and its structure was determined by Yin and Wang via template-assisted self-assembly techniques. They employed polystyrene (PS) particles as template, titanium butoxide as titanium precursor and heptane solution of cobalt carbonyl as cobalt source. They found that cobalt titanium oxide may be formed on the internal surface of the ordered pore structure. They suggested that transition metal elements could be incorporated into porous titania without blocking the interconnected pores [111].

In 2006, Wang et al. prepared Fe-doped ordered mesoporous titania through a hydrothermal process by using CTAB as a template and tetrabutyl orthotitanate (TBOT) as precursor. They concluded that ordering of the pore channels and the thermal stability of the mesostructure at 350°C were improved after the incorporation of iron into TiO₂ [112]. In another study [113], Fe-doped ordered mesoporous TiO₂ has been synthesized via the EISA using P123 as soft template, TBOT as a titanium precursor and ferric nitrate (Fe(NO₃)₃·9H₂O) as an iron source. The results indicated that the 0.5 mol ratio of doped Fe³⁺ ions had an

ordered mesoporous structure. They explained that the Fe^{3+} ions introduced into the lattice of mesoporous TiO_2 could reduce the growth of the anatase during the calcination and preserved the mesoporous structure with large surface area. Further, cobalt-doped ordered mesoporous titanium dioxide also has been successfully synthesized by Ye and co-workers via a multicomponent self-assembly process. They used triblock copolymer Pluronic F127 as a template, tetrabutyl titanate as a titanium source and cobalt acetate as a cobalt source. The doped Co species have changed the construction of the conduction band and valence band of TiO_2 leading to visible-light absorption by TiO_2 [114].

Moreover, the highly ordered 2D hexagonal mesoporous Bi-doped TiO_2 with changing Bi ratios (from 0 to 4 mol%) has been synthesized by Sajjad et al. [115] through an ethanolic EISA process. They employed triblock copolymer Pluronic P127 as a template, titanium isopropoxide as a titanium precursor and bismuth nitrate as a bismuth source. They used variable Bi ratios (1, 2, or 4% Bi-doped ordered mesoporous TiO_2). Here, no effect of using different Bi ratios on the ordered hexagonal mesostructure has been investigated. Moreover they studied the thermal stability at three different temperatures (350, 400, and 450 °C). They concluded that increasing the calcination temperature leads to a gradual decrease of diffractive strength due to the degree of ordering of the mesoporous structure.

Recently, Assaker et al. [116] have examined the effect of the zinc ion addition on the structure and photocatalytic properties of the ordered mesoporous titania. They observed that the hexagonal array was lost upon increasing the zinc content to higher than 7 mol%. The decrease in the activity of methyl orange photo-degradation under UV irradiation at high Zn content was related to the decrease of the crystallinity as well as to the shift of the band gap. In the same context, Co-doped ordered mesoporous TiO_2 has been fabricated by Li et al. [117] via multicomponent self-assembly procedure. They used triblock copolymer Pluronic F127 as templates, tetrabutyl titanate ($\text{C}_{16}\text{H}_{36}\text{O}_4\text{Ti}$) and cobalt acetate ($\text{C}_4\text{H}_6\text{CoO}_4 \cdot 4\text{H}_2\text{O}$) as cobalt source. They showed that low cobalt contents up to 3 mol% did not destroy the mesoporous structure and hence the response of the sensors increased with increasing the cobalt contents. Above this content (e.g. 5 mol%), the cobalt started to appear in oxides form and the mesoporous structure was mainly destroyed.

1.3.2.2 *Non-metal doped ordered mesoporous titanium dioxide powder*

N-doped ordered mesoporous structure TiO_2 powder has been synthesized by Ikuma and his group [118]. Their results showed stronger absorption in the visible region above 400 nm, owing to the substitution of the lattice oxygen by nitrogen. Their XPS results proved the doping of nitrogen in to oxygen in TiO_2 lattice. More recently, Li et al. [119] have reported nitrogen doped ordered mesoporous TiO_2 powder via EISA method combined with the post-annealing treatment in NH_3 atmosphere. The BET surface area of ordered mesoporous TiO_2 and N-doped ordered mesoporous TiO_2 were 139.6 and 138.7 m^2/g . in addition, their XPS results suggested existence of N-Ti-O and Ti-O-N bonding.

1.4 Principles of photocatalysis

The development of water treatment technologies has included conventional technologies such as activated carbon adsorption and solvent extraction, and advanced technologies such as electro-Fenton method, membrane-based separation method, and photocatalysis. All these methods have been successfully used for removal of phenolic compounds from water [120]. However, well-known conventional methods for wastewater treatment are not efficient enough to destroy the refractory organic pollutants. Moreover, their applications are limited because of the high cost and the required sophisticated equipment (Panda et al., 2011). Based on IUPAC, the term photocatalysis means that the reactions are carried out in the presence of a semiconductor and light [121]. The photocatalysis technology has received enormous attention in recent years. It is rapidly developing as one of the most active areas of chemical research. It can be applied in different scientific areas such as electrochemistry, medicine, and environmental chemistry. Photocatalysis can be classified into two main branches including homogeneous and heterogeneous photocatalysis. This classification is mainly based on the phase of the reactant as well as the photocatalyst. Moreover, the main difference between a conventional thermal catalyst and a photocatalyst is that the former one is activated by heat whereas the latter is activated by photons of appropriate energy [53]. Currently, heterogeneous photocatalytic techniques are using a semiconductor (such as TiO_2) as photocatalyst to degrade various pollutants (such as phenol and its derivation) from water [122]. Furthermore, the photocatalytic activity of ordered mesoporous TiO_2 was obviously enhanced compared to that of disordered mesoporous structures. The increase in activity was attributed to their uniformly distributed porosity leading to high specific surface areas, which could enhance both the diffusion of reactants and products and the access to active sites [2, 86].

However, it has to be mentioned that the ability of titania to undergo a charge transfer from the semiconductor to the surface adsorbed species depends on the position of the CB and VB edges and the redox potential of the adsorbed molecule (Figure 5). The energetic level of an electron accepting species that will be reduced has to be lower than the lower edge of the titania CB. In contrast the energetic level of a hole accepting species that will be oxidized has to be higher than the upper edge of the titania VB.

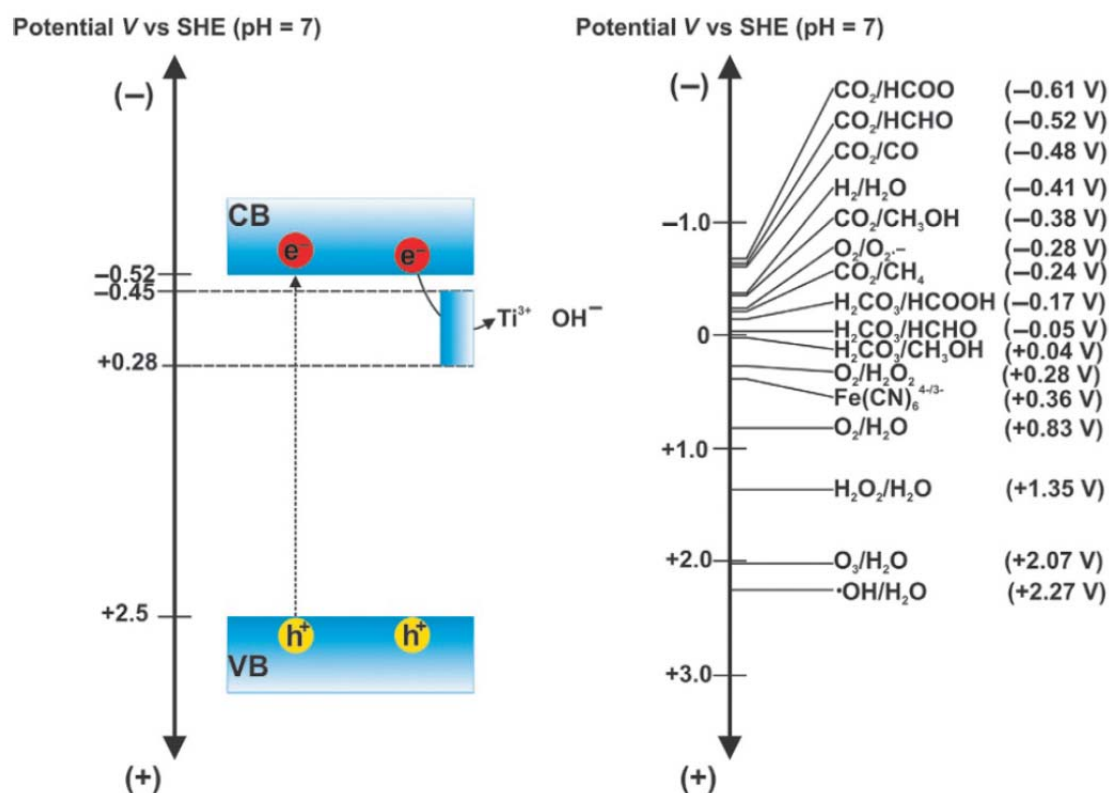


Figure 5. Comparison of energetic level of titania VB and CB band with the redox potential of different processes [123].

1.5 Photoactivity of mesoporous titanium dioxide powder

1.5.1 Photoactivity of undoped-mesoporous titanium dioxide powder

In recent years, great efforts have been devoted to study the photodegradation of organic and inorganic pollutants of water and air by employed mesoporous TiO_2 [58]. Generally, previous studies showed that the photoactivity of TiO_2 depends on its structural and morphological characteristic. These are related to the method of synthesis used in the preparation of nanoparticles. To be photoactive, the photocatalysis process favoring, being mainly consisting of anatase crystalline phase, high surface area, good porosity, with high sized pores [124]. In the fact, the relation between the physical properties and the photocatalytic activities is complicated. A large surface area with a constant surface density of

adsorbents led to faster surface photocatalytic reaction rates. However, the surface is a defective site; therefore the larger surface area is the faster recombination. The higher the crystallinity means the fewer the bulk defects, which leads to high photoactivity [1]. Other reports showed that the photocatalytic activity of TiO_2 is influenced by the crystal phase, pore diameter, and surface hydroxyl group density. All these structural factors are dramatically dependent on the TiO_2 synthesis procedure [125, 126].

Moreover, many studies suggest that the photocatalytic activity depends on the number of electrons and holes at the photocatalyst surface. In addition to many other factors, the small grain size leads to a shorter distance for the electrons and holes to transfer to the photocatalytic reaction sites. So efforts should be made to increase the specific surface area and decrease the grain size that would improve photocatalytic activity [40].

Further, mesoporous TiO_2 has been employed as photocatalyst for chloro-phenol degradation. Its degradation efficiency increased with increasing the PEG molecular weights. The remarkably high catalytic activity of the mesoporous TiO_2 was derived from its high crystallinity and mesostructure as compared to Degussa P-25 [115]. Moreover, it was observed by Zhang's group [40] that the absorption intensity, in the visible region, for the prepared samples by the two-step calcining process (powder was calcined at 500-700 °C in nitrogen, and then recalcined at 500 °C in air) is higher than that for the prepared samples by the one-step calcining process (calcined at 500 °C in air).

1.5.2 Photoactivity of doped-titanium dioxide powder

Generally, the photocatalytic activity of pure mesoporous materials could be enhanced by dispersing metals on surfaces of these materials [83]. This will increase the reaction efficiency by introducing more active sites. Both metal- and non-metal-doped mesoporous TiO_2 could extend the absorption edge into the visible-light region and improve the separation efficiency of the photogenerated electron [36]. Photoactivity of doped- TiO_2 substantially depends on several factors such as the nature and concentration of dopants, thermal treatment, and thus on the synthesis method [127].

1.5.2.1 Photoactivity of metal-doped mesoporous titanium dioxide powder

The photocatalytic performance of titania can be further improved by doping of the material with transition metal ions [17, 34, 36, 57, 128]. The activity of the doped material is influenced by the preparation method, specific metal and its concentration, the location and distribution of the metal ions in the titania phase, and the oxidation state of the metal and its local environment.

Zhu et al. [61] studied effect of the synthesis method and iron doping on the photocatalytic activity of TiO_2 . They investigated activity of their samples by photolytic degradation of methylene blue under visible light irradiation. They showed that Fe- TiO_2 obtained via NSG route exhibited a higher photoactivity compared to the undoped TiO_2 and the Fe- TiO_2 obtained via HSG route. The NSG route was superior to the HSG route due to its controlled reaction rate and lack of the surface tension. This could be explained by the formation of mesoporous, well-crystallized anatase, the strong absorbance for visible light, and more surface oxygen vacancies and/or defects that could reduce the recombination process between the photoelectrons and holes. This will lead to the enhanced quantum efficiency of photocatalysis. Moreover, the enhancing of the Fe-doping on the photocatalytic activity could be attributed to the producing of intermediate energy levels that allow Fe- TiO_2 to be activated easily in the visible light.

In the same context, the photocatalytic property of the prepared samples by Shouqiang et al. [62] was evaluated by degradation of the methylene blue (MB) solution. The appropriate content of iron can effectively enhance the absorption in the visible light region and the photocatalytic activity of TiO_2 . The optimum content of the doped Fe was 2 mol%.

Here, the effect of titanium source on the photocatalytic properties of TiO_2 doped with iron will be briefly introduced. Goswami and his colleague [63] demonstrated that the Fe-doped mesoporous TiO_2 prepared from (K_2TiF_6) was much more effective in the photocatalytic decomposition of bromocresol green than undoped mesoporous TiO_2 as well as commercial titania.

The effects of copper doping and mesoporous structure on the photocatalytic properties of TiO_2 have been reported by Guo's group [65]. The results confirmed that copper doping greatly promoted the absorption in the visible light region and played a significant role for enhancing the photocatalytic activity of the catalysts. The observed high photoactivity of the catalysts for degradation of methyl orange (MO) strongly depends on the stabilization of Cu (I) that was well dispersed in TiO_2 . Moreover, mesoporous structures with larger specific surface area, pore size, and the relatively regular channel structure had better adsorption capacity. Yusop and his colleagues [66] have reported a significantly high photocatalytic activity for the Fe-doped mesoporous TiO_2 in the photodegradation of RB5 under solar light irradiation. This is due to the high surface area for the anatase-brookite phase and mesoporous structure.

1.5.2.2 *Photoactivity of non-metal-doped mesoporous titanium dioxide powder*

Previous studies have explained the synergistic effects of many factors on photocatalytic activity of N-doped TiO₂ such as synthetic methods, morphology, crystal phase, particle size, optical response, surface area, and nitrogen doping [70, 129]. Moreover, localized nitrogen state in N-doped TiO₂ lattice has a significant influence on the photocatalytic degradation of pollutants [72]. Wang et al. [130] synthesized N-doped mesoporous TiO₂ polycrystalline powders by calcination of the hydrolysis product of tetra butyl titania with ammonia. Their results showed that the photocatalytic activity of N-doped TiO₂ was higher than that of P25 for the phenol degradation under visible light irradiation, while P25 showed higher photocatalytic activity under sunlight irradiation.

Over the past years, a number of studies have focused on study influence of the experimental parameters of sol-gel N-doping method on the photocatalytic activity of N-doped TiO₂. These parameters included TiO₂ precursors, nitrogen precursors, solvents, pH values, and post N-doping treatments [76]. Huang and co-workers [77] investigated that N-doped TiO₂ calcined at 400 °C has Brønsted acid sites arising from covalently bonded dicarboxyl groups. This greatly promoted the adsorption capacity for methyl orange. N-doped mesoporous titania samples demonstrated excellent photoactivity for methyl orange (MO) degradation under visible light irradiation, which could be attributed to synergistic effect between the retained alkoxy groups and the nitrogen doping [79]. Moreover, Zalas observed that N-doped mesoporous TiO₂ materials are more active than the undoped mesoporous TiO₂ and P25 [80]. He concluded that the improvement in the photocatalytic efficiency of N-doped TiO₂ is due to their visible light sensitization caused by incorporation of nitrogen atoms into the TiO₂ structure. His results also indicated that the relatively low specific surface areas of N-doped mesoporous TiO₂ materials have not influenced their activity.

Zhang et al. studied the influence of different chemical bonds for the nitrogen element in each particular nitrogen source on the photocatalytic properties of N-doped TiO₂. They tested the photoactivity of materials in carbon dioxide photocatalytic reduction under visible light illumination. CH₄ was the main product with N₂H₄-doped N-TiO₂, while CO was the main product with NH₃-doped N-TiO₂ [131]. Rayalu and his group [132] explored the photo-oxidation properties of N-doped mesoporous titania in photodegradation of phenols under visible light. Their study showed the effect of various operating parameters including catalyst loading, pH, initial concentration, and the effect of coexisting ions (such as chloride, carbonate and bicarbonate) on the rate of photocatalytic degradation of both phenol and o-

chlorophenol. It was found that the catalyst showed significant activity in the solar radiation as compared to artificial light. Their results indicated that initial pH and coexisting ions have a significant influence on the photocatalytic degradation rates. Maximum photodegradation was observed at neutral pH while the presence of co-ions has a detrimental effect on the degradation rates in case of both phenol and o-chlorophenol. Further improvement in the photoactivity of N-doped mesoporous titania was envisaged by co-doping with nonmetal or metal ions.

1.6 Photoactivity of ordered mesoporous titanium dioxide powder

1.6.1 Photoactivity of pristine mesoporous titanium dioxide powder

In reference [101], the photocatalytic activity of powders prepared for phenol degradation under UV irradiation showed that the well-ordered open pore structure and biphasic composition (anatase and rutile) played significant roles in determining the sample's photoactivity. In another reference [93], ordered mesoporous anatase TiO₂ demonstrated a remarkable photocatalytic efficiency for degradation of methylene blue (MB) under UV irradiation. The researchers attributed the reason to the associated effects of high specific surface area, pure anatase crystalline framework, and structural ordering of the mesopores.

Zhou et al. showed that the mesoporous anatase TiO₂ exhibited better photocatalytic activity than that of Degussa P25 TiO₂ under UV irradiation due to the integrated ordered large-pore mesoporous structure and the high crystallinity in favor of the separation of photogenerated electron-hole pairs [133]. The photocatalytic degradation of methyl orange also has been performed by Zimny's sample [90]. Here the influence of calcination temperature on photocatalytic activity was studied. They showed that the crystallinity played a significant role in the photoactivity. The material calcined at temperatures between 400 and 450 °C showed the fastest degradation rate under UV irradiation.

Ordered mesoporous titania has been synthesized by Zeng's group [104], it has shown higher photocatalytic efficiency for methylene blue (MB) degradation under UV irradiation than TiO₂ nanoparticles, due to the 2D hexagonal mesostructure with small particle size and high surface area. Cao et al. have investigated that ordered mesoporous titania demonstrated good photocatalytic activity for degradation of rhodamine B in aqueous suspension due to its highly crystalline material and large surface area [94].

Silvam's group [134] referred that the ordered mesoporous titania showed much higher activity than P25 due to synergistic effect of stable mesoporous structure and mixed

crystalline phases of titania (anatase, brookite and rutile). The presence of ternary phase compositions promoted the photoinduced e^-/h^+ pair life time by facilitating carrier migration across the phase junctions. Higher life time of the charge carriers led to higher OH radical concentration and a faster degradation rate of 4-chlorophenol.

Moreover, in other study, the effect of some physicochemical parameters such as time of adsorption prior to UV irradiation, initial methyl orange concentration, photonic flux, pH and amount of photocatalyst has been studied by Blin and his colleagues in order to optimize the experimental parameters. They tested ordered mesoporous TiO_2 efficiency on the photodegradation of methyl orange (MO) under UV irradiation. Their results explained that the efficiency of the process depended on the experimental conditions, which were including the time of adsorption prior to UV irradiation, initial methyl orange concentration, incident light intensity, pH and amount of photocatalyst [110].

1.6.2 Photoactivity of doped ordered mesoporous titanium dioxide powder

1.6.2.1 Photoactivity of metal-doped ordered mesoporous titanium dioxide powder

In the reference [113], the results indicated that the 0.5 mol ratio of Fe-doped had an ordered mesoporous structure and the highest photoactivity to degrade the methyl orange under visible light irradiation compared with other catalysts. The Bi-doped mesoporous TiO_2 samples by Sajjad et al. [115] enhanced photocatalytic activities for simultaneous phenol oxidation and chromium reduction in aqueous suspension under visible and UV light over the pure mesoporous TiO_2 , Bi-doped titania, and P25. The reason was attributed to both the unique structural characteristics and the Bi doping.

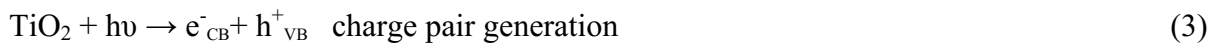
The ordered mesoporous Co-doped TiO_2 synthesized by Wang et al. [114] exhibited a much higher photocatalytic activity for CO_2 reduction under visible light owing to its regular porous structure and suitable band structure. In addition, the selectivity of the reduction products was improved by optimizing the energy-band configurations of cobalt-doped titanium dioxide through varying the molar ratio of Co/Ti. The optimal molar ratio of Co/Ti was 0.025, which showed the best photoactivity. When the doping content of cobalt species increases to some extent, Co_3O_4 /Co-doped TiO_2 nanocomposites with oxygen vacancies were obtained, which markedly improve the generation rate of CH_4 . In the same context, Assaker et al. explained [116] that the photocatalytic efficiency was significantly affected by the zinc content. The high content of zinc inhibited the photodegradation rate of methyl orange under UV irradiation.

1.6.2.2 Photoactivity of non-metal-doped ordered mesoporous titanium dioxide powder

The efficiency of photocatalyst prepared by Ikuma's group [118] was evaluated via the degradation of Rhodamine-B and antibacterial activity against *E. coli* under visible-light irradiation. N-doped mesoporous TiO₂ showed superior photocatalytic and anti-bacterial activity compared to pure TiO₂ under visible-light irradiation. The enhanced photocatalytic activity after N-doping was attributed to synergistic effect of nitrogen and well-ordered crystalline mesoporous structure with high surface area. Huang and his colleague [81] claimed that different sources of nitrogen doping led to different degrees of doping, which enhanced the photodegradation of methylene blue in the visible light region.

1.7 Photocatalytic mechanism

The photocatalytic mechanism of pristine TiO₂ under UV light irradiation (as shown in Figure 6) can be described during two steps. The first step of photoreaction is producing an electron-hole pair on the surface of TiO₂ nanoparticle. This step needs energy to overcome the band gap between the valence band (VB) and conduction band (CB). When the photon energy is equal to or exceeded the band gap energy (E_g) of TiO₂ (3.2 eV for the anatase phase), the electron-hole pairs are created in the volume and on the surface of TiO₂ nanoparticle (Eq. (3)). In this step, photoelectron is promoted to CB while a positive photo hole is formed in VB. The photocatalytic redox reaction will utilize the positive hole (h^+_{VB}) for the oxidation processes and the electrons (e^-_{CB}) for the reduction processes on the surface of the photocatalysts.



The second step involves producing the hydroxyl radical OH^\bullet with high redox oxidizing potential by the oxidation reaction of adsorbed water or OH^- (Eq. (4) and (5)). In addition, in conduction band, the electron is reducing the oxygen molecules to form superoxide anion $\text{O}_2^{\bullet-}$ (Eq. (5)). The superoxide anion is protonated (Eq. (7)) by H^+ , which is produced by (Eq. (5)). Then HOO^\bullet traps another excited electron to produce HO_2^- (Eq. (8)), which is protonated by H^+ to form hydrogen peroxide H_2O_2 (Eq. (9)). Finally, the hydrogen peroxide is reacting with the electron e^- to produce OH^\bullet (Eq. (10)). Here, the oxygen can play a very important role to produce more of OH^\bullet [17].

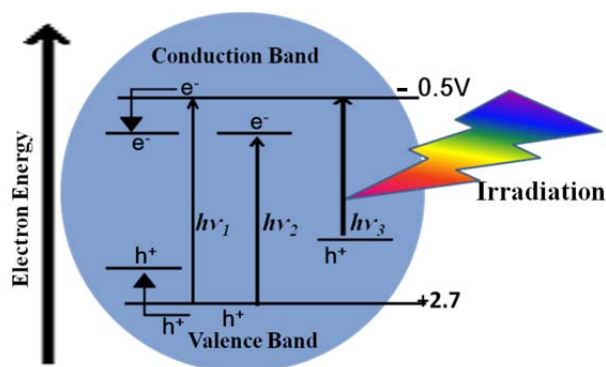
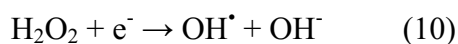
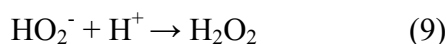
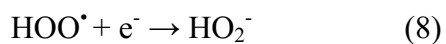
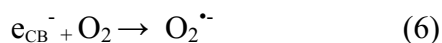
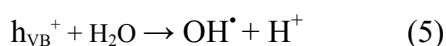
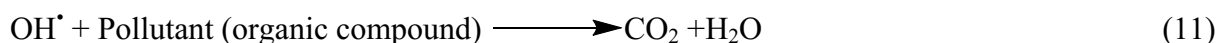


Figure 6. mechanism of $h\nu_1$: pristine, $h\nu_2$: metal-doped and $h\nu_3$: nonmetal-doped TiO_2 photocatalysis [58].

Now, the highly reactive hydroxyl radicals OH^{\bullet} will react to degrade and convert the pollutants into harmless products such as water and carbon dioxide at the end. (Eq. (11)).



The photocatalytic mechanism of metal-doped TiO_2 under visible light irradiation can be explained by a new energy level produced in the band gap of TiO_2 through the dispersion of metal ions in the TiO_2 matrix. Figure 6 shows the excitement of electrons from the defect state to the TiO_2 conduction band CB photon with energy equals $h\nu_2$. The introduced transition metal acts as trapping center for electrons to inhibit electron-hole recombination during irradiation, which is an additional benefit of transition metal doping. Figure 6 shows also the photo-catalytic mechanism of nonmetal-doped TiO_2 under visible light irradiation. There are three various major opinions: band gap narrowing, impurity energy levels, and oxygen vacancies [58].

1.8 Phenol as pollutant

Phenol compound is an aromatic compound with one hydroxyl group directly bonded to the aromatic ring with the chemical formula of C_6H_5OH . It is considered as one of the most extremely toxic industrial organic pollutants. It is produced as an intermediate in many industries such as petroleum refineries, chemical synthesis, plastics, adhesives and antiseptics [135]. Moreover, Phenol compounds have significant toxic effects on humans and wildlife upon exposure. So, many attempts have been done to find an effective way to remove it from wastewater.

Many various operating parameters have influenced the photocatalytic degradation rate of phenols such as crystal composition, type and amount of catalyst, light intensity, pollutant type and concentration, catalyst loading, solution pH, and oxidizing agent/electron acceptors

[128]. Previous studies showed that phenol could be degraded by OH radicals or directly via photogenerated carriers using photocatalysis technology [13, 136]. There are many different mechanisms proposed for the phenol degradation process by photocatalysis technology through OH radicals attack. In all these proposals, mostly hydroquinone and catechol have been formed in the first step of the reaction while the main products were water and carbon dioxide at the final step of the reaction. The differences were only in the intermediates compounds such as 2-hydroxy-propaldehyde, glycerol, 3-hydroxypropyl acid, hydroxyl-acetic acid, maleic acid, and oxalic acid. These differences were due to various reaction conditions and different analytical techniques (e.g. GC-MS and HPLC) applied to enrichment step and final detection of samples [136]. The general formula of the photocatalytic reaction on illuminated TiO_2 is shown below (Eq. (12)):

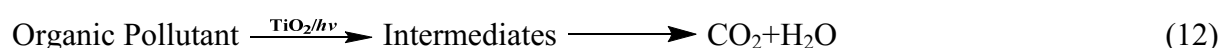


Figure 7 shows the possible proposed reaction mechanisms by Devi and Rajashekhar for the phenol degradation. The generated hydroxyl radicals attack the phenol molecule that leads to the formation of dihydroxy benzene (2) which is confirmed by the presence of m/z peaks at 110 (relative abundance [RA]: 42, retention time [Rt]: 10.4 min). Further degradation proceeds through the cleavage of dihydroxy benzene (2). After 15 min of UV irradiation, m/z peaks at 130 (RA: 54; Rt: 16.6 min) and 30 (RA: 42; Rt: 28.6 min) corresponding to the formation of Pent 2-enedioic acid (3) and formaldehyde (4) are observed. Few low intense peaks at 108 and 116 (RA: 49; Rt: 6.8 min) were accounted as benzoquinone (5) and maleic acid (6). The decarboxylation of maleic acid (6) and ring opening of hydroquinone (5) results in the formation of oxalic acid (7) with the m/z peak at 90 (RA: 64; Rt: 18.2 min). During the photodegradation process, formation of the two main intermediates of dihydroxy benzene (2) and benzoquinone (5) has been observed. Finally, decarboxylation of oxalic acid leads to the formation of carbon dioxide and water molecule [137].

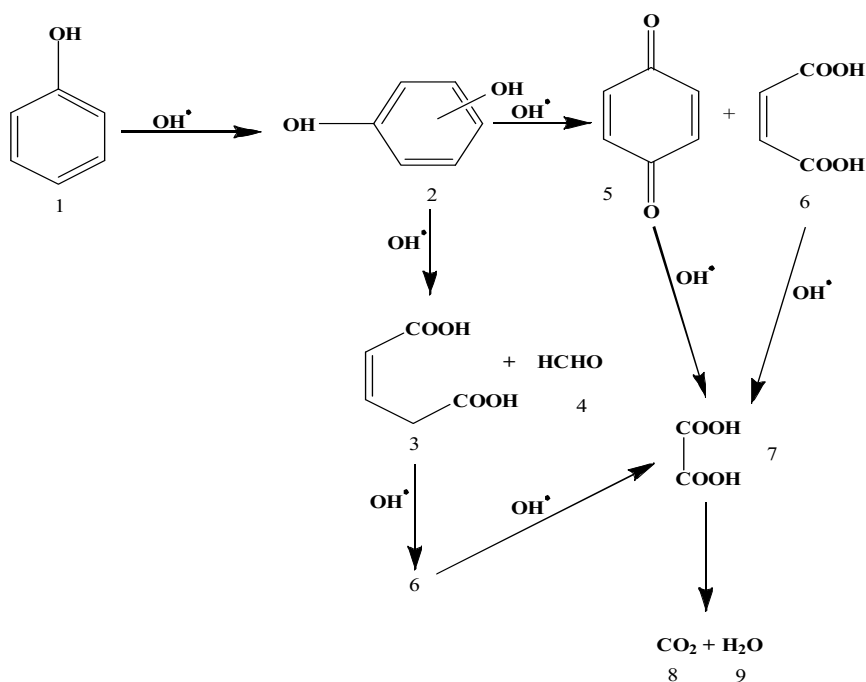


Figure 7. Schematic diagram showing the probable degradation mechanism for phenol [137].

1.9 Objectives and structural planning

This dissertation aims to study the effect of synthesis parameters on the structure of mesoporous TiO_2 and their photocatalytic performance in order to obtain a highly ordered mesoporous structure with high crystallinity and high photocatalytic performance in the treatment of water pollution.

Important reaction parameters including:

- The evaporation temperature, synthesis of mesoporous TiO_2 powders in a range between 25 and 80 °C in order to obtain optimal evaporation temperature.
- The extraction conditions were varied to find the optimal condition in order to remove of the surfactant including: extraction step, extraction temperature a range between 23 and 78 °C, and the number of the extraction steps.
- The optimal molar ratio P123/Ti-source, synthesis of mesoporous TiO_2 powders in a molar range between 0.1-0.4.
- The titanium source, synthesis of mesoporous TiO_2 powders were performed by using two titanium sources, titanium isopropoxide $\text{Ti}(\text{O}^i\text{Pr})_4$ and titanium butoxide $\text{Ti}(\text{O}^n\text{Bu})_4$.

Additionally, influence of transition metal and nonmetal doping on the structure of ordered mesoporous TiO_2 and their photocatalytic performance will be studied.

The synthesized materials have been characterized by SAXS, XRD, STEM, XPS, EPR, ATR-IR, nitrogen adsorption–desorption analysis and UV/vis spectroscopic techniques. The photodegradation of phenol was chosen as a probe reaction to evaluate the photocatalytic activity of materials. Figure 8 represents the schematic structure of this dissertation.

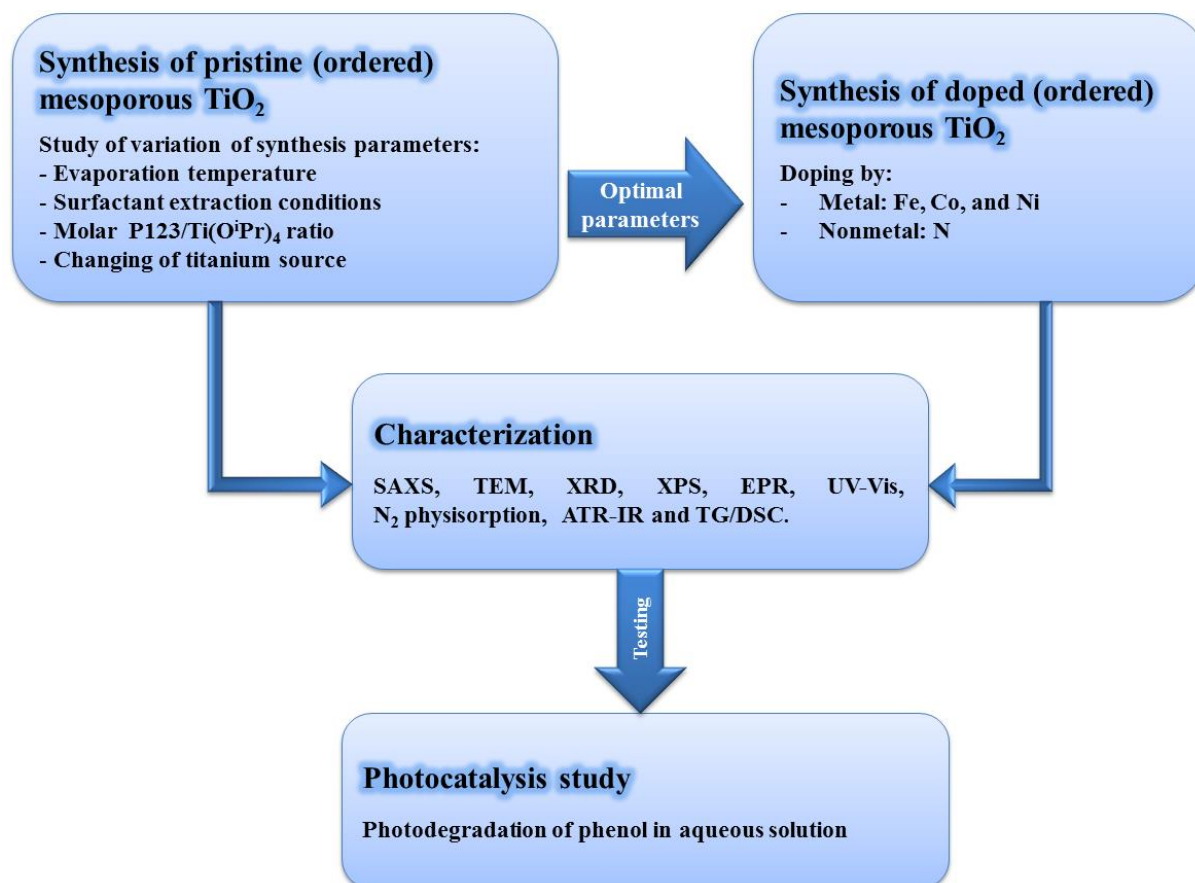


Figure 8. Schematic diagram showing structural planning of the dissertation.

2 Experimental part

2.1 Material synthesis

2.1.1 Materials

Triblock copolymer P123 ($\text{EO}_{20}\text{PO}_{70}\text{EO}_{20}$, Sigma-Aldrich) was used as structure-directing agent (surfactant); titanium isopropoxide ($\text{Ti}(\text{O}^i\text{Pr})_4$, 97%) and titanium butoxide ($\text{Ti}(\text{O}^n\text{Bu})_4$, 97%) purchased from Sigma-Aldrich were used as titanium precursor. Iron (III) chloride (FeCl_3 , 97%), cobalt chloride hexahydrate ($\text{CoCl}_2 \cdot 6\text{H}_2\text{O}$, 98%) were also purchased from Sigma-Aldrich. Nickel chloride (NiCl_2 , 98%) was obtained from MERCK. HCl (37%) were purchased from VWR chemicals, and absolute ethanol was obtained from J. T. Baker. All chemicals were used as received without any further purification.

2.1.2 Synthesis of pristine mesoporous titania

2.1.2.1 General synthesis procedure

1 g of P123 was dissolved in 20 g of ethanol in a two necked round bottom flask (100 mL) at room temperature (RT) under stirring. After 30 min stirring at RT, 2 g of HCl (37%), 3.016 g of the titanium precursor ($\text{Ti}(\text{O}^i\text{Pr})_4$) and 2 g of distilled water were added to the P123 containing solution (molar P123/Ti ratio = 0.0163). After the water addition was finished, the flask was flushed with argon. The two necked round bottom flask containing the clear reaction mixture was immersed in a water bath which was heated to a temperature of 5 °C below the temperature used for solvent evaporation. In general, this step was performed using two parallel round bottles flask at the same time. After the water bath had achieved 40 °C the argon flow was stopped and the solvent removal was started under reduced pressure (250 mbar). The time of solvent evaporation to obtain a viscous gel varied between 2 h and 2 h 15 min. The slightly yellow gels obtained after solvent evaporation were dried in an oven at 40 °C in air atmosphere for 15 to 19 h. The aged materials were deposited as a thin layer on petri dishes by using a spatula and placed in a desiccator. The air in the desiccator was exchanged to ammonia and the solid material was treated at RT with ammonia for 18-22 h to allow the TiO_2 precipitation. The P123 surfactant was removed from the titania framework by treatment of the solid material with boiling ethanol for 1h and the titania was separated from the solution by centrifugation. This procedure was repeated 2 or 4 times. Afterwards the solid material was dried in the oven at 60 °C. Finally, the obtained dried powder was heated from 22 to 450 °C within 6.5 h under argon flow (100 mL/min) followed by treatment under oxygen flow (100 mL/min) for 2 h at 450 °C.

Single synthesis parameters were varied in order to obtain information about their influence on structural characteristics of titania at different synthesis steps.

Surfactant/Ti-ratio

The synthesis of materials was carried out as described in the paragraph (2.1.2.1) but using different amounts of $\text{Ti}(\text{O}^i\text{Pr})_4$. The amount of added $\text{Ti}(\text{O}^i\text{Pr})_4$ varied between 1.225 - 4.66 g leading to molar surfactant/Ti-ratios between 0.0105 and 0.04.

Extraction temperature

The synthesis of materials was carried out as described in the paragraph (2.1.2.1). The amount of $\text{Ti}(\text{O}^i\text{Pr})_4$ was fixed to 3.016 g. P123 surfactant was removed from the titania framework by treatment of the solid material in water bath at different temperatures (25, 60, 80, and 100 °C). For each extraction temperature, the identical synthesis procedure was applied to obtain the material used for the extraction. The temperature inside the ethanol solution was determined as 23, 53, 69, and 78 °C, respectively.

Titanium source

The synthesis of materials were carried out under the same conditions as described in the paragraph (2.1.2.1) but different amounts of $\text{Ti}(\text{O}^n\text{Bu})_4$ (3.018, 3.61, and 4.18 g) were added as titanium precursor instead of $\text{Ti}(\text{O}^i\text{Pr})_4$ in order to obtain molar surfactant/Ti ratios of 0.0194, 0.0163, 0.014 respectively. In addition, the surfactant extraction step was repeated 2 times.

2.1.3 Synthesis of metal-doped mesoporous titania

The synthesis was carried out under the same conditions as described in the paragraph (2.1.2.1) with fixed $\text{Ti}(\text{O}^i\text{Pr})_4$ amount of 3.016 g. In order to synthesis 0.5 and 5 mol% metal - doped TiO_2 appropriate amounts of metals precursors (see Table 1) were added as solid to the synthesis solution directly after addition of $\text{Ti}(\text{O}^i\text{Pr})_4$.

Table 1. Amount of metal source that was used in the synthesis of metal doped titania.

metal source	0.5 mol% metal	5 mol% metal
	metal source mg	
FeCl_3	9.0	90.9
$\text{CoCl}_2 \cdot 6\text{H}_2\text{O}$	12.7	132.8
NiCl_2	6.9	72.3

2.1.4 Synthesis of nitrogen-doped mesoporous titania

In order to study titania crystallization in presence of gaseous ammonia titania synthesis was stopped after surfactant extraction. The synthesis of amorphous titania (material obtained after extraction) was described in the paragraph (2.1.2.1.). To obtain a sufficient amount of amorphous titania, the synthesis was repeated several times followed by mixing of the single fractions. Finally, the obtained mixture was divided in single fractions which were used for study of thermally induced crystallization in ammonia-containing gas flow.

A flow sheet of the experimental set-up used for thermal treatment of the amorphous mesoporous titania in ammonia atmosphere is shown in Figure 9. The quartz tube located in an electrical heated furnace has an internal diameter of 1.6 cm. An open ceramic vessel was placed inside the isothermal zone of the furnace which contained the titania. The ceramic vessel was located on the ground of the tube. The amount for the single experiment varied between 90 and 500 mg.

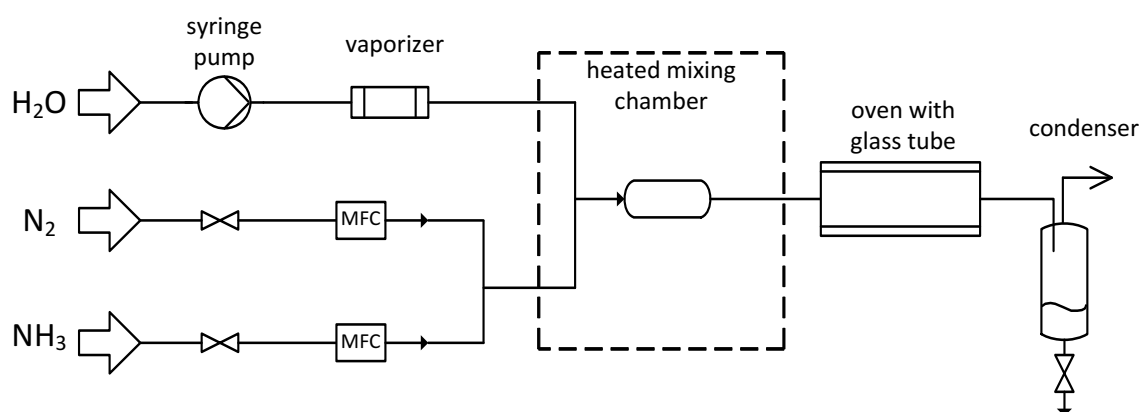


Figure 9. Schematic diagram showing experimental set up for treatment of amorphous mesoporous TiO_2 with gaseous ammonia.

Experiments with different furnace temperatures

The amorphous TiO_2 powder was heated from room temperature to the desired temperature (350, 450, or 550 °C) with a heating rate of 1.2 °C/min in a pure NH_3 flow of 30mL/min. After achieving the desired temperature, the product was kept in the NH_3 atmosphere for another 0.5 h. After that time, nitrogen was switched on and ammonia was switched off and the sample was slowly cooled down to room temperature under N_2 flow. For the temperature of 450 °C one attempt was carried out where the sample was treated in ammonia for 4 h. An aliquot part of the material calcined under ammonia atmosphere was

afterwards treated in an external tube oven under oxygen atmosphere (flow rate = 100 mL/min, heated from 25 to 450 °C using a heating rate of 1.2 °C/min, treatment time: 2 h). In an another experiment, the sample was treated firstly in oxygen atmosphere and afterwards in ammonia atmosphere at 450 °C for 0.5 h in the same manner as described before. The samples obtained at different heating temperatures were referred as N-TiO₂-350NH₃/O₂, N-TiO₂-450NH₃/O₂ and N-TiO₂-550NH₃/O₂.

Experiments with different heating rates

The amorphous TiO₂ powder was heated from 25 °C to 450 °C in NH₃ flow (flow rate = 30 mL/min) with heating rates of 0.6, 1.2, 2.4 °C/min, respectively. After achieving the final temperature the material was kept in the gaseous NH₃ atmosphere for another 0.5 h. Then, the NH₃ flow was replaced by a N₂ flow. The sample was cooled down to RT under nitrogen flow. One part of the powder was again treated with oxygen (flow rate = 100 mL/min) under the same conditions as described before.

Experiments in presence of water

The amorphous TiO₂ material was heated in a mixture of 10 mL/min NH₃ and 20 mL/min N₂ with a heating rate of 1.2 °C/min. After achieving 200 °C gaseous water was introduced with a flow rate of 10 mL/min. After 210 min, the water and the NH₃ flow were stopped and the sample was cooled down under N₂ flow.

In a further experiments, the sample was heated from 25 to 350 or 450 °C with a heating rate of 1.2 °C/min. Between RT and 200 °C the material was flushed with pure NH₃ (10 mL/min). When the temperature had achieved 200 °C, the water flow was switched on (20 mL/min). After achieving the desired temperature (350 or 450 °C), the temperature was held for another 30 min. Afterwards, the water and NH₃ flow were switched off and the sample was cooled down under N₂ flow.

2.1.5 Photocatalytic degradation of phenol in aqueous solution

To study the photocatalytic activity of the materials prepared, photocatalytic degradation of phenol in water was chosen as a test reaction. Phenol and aromatic intermediates (1,2-Dihydroxybenzen, 1,4-Benzochinon, and 1,4-Dihydroxybenzen) were identified and quantified by high performance liquid chromatography.

For comparison of the single samples, a zero order or pseudo first order photo degradation rate of phenol was calculated by the following (Eq. (13 and 14)), respectively:

$$C_t = C_0 - k t \quad (13)$$

$$\ln(C_0 / C_t) = -k t \quad (14)$$

Where C_0 is the initial concentration of phenol (the concentration at time = 0), C_t is the concentration of phenol at the irradiation after time t , and k is the rate constant.

The Photocatalytic degradation of phenol was studied at different experimental conditions.

2.1.5.1 Experiments with a Mercury lamp

The phenol aqueous solution ($C = 0.005$ M) was prepared by dissolving 0.2353 g of the phenol in 0.5 L distilled water. The photochemical reactor consisted of a cylindrical quartz vessel equipped with Hg lamp (Heraeus) located in the middle of the reactor. The Hg lamp was cooled by water flow from the outside. For the tests, 50 mg of the catalyst was dispersed in 300 ml of the phenol aqueous solution. In each experiment, prior to UV irradiation the aqueous TiO_2 suspension containing phenol was continuously agitated in the dark for 1 h in order to obtain an adsorption/desorption equilibrium. The temperature of system was set to 25°C by circulating cooling water through the outer mantle of the cylinder. Oxygen was bubbled through the stirred reaction mixture with a flow rate of 50 ml/min. In order to determine the change in phenol concentration during UV irradiation, 2 ml aliquots of suspension were withdrawn at appropriate times from the reactor by using syringe. The withdrawn liquid was separated from TiO_2 particles by filtration through a $0.2 \mu\text{m}$ (PTFE) Millipore filter and, if necessary, centrifuged to remove the solid catalyst from the sample before HPLC analysis. HPLC analysis was carried out using a Merck-Hitachi with L-4500 diode array detector. HPLC analysis was performed by injection of 5 μl using 10% MeCN in water as mobile phase using a Lichro CART® 250*4 mm column (Merck K GaA). The column temperature was set to 25°C and the flow amounted to 1 ml/min.

2.1.5.2 Experiments with a Xenon lamp

The experiments were carried out in a 50 ml double jacket cylindrical glass reactor. The solution was irradiated with a 1000 W Xenon lamp (LAX 1000) equipped with a 90° deflection reflector system (MS 90) containing a dichroic mirror. The reactor was located in a distance of 12 cm from the deflection reflector system. The lamp intensity reaching the reactor was 105 mW/cm². For experiments with a cut-of filter ($\lambda > 420$ nm) the power decreased to 80 mW/cm². The reaction temperature was set to 25 °C by circulating cooling water through an outer cooling mantle. Oxygen was fed to the bottom of the reactor by means of a small tube with a flow rate of 10 ml/min. 30 mg of the catalyst were dispersed in 30 mL of 0.0002 M phenol aqueous solution. Prior to exposure to the radiation, the TiO₂ and phenol containing suspension was stirred in the dark for 30 min. During irradiation with light, the reaction mixture was continuously stirred to keep TiO₂ particles in suspension. In order to monitor phenol concentration during irradiation, 0.3 ml aliquots of the suspension were regularly withdrawn from the reactor, filtrated from TiO₂ particles and analyzed by HPLC. Additionally, samples were withdrawn before and after stirring the suspension in dark in order to account for phenol adsorbed on titania. HPLC analysis was performed on an Agilent instrument equipped with a L-4500 diode array detector and a Lichro Rp-18 CART[®] 250*4 mm column (Merck K GaA). The injection volume was 5 µl. 10% MeCN in water was used as a mobile phase and the flow rate was set to 1 ml/min. The analysis was performed at 25 °C.

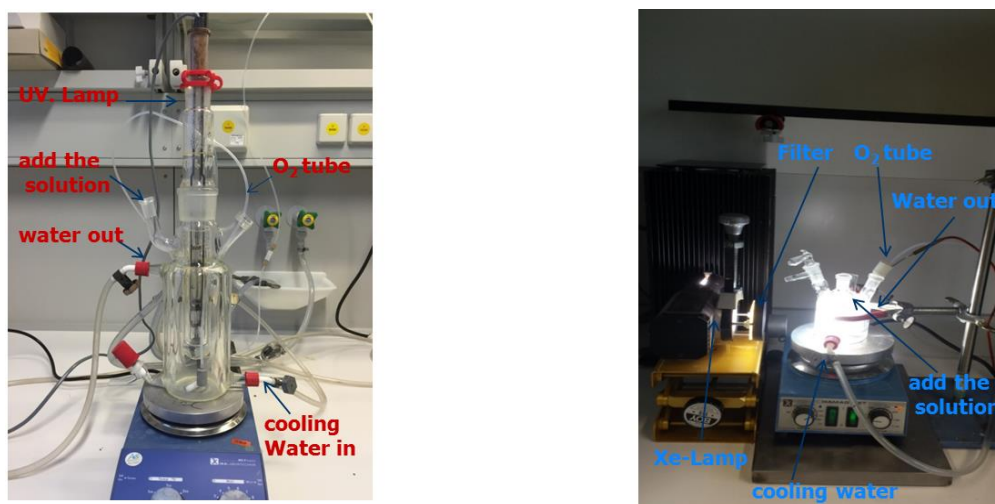


Figure 10. Photos of the experimental set up used for the degradation of phenol with mesoporous titania using a) Mercury lamp and b) Xenon lamp.

2.2 Characterization

Different analysis and characterization techniques have been employed to characterize and describe structural, morphological and physicochemical properties of synthesized materials, which provide information about phase composition, crystallinity, crystallite size, optical properties, surface structure, textural properties, morphology, and other characteristic features. Moreover, they give information about the nature and chemical state of dopant. These techniques involve the small angle X-ray diffraction (SAXS), transmission electron microscopy (TEM), X-ray diffraction (XRD), X-ray photoelectron spectroscopy (XPS), electron paramagnetic resonance (EPR) spectroscopy, UV/visible diffuse reflectance spectra (DRS), thermogravimetry (TG) and differential scanning calorimetry (DSC) and nitrogen adsorption-desorption analysis. The procedure of each technique used in the current study is briefly explained.

2.2.1 Small-angle X-ray scattering (SAXS)

SAXS measurements were carried out using a Kratky-type instrument (SAXSess, Anton Paar, Austria) operated at 40 kV and 50 mA in slit collimation using a two-dimensional CCD detector cooled to $-40\text{ }^{\circ}\text{C}$ or image plates digitalized with a Cyclone Plus (Perkin Elmer). A Göbel mirror was used to convert a divergent polychromatic X-ray beam into a collimated line-shaped beam of $\text{CuK}\alpha$ radiation ($\lambda = 0.154\text{ nm}$). Slit collimation of the primary beam was aimed to increase the flux and to improve the signal quality. The sample cell consisted of a metal body with two windows for the beam. The samples were sealed between two layers of scotch® tape. Scattering profiles of the mesoporous materials were obtained by subtraction of the detector current background and the scattering pattern of scotch® tape from the experimental scattering patterns. The 2D scattering patterns were converted with SAXS Quant software (Anton Paar) into one-dimensional scattering curves as a function of the magnitude of the scattering vector $q = (4\pi/\lambda) \sin(\theta/2)$. Correction of the instrumental broadening effects (smearing) was carried out with SAXS Quant software using the slit length profile determined in a separate experiment. All SAXS measurements were carried out at $25\text{ }^{\circ}\text{C}$.

2.2.2 Transmission electron microscopy (TEM)

STEM measurements were performed in an aberration-corrected JEM-ARM200F instrument (JEOL, Corrector: CEOS) operated at 200 kV. The microscope was equipped with a JED-2300 (JEOL) energy dispersive X-ray spectrometer (EDXS). The aberration-corrected STEM imaging (High-Angle Annular Dark Field (HAADF) and Annular Bright Field (ABF)) was performed under the following conditions. HAADF and ABF were both done with a spot

size of approximately 0.13 nm, a convergence angle of 30-36° and collection semi-angles for HAADF and ABF of 90-170 mrad and 11-22 mrad, respectively. The samples were supported on holey carbon Cu or Ni-grids (mesh 300) and transferred into the microscope without any pretreatment.

2.2.3 Powder X-ray diffraction (XRD)

XRD powder patterns were recorded either on a Panalytical X'Pert diffractometer equipped with a Xcelerator detector or on a Panalytical Empyrean diffractometer equipped with a PIXcel 3D detector system both used with automatic divergence slits and Cu K α 1/ α 2 radiation (40 kV, 40 mA; λ = 0.015406 nm, 0.0154443 nm). Cu beta-radiation was excluded by using nickel filter foil. The measurements were performed in 0.0167° steps and 25 s of data collecting time per step. Phase analysis was done with the Panalytical HighScore Plus software package using the PDF-2 2015 database of the International Center of Diffraction Data (ICDD).

The crystallite sizes were calculated by applying the Scherrer equation (Eq. (15)) and the usage of the integral breadth under the assumption of spherically shaped crystallites.

$$D = K\lambda / \beta \cos \theta \quad (15)$$

K is set to 1.0747, λ is the x-ray wavelength (λ = 0.015406 nm, 0.0154443 nm) for (CuK α 1 K α 2 radiation), β is Integral breadth in radians (area peak/Int. peak), θ is the angle in radians. An average value of the calculated sizes of diffraction peaks between $20 \leq 2\theta \leq 50^\circ$ is presented here.

2.2.4 X-ray photoelectron spectroscopy (XPS)

The oxidation states and the surface compositions were determined by X-ray photoelectron spectroscopy (XPS). The measurements were performed with an ESCALAB 220iXL (ThermoFisherScientific) with monochromatic Al K λ radiation (E = 1486.6 eV). The samples were fixed on a stainless steel sample holder with double adhesive carbon tape. For charge compensation a flood gun was used, the spectra were referenced to the C1s peak at 284.8 eV. The error range for the determination of the electron binding energy is approximately ± 0.2 eV. After background subtraction the peaks were fitted with Gaussian–Lorentzian curves to determine the positions and the areas of the peaks. The surface composition was calculated from the peak areas divided by the element- specific Scofield factor and the transmission function of the spectrometer.

2.2.5 N₂ physisorption measurement

Nitrogen adsorption-desorption isotherms were collected at $-196\text{ }^{\circ}\text{C}$ on BELSORP-mini II (BEL Japan, Inc.). The specific surface area (BET) and pore size distribution were calculated from the adsorption and desorption branches of the isotherm, respectively, applying the Brunauer, Emmet and Teller equation for the N₂ relative pressure range of $0.05 < P/P_0 < 0.3$ and the BJH method for the pressure range of $0.3 < P/P_0 < 0.99$. Some samples were measured by the apparatus ASAP 2020 (USA). The samples were pretreatment before measure by heating to $200\text{ }^{\circ}\text{C}$.

2.2.6 UV-Vis spectroscopy (UV/Vis)

UV/Vis spectra were measured using the UV-Visible spectrometer of the type AvaSpec-2048 Fiber-Optic Spectrometer (Avantes) using the FCR7UV-400-400-2-Me-HT Fiber optic and pure barium sulphate BaSO₄ powder as white reflection standard of referencing.

The optical band gap (BG) energies values of un-doped and doped mesoporous TiO₂ were calculated from the Tauc's plot [138], which shows the relationship between $(F(R)\cdot hv)^{1/2}$ and hv for indirect transition. $F(R)$ is the Kubelka-Munk function derived from reflectance spectra where $F(R) = (1-R)^2/2R$ and hv is the photon energy. Plotting $(F(R)\cdot hv)^{1/2}$ against hv based on the spectral response.

2.2.7 Electron paramagnetic resonance (EPR)

EPR spectra were measured at 300 K on a Bruker EMX CW-micro X-band spectrometer ($\nu \approx 9.8\text{ GHz}$) with a microwave power of 6.9 mW , a modulation frequency of 100 kHz and modulation amplitude up to 5 G .

2.2.8 Attenuated total reflection infrared spectroscopy (ATR-IR)

ATR-IR spectra were acquired using an ALPHA FTIR-spectrometer from Bruker. The data collection consisted of 64 scans per spectrum with a resolution of 4 cm^{-1} . The mesoporous titania powder was deposited on the ATR-crystal without any further pretreatment.

2.2.9 Thermogravimetric analyses (TGA) and differential scanning calorimetry (DSC) measurements

Thermogravimetric analyses (TGA) and differential scanning calorimetry (DSC) measurements were performed simultaneously on a Netzsch STA 449 F3 Jupiter device in the temperature range of $25\text{-}500\text{ }^{\circ}\text{C}$ with heating rates of 10 or 20 K/min in nitrogen or compressed air atmosphere, respectively.

3 Results and discussion

3.1 Pristine ordered mesoporous titanium dioxide

3.1.1 Variation of synthesis parameters

The whole synthesis process consists of different steps which includes (a) dissolving the materials in ethanol, (b) evaporation of the solvent under reduced pressure, (c) treatment of the obtained mesophase with ammonia vapor, (d) surfactant extraction in ethanol, and (e) thermal treatment in inert gas and oxygen. In order to study the influence of synthesis parameters on formation of ordered mesoporous TiO_2 , various parameters were systematically varied.

3.1.1.1 Evaporation temperature

Firstly, the synthesis of titania was performed at different evaporation temperature (25, 40, 60, 70, and 80 °C). SAXS patterns monitored after treatment of the mesophase with ammonia (synthesis step c) are shown in Figure 11A. Independent of the applied solvent evaporation temperature, all patterns exhibited an intense first reflection and a weak second reflection which indicate a hexagonal ordered mesoporous structure after ammonia treatment [90]. The d_{100} spacing ranged between 13.1 nm (60 °C) and 10.2 nm (70 °C) and was generally higher for samples synthesized with solvent evaporation temperatures between 25 and 60 °C. A decrease of d_{100} spacing with increasing evaporation temperature was already observed previously using CTAB as surfactant and explained by a more complete solvent removal at higher temperatures connected with an extended condensation degree of the inorganic network [139].

Figure 11B displays the SAXS profiles after removal of the surfactant in boiling ethanol. Differences in d_{100} spacing for different evaporation temperatures which were observed after ammonia treatment were still found in the SAXS patterns. However, all reflections are shifted to slightly higher q values. The d_{100} spacing ranged now between 12.1 and 10.7 nm (see also Figure 11). The second reflection was most intense for samples where the solvent was evaporated at 40 or 60 °C.

The final thermal treatment (synthesis step e) led to the largest shift of the SAXS reflexes associated with a broadening (Figure 11C). The d_{100} spacing of materials synthesized with solvent evaporation temperatures between 25 and 60 °C peaked between 9 and 10 nm. The SAXS patterns of the materials synthesized with the evaporation temperatures higher than 60 °C exhibited only a broad hump instead of a reflection peak. After thermal treatment,

the second reflection could be detected only for the materials synthesized with solvent evaporation temperatures of 40 or 60 °C. A broadening of the SAXS reflection was explained previously by a larger distribution of the lattice parameter or a reduced size of the coherent scattering areas [140].

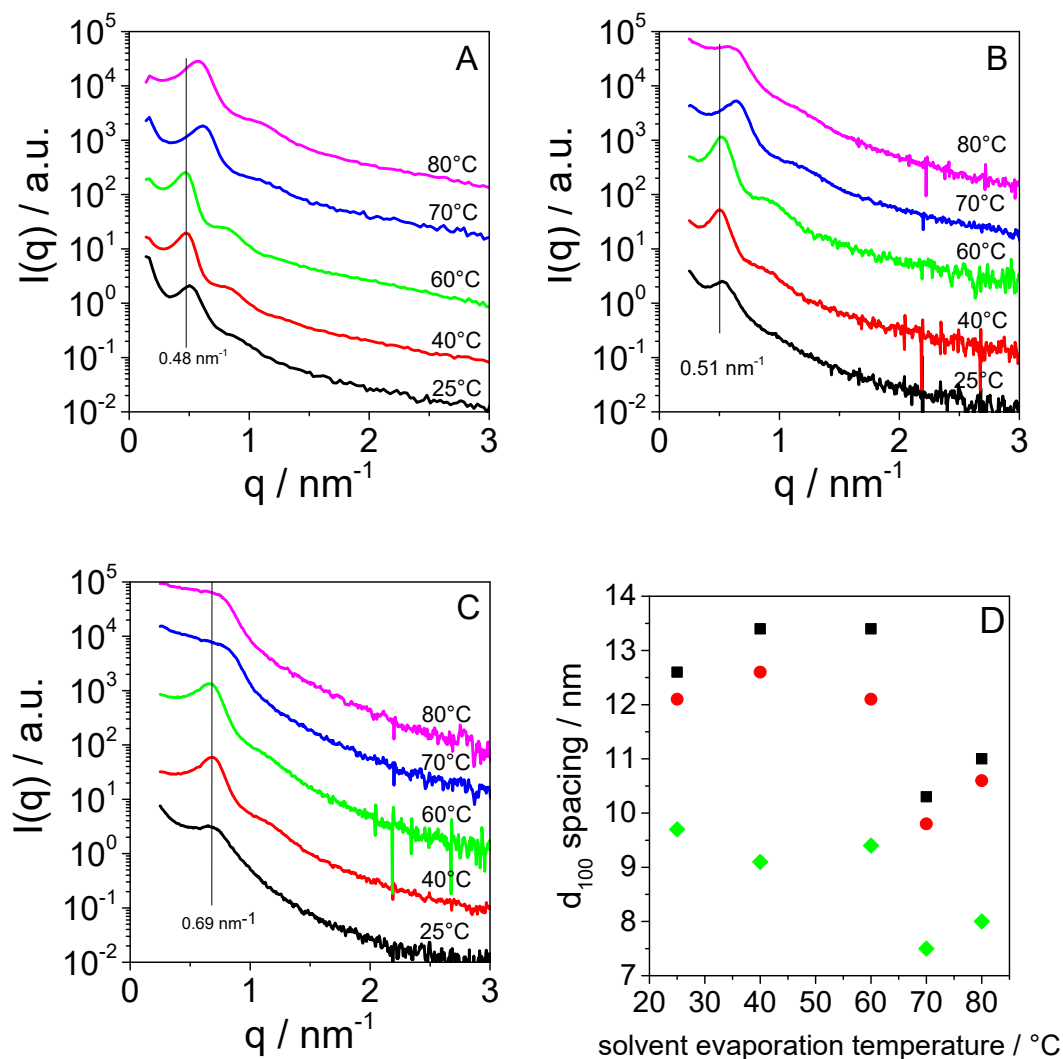


Figure 11. Influence of the solvent evaporation temperature on the SAXS patterns recorded at different steps of material synthesis A) after ammonia treatment, B) after surfactant removal, C) after thermal treatment; and D) influence of single synthesis step on d_{100} spacing (■ - after ammonia treatment, ● - after surfactant removal, and ◆ - after thermal treatment (the value of d_{100} after thermal treatment for samples formed with a solvent evaporation temperature of 70 and 80 °C was taken from the inflection point, the single SAXS pattern were shifted by multiplication of the data points using a constant factor; synthesis conditions: molar $\text{P123}/(\text{TiO}^{\text{I}}\text{Pr})_4 = 0.0163$, $T_{\text{extrac}} = 78 \text{ °C}$ (4 times), calcination: 25 – 450 °C with 1.2 °C/min in Ar than 2 h at 450 °C, 25 – 450 °C with 1.2 °C/min in O_2 than 2 h at 450 °C).

Because the SAXS patterns alone do not allow the unambiguous assignment of the morphology and to support these results, HAADF-STEM images of the materials synthesized at solvent evaporation temperature 40 and 70 °C were also collected. In these samples the largest difference in d_{100} spacing was detected by SAXS. The corresponding micrographs are

shown in Figure 12 and in Figure A1 (see Appendix) in higher magnification. The images of the materials obtained after the ammonia treatment showed a porous solid with a partially hexagonal ordered mesostructure (Figure 12A and Figure 12D). Differences in mesoporous ordering between both samples seem to be relatively low. For the sample where the solvent was evaporated at 40 °C (2A) the mesoporous framework was built from small TiO_x units and no long range order could be found (Figure A1, Appendix). When the solvent evaporation temperature increased to 70 °C, the precipitated titania exhibited already small crystalline domains (Figure A1D). EDX measurements showed that both samples contained, beside Ti and O, also larger amounts of carbon and a low amount of chlorine attributed to the surfactant and to NH_4Cl , respectively (Figure A2 and Figure A3).

The STEM-HAADF micrographs of both samples recorded after removing the surfactant in boiling ethanol are shown in Figure 12B and Figure 12E. The images reveal that the materials preserved their ordered porosity. The degree of order seems to be higher for the sample shown in Figure 12B where the solvent was evaporated at 40 °C. Here, in the center-right of the image close-packed hexagonal ordered tubular pores are clearly visible. In Figure 12E the pores seem to vary in size and shape to a larger extent compared to the ones that were found in the material after solvent evaporation at 40 °C. In addition, highly ordered domains have not been observed after surfactant removal at 70 °C. Generally, particles forming the walls of the mesoporous framework appeared to be more crystalline after surfactant removing and are formed by several crystal planes which are randomly orientated across the particle (see Appendix Figure A1B and Figure A1E). Crystallinity was obviously higher for the sample prepared with higher solvent evaporation temperature. EDX spectra of both samples (see Appendix Figure A4 and Figure A5) show that the carbon content after surfactant extraction was obviously lower as obtained after ammonia treatment and that the chloride was nearly complete removed during this step. Figure 12C and Figure 12F show representative STEM-HAADF micrographs of TiO_2 framework recorded from the samples after thermal treatment at 450 °C. Evidently, mesoporosity is preserved in both materials, but the order seemed to be lower than before calcination, suggesting that thermal treatment influenced both pore size and wall thickness. This loss in ordering is assumed to be higher for the sample synthesized at 70 °C solvent evaporation temperature compared to that obtained at 40 °C. In both samples the titania framework was now built from small crystalline TiO_2 grains which are grown together during the thermal treatment (see Appendix Figure A1C and Figure A1F). EDX spectra (see Appendix Figure A6 and Figure A7) indicate that carbon content was decreased after treatment with oxygen at 450 °C but the samples still contained carbon.

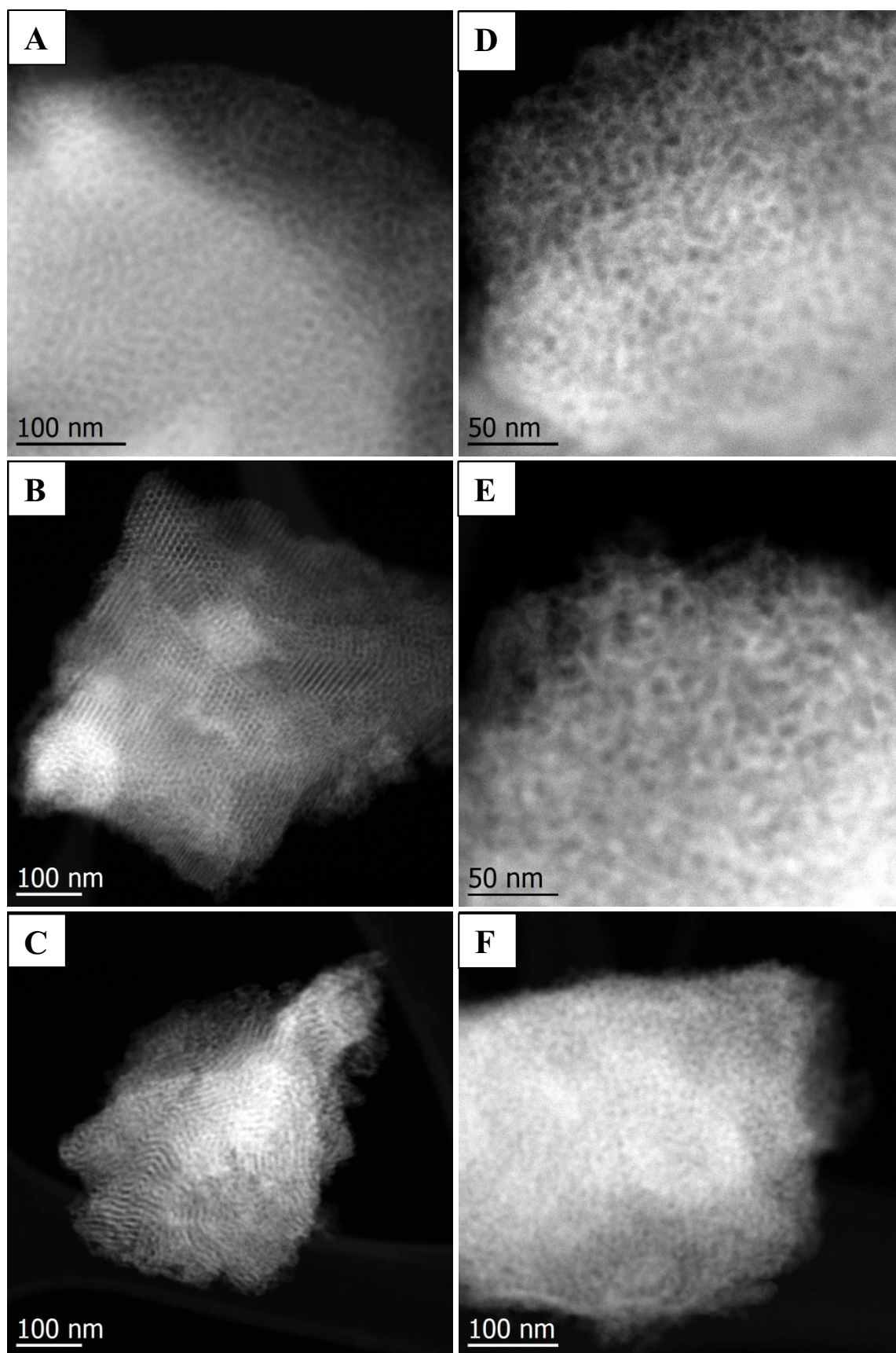
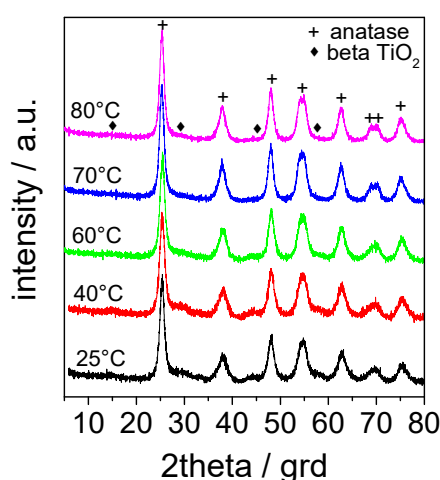


Figure 12. HAADF-STEM images of the material where the solvent was evaporated at 40 °C (A,B,C) and 70 °C (D,E,F), respectively; (A,D) after treatment of the sol with ammonia, (B,E) after surfactant extraction, and (C,F) after thermal treatment; (synthesis conditions: molar $\text{P123}/(\text{TiO}^{\text{i}}\text{Pr})_4 = 0.0163$, $T_{\text{extrac}} = 78\text{ °C}$ (4 times), calcination: 25 – 450 °C with 1.2 °C/min in Ar than 2 h at 450 °C, 25 – 450 °C with 1.2 °C/min in O_2 than 2 h at 450 °C).

XRD powder patterns of the materials obtained after thermal treatment (C) are presented in Figure 13. XRD patterns of these materials showed intense reflections of anatase TiO_2 (ICDD 03-065-5714) together with minor reflections attributed to $\beta\text{-TiO}_2$ (ICDD 00-035-0088) independent of the temperature used for solvent evaporation. Rietveld refinement was applied to analyze the diffraction data quantitatively. The anatase content varied between 73 and 80%, however, an influence of the solvent evaporation temperature on phase composition could not be derived. The average domain size of crystal synthesis parameters after calcination determined by the Scherrer equation increased with rising evaporation temperature from 3.9 (25 °C) to 5.4 nm (80 °C) (see Table 2).



data in Table 2 also show that BET surface and pore volume obviously decreased during the calcination step (see also Appendix Figure A8).

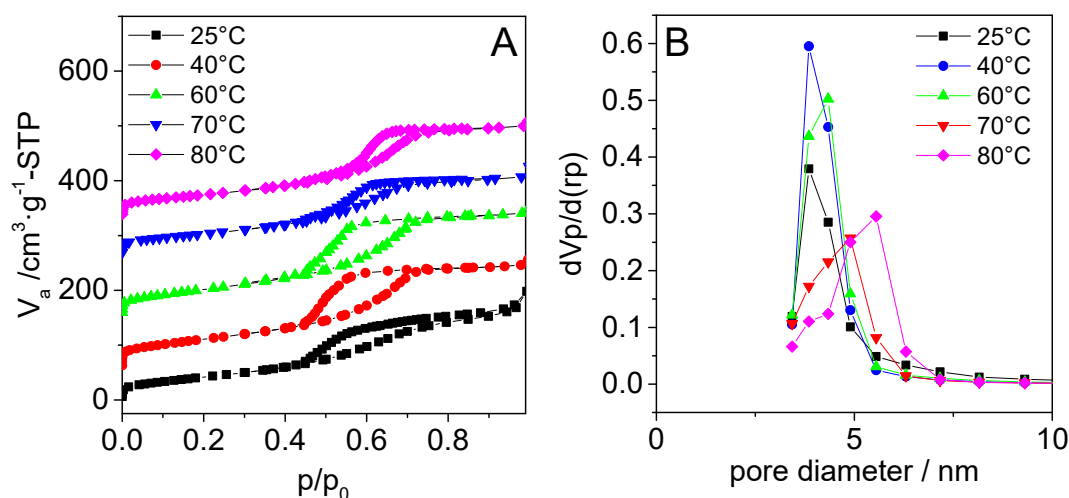


Figure 14. A) Adsorption-desorption isotherms of calcined titania materials synthesized with different evaporation temperature and B) Pore size distribution obtained by BJH method (synthesis conditions: molar $\text{P123}/(\text{TiO}^i\text{Pr})_4 = 0.0163$, $T_{\text{extrac}} = 78^\circ\text{C}$ (4 times), calcination: $25 - 450^\circ\text{C}$ with $1.2^\circ\text{C}/\text{min}$ in Ar than 2 h at 450°C , $25 - 450^\circ\text{C}$ with $1.2^\circ\text{C}/\text{min}$ in O_2 than 2 h at 450°C).

Table 2. Summary of the structure characteristics for materials synthesized with different solvent evaporation temperatures (molar $\text{P123}/\text{Ti}(\text{O}^i\text{Pr})_4$ ratio = 0.0163, calcination at 450°C).

temperature $^\circ\text{C}$	d_{100} nm	a_{hex}^{**} nm	BET $\text{m}^2 \cdot \text{g}^{-1}$	V_p $\text{cm}^3 \cdot \text{g}^{-1}$	d_{pore} nm	$d_{\text{cryst.}}$ nm	band gap eV
25	9.6 (12.1)*	11.1 (14.0)*	178	0.34	3.9	3.9	3.15
40	9.2 (12.6)*	10.6 (14.0)*	202 (452)*	0.35 (1.01)*	3.9 (3.9)*	3.9 -	3.16
60	9.6 (12.1)*	11.1 (14.0)*	202	0.36	4.3	4.3	3.15
70	(9.9)*	(10.6)*	147 (394)*	0.27	4.9	5.7	3.08
80	(10.6)*	(11.1)*	151	0.30	5.6	5.4	3.13

*value in brackets shows results obtained after surfactant removal before calcination; ** $a_{\text{hex}} = 2 \cdot d_{100}/3^{1/2}$

UV/Vis diffuse reflectance spectra of the calcined samples are presented in Figure 15. The band gap (E_g) energies were estimated from the powder spectra using the transformed Kubelka-Munk function $[F(R) \cdot hv]^{0.5}$ which was plotted versus the photon energy hv [143]. The calculated band gaps were in the range between 3.08 and 3.15 eV (see also Table 2). In contrast to P25, the UV/Vis spectra of the mesoporous materials showed also some light absorption in the visible light range.

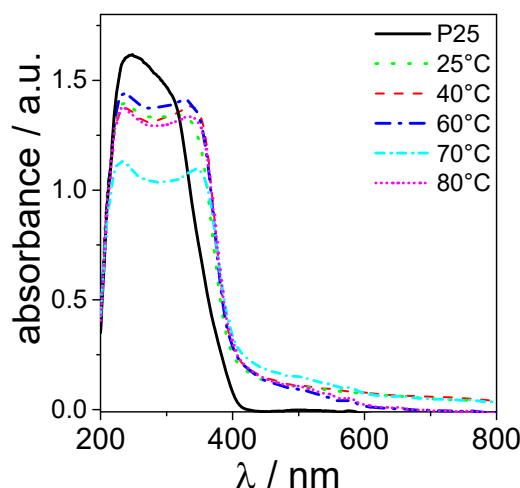


Figure 15. UV/Vis Spectra of samples synthesized with different solvent evaporation temperature after thermal treatment.

The visible light absorption might be attributed to the presence of carbon residuals originating from residuals of the titanium precursor and/or the surfactant which remain(s) in the sample despite the final treatment with oxygen. To prove this assumption the sample synthesized with solvent evaporation temperature at 60 °C was investigated by XPS. The corresponding XPS spectra are shown in Figure 16. XPS analysis indicated to presence of both carbon residuals and nitrogen on titania surface. This was surprising because nitrogen was not mentioned in previous reports using the applied synthesis method [89, 90]. Probably, the nitrogen was introduced by the titania precipitation step as adsorbed ammonia or the formed ammonium chloride was not completely removed during the treatment with boiling ethanol. Doping of titania by addition of ammonium chloride to the synthesis mixture was already reported previously for synthesis of iron-nitrogen doped titania nanoparticles [144]. XPS spectra of the N(1s) region showed peaks located at 399.5 and 400.7 eV indicating the presence of O-Ti-N and Ti-N-O bonds, respectively [145]. The main peak in the C(1s) spectra was located at 284.4 eV and could be assigned as carbon residues from the carbon sources [146]. The total nitrogen and carbon content was very low and below the detection limit of the H, C, N analyzer (nitrogen 0.02 wt.%, carbon 0.002 wt.%) where only hydrogen was detected in the range between 0.24 – 0.40 wt.%. It was postulated that carbon residues from the P123 surfactant were removed from the mesoporous titania below 400 °C [147]. However, total elimination of organic carbon residues from titania surface proceeds at temperatures much higher as applied for calcination (700 °C or higher) [148].

Finally, the characterization results showed that the temperature of solvent evaporation had affected the structural characteristics of the finally obtained material. It was clear that the best evaporation temperatures were 40 and 60 °C.

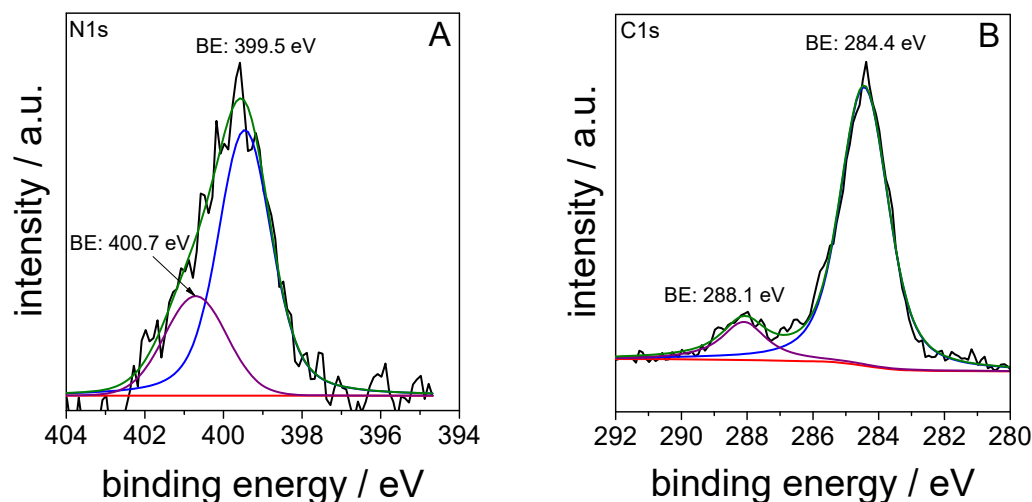


Figure 16. High resolution XPS spectra from calcined material synthesized with solvent evaporation temperature of 60 °C A) N 1s and B) C1s.

In order to investigate in which extent the structural parameters varied at repeated synthesis under approximately identical synthesis parameters, the titania synthesis was repeated with an evaporation temperature at 40 °C several times. Figure 17 compares the SAXS pattern of these materials after ammonia treatment, after surfactant extraction and after calcination. All SAXS patterns after ammonia treatment exhibited an intense first reflection and a weak second reflection which indicate a hexagonal ordered mesoporous structure. Slight differences were observed in the position of reflection peak maximum (Figure 17A). The removal of surfactant did not lead to a clear change of the shape of the SAXS pattern. The surfactant extraction shifted the position of all reflections to slightly larger q values. (Figure 17B). However, clear differences in SAXS pattern were obtained after the thermal treatment. In some samples the mesoporous ordering was still there, in other samples the mesoporous ordering was lost (Figure 17C). At the same time, BET surface area varied strongly (232.5, 223, 202, 182, 181, 168, 166, and 155 m²/g). Otherwise, the phase composition in all material was comparable. Until now, the reasons for the structural differences of the materials synthesized at nearly identical conditions are still unclear.

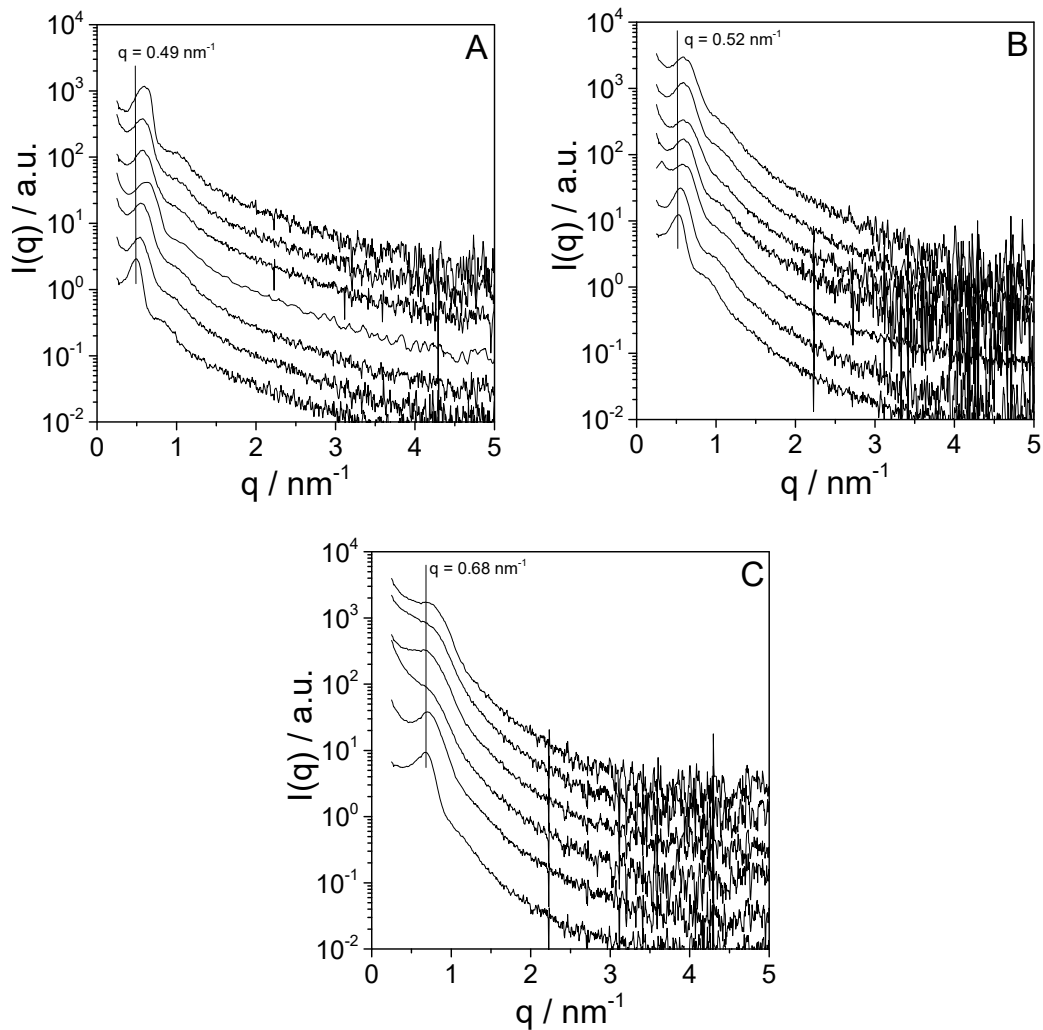


Figure 17. Influence of the repetition of synthesis mesoporous TiO_2 on the SAXS patterns A) after ammonia treatment, B) after surfactant removal, C) after thermal treatment. (molar $\text{P123}/(\text{TiO}^i\text{Pr})_4 = 0.0163$, $T_{\text{evap}} = 40^\circ\text{C}$, $T_{\text{extrac}} = 78^\circ\text{C}$ (4 times), calcination: $25 - 450^\circ\text{C}$ with $1.2^\circ\text{C}/\text{min}$ in Ar than 2 h at 450°C , $25 - 450^\circ\text{C}$ with $1.2^\circ\text{C}/\text{min}$ in O_2 than 2 h at 450°C).

The degree of order of the material obtained after calcination might be influenced from the mesoporous structure obtained after evaporation step as indicated by the small differences of SAXS pattern of precipitation of titania with ammonia. Only those materials with highest degree of order after ammonia treatment might conserve the ordered structure after thermal treatment.

Furthermore, it was investigated whether ordered mesoporous titania can be synthesized without gel aging. For that reason, the gel obtained after solvent evaporation was treated with ammonia directly after finishing this process. In all other studies presented in this work, the aging time of the gel was between 15 and 19 h. SAXS patterns of the samples without gel aging obtained after surfactant extraction and after calcination are presented in Figure 18. The pattern shows that hexagonal ordered mesoporous TiO_2 can be synthesized without the aging

step. BET surface area of the calcined sample was high ($221 \text{ m}^2/\text{g}$) and the results supports conclusion derived from SAXS. Also TiO_2 phase composition was not influenced by gel aging time. The finding that ordered mesoporous TiO_2 can be synthesized without gel aging will shorten the time for the synthesis process considerably.

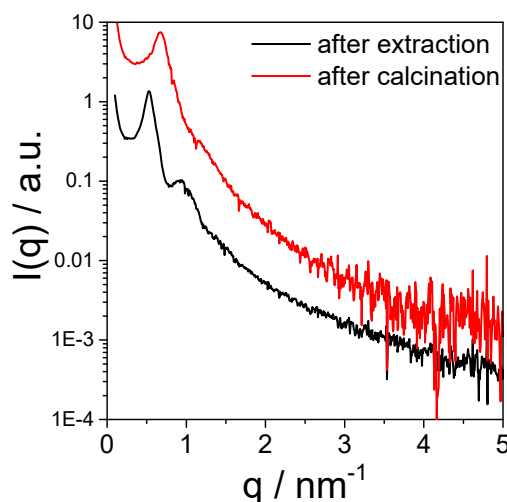


Figure 18. SAXS pattern of the sample synthesized without gel aging time of 15 h.(molar $\text{P123}/(\text{TiO}^i\text{Pr})_4 = 0.0163$, $T_{\text{evap}} = 40 \text{ }^\circ\text{C}$, $T_{\text{extrac}} = 78 \text{ }^\circ\text{C}$ (2 times), calcination: $25 - 450 \text{ }^\circ\text{C}$ with $1.2 \text{ }^\circ\text{C}/\text{min}$ in Ar than 2 h at $450 \text{ }^\circ\text{C}$, $25 - 450 \text{ }^\circ\text{C}$ with $1.2 \text{ }^\circ\text{C}/\text{min}$ in O_2 than 2 h at $450 \text{ }^\circ\text{C}$).

3.1.1.2 Surfactant extraction conditions

In order to investigate the influence of surfactant extraction on the ordering of mesostructure, mesoporous titania was prepared using different temperatures and different repetitions of surfactant extraction. At first, titania synthesis with and without surfactant extraction was performed. The material with surfactant extraction was referred as $\text{TiO}_2\text{-E}$ and that without extraction was referred as $\text{TiO}_2\text{-W}$. The SAXS pattern in Figure 19A showed a mesoporous ordering of the material obtained ammonia treatment. When the surfactant was extracted before calcination, the position of the d_{100} reflection was shifted to higher q -values. The presence of the d_{100} reflection proves that the material contains ordered mesoporous domains. For the material prepared without surfactant extraction, the intensity of the SAXS pattern decreases with increasing q values nearly continuously. This indicates that for the material prepared without surfactant extraction the mesoporous ordering was destroyed during the thermal treatment which lead to a disordered structure. This result agrees with a study presented by Dai et al. [149]. From Nitrogen adsorption–desorption measurements (Figure 19B), it can be seen that the samples exhibit a type IV isotherm, and H2 type hysteresis characteristic of mesoporous materials according to the IUPAC classification [141]. The inflection of isotherm and its sharpness is reduced and shift toward P/P_0 0.5 for the sample

TiO₂-W and was found to be 0.4 for the sample TiO₂-E. The surface areas of the prepared samples TiO₂-W and TiO₂-E are 180.9 and 232.5 m²/g, respectively. This means the removal of the surfactant leads to an increase in surface area. The average pore diameter was determined by using the BJH method and was found to be 7.3 nm for TiO₂-W and 5.6 nm for TiO₂-E, respectively. Calcination of TiO₂-W led to structural collapse during heating. It is assumed that the template burn rapidly (explode) in the pores. This led to rip apart and collapse of the ordered structure. The collapse of the pores might be also responsible for the decrease in BET surface area.

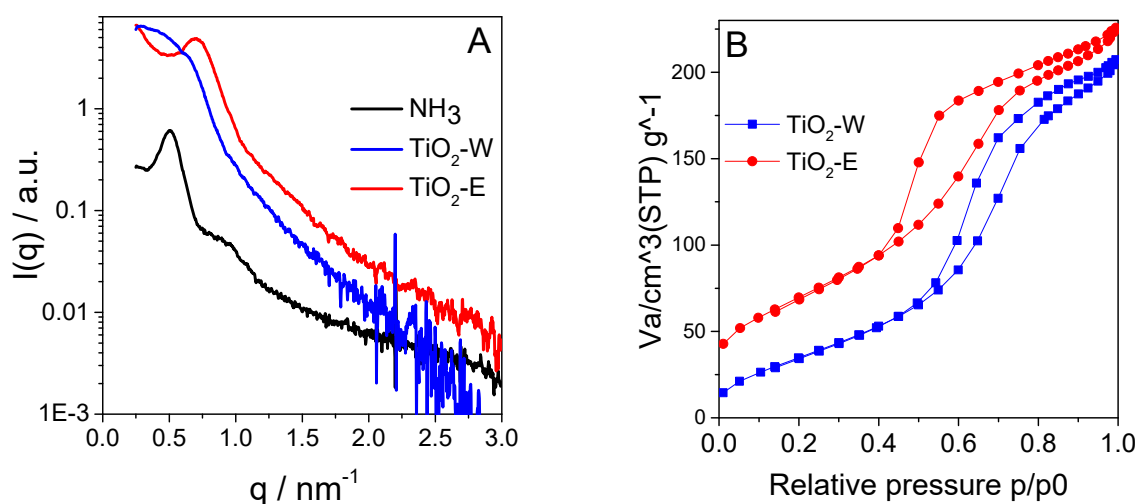


Figure 19. A) SAXS patterns and B) Nitrogen adsorption–desorption isotherms for the powders without surfactant P123 extraction (TiO₂-W) and with surfactant P123 extraction (TiO₂-E); (synthesis conditions: molar P123/(TiOⁱPr)₄ = 0.0163, T_{evap} = 40 °C, T_{extrac} = 78 °C (4 times), calcination: 25 – 450 °C with 1.2 °C/min in Ar than 2 h at 450 °C, 25 – 450 °C with 1.2 °C/min in O₂ than 2 h at 450 °C).

To obtain more information about the surfactant removal step, simultaneous TG and DSC measurements were carried out before and after extraction. In Figure 20A, TG/DSC curves are presented for the sample before extraction. There, mass loss starts above 100 °C with an endothermic event, and ends slightly above 300 °C with a sharp exothermic event, which can be assigned to evaporating and burning of polymer P123 [150, 151], yielding a total weight loss of about 64.5%. In Figure 20B(a-d), TG/DSC curves are shown for the materials prepared with one, two, three or four extractions. Weight losses of about 21.9, 19.8, 18.8, and 18.0 %, respectively, can be observed. Mass loss starts always at temperatures between 100–150 °C with endothermic phenomena, which was assigned to evaporation of water and organic solvent [152].

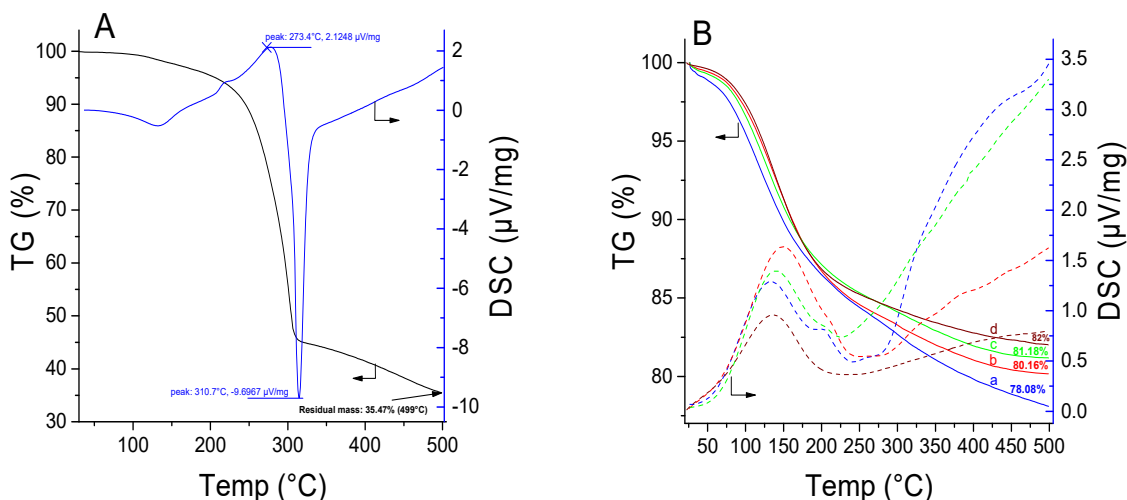


Figure 20. Simultaneous TG/DSC curves in compressed air atmosphere A) for the materials P123/Ti(OⁱPr)₄ (molar ratio: 0.0163) before and after extraction using ethanol (temperature of extraction: 78 °C, stirred at 300-rpm) and B) for P123/Ti(OⁱPr)₄ (molar ratio: 0.0163) after a) first, b) second, c) third, d) fourth extraction.

In further experiments, the influence of the extraction temperature on the surfactant removal was studied. For that reason the titania synthesis was repeated four times, and the surfactant was extracted two times in ethanol at 23, 53, 69, and 78 °C. In general, Figure 21A(a-d) compared the weight loss of the materials. The weight loss decreases slightly from 23.5 to 19 % when the extraction temperature was increased from 23 to 78 °C. It can be observed due to endothermic events. These events are observed between 100-150 °C that correspond to evaporation of water and organic solvents [152]. On the other hand, TG/DSC curves in compressed air (Figure 21B(a-d)) did not exhibit the same shape as the curves depicted in Figure 21A(a-d) responding to the same samples in nitrogen atmosphere. The difference in thermal behavior of samples under nitrogen and air heating was due to the thermo-oxidative decomposition of the surfactant P123 under air. Figure 21B(a-d) showed weight loss of about 28.2, 22.7 and 23.1% for the samples at 23, 53, and 69 °C, respectively. Further mass loss was detected above 250 °C with exothermic events, which can be assigned to burning of polymer P123. In contract, for the sample at 78 °C, mass loss was at around 125 °C with an endothermic event. This can be referred to the evaporation of water and organic solvent [152].

Based on above findings, it can be found that ethanol boiling temperature (78 °C) was the best extraction temperature to remove the surfactant from samples.

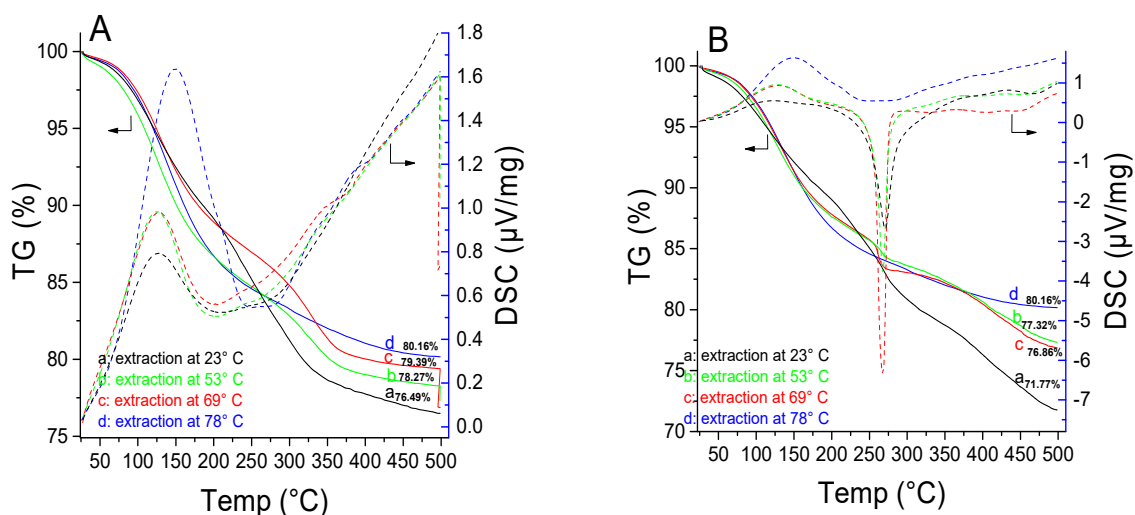


Figure 21. Simultaneous TG-DSC curves of the material molar ratio $\text{P123/Ti(O}^i\text{Pr)}_4$ (molar ratio: 0.0163) after two extraction at different temperatures, A(a-d): under N_2 and 19B(a-d): air atmosphere.

To investigate the influence of extraction temperature on mesoporous ordering, the calcined samples were characterized by SAXS (Figure 22A). SAXS pattern indicate an improvement of mesoporous ordering with increasing extraction temperature. Surfactant extraction temperature of 23 °C seems to be low because similar SAXS profile as without surfactant extraction was obtained. This pattern indicates the presence of a disordered structure after thermal treatment.

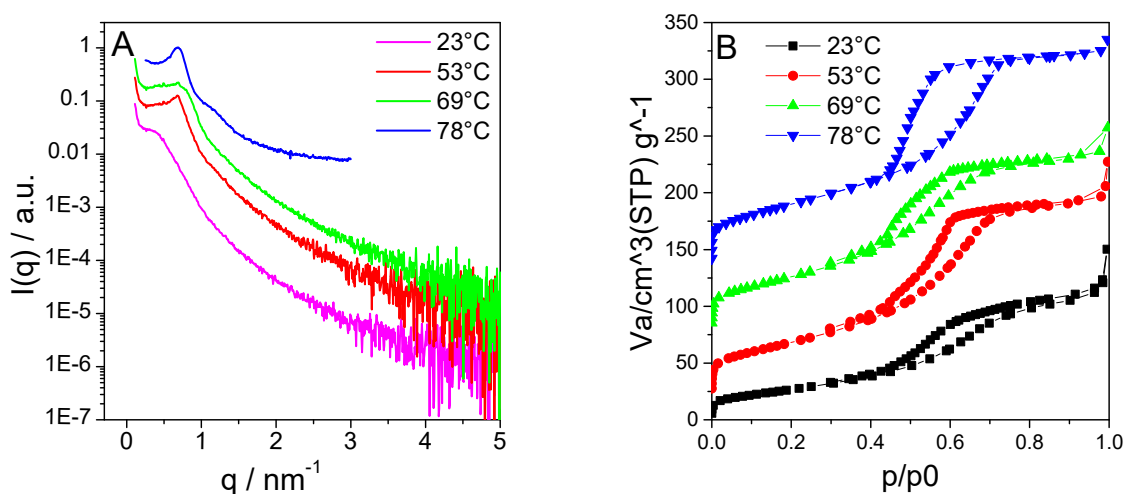


Figure 22. A) SAXS patterns and B) Nitrogen adsorption–desorption isotherms of the materials after calcination prepared with different extraction temperatures (synthesis conditions: molar $\text{P123}/(\text{TiO}^i\text{Pr)}_4 = 0.0163$, $T_{\text{evap}} = 40^\circ\text{C}$ (4 times), calcination: 25 – 450 °C with 1.2 °C/min in Ar than 2 h at 450 °C, 25 – 450 °C with 1.2 °C/min in O_2 than 2 h at 450 °C).

The nitrogen adsorption–desorption isotherms of these samples are shown in Figure 22B. The isotherms can be classified as type IV, typical for mesoporous materials according to the IUPAC nomenclature [141]. The calculated BET surface areas and pore diameter are

listed in Table 3. As can be seen in Table 3, BET surface area increases with rising extraction temperature. The sample at 78 °C extraction temperature exhibit the highest surface area (202 m²/g) compared to 97 m²/g measured for the sample where the surfactant was extracted at 23 °C. The crystallite size of the samples ranged from 3.86 to 7.41 nm. In general, crystallite size with surfactant extraction between 53 and 78 °C was comparable and increased considerably when the surfactant was extracted at 23 °C. The higher amount of surfactant maintaining in the titania after extraction at 23 °C might be the reason for the observed differences in BET surface and the loss of mesoporous ordering as already observed previously for TiO₂-W sample.

Table 3. Summary of the structure characteristics for materials synthesized with different solvent evaporation temperatures (molar P123/Ti(OⁱPr)₄ ratio = 0.0163, calcination at 450 °C).

temperature °C	crystal phase	crystallite size	BET m ² .g ⁻¹	d _{pore} nm	d _{cryst.} nm	band gap eV
23	anatase	7.41	97*	3.86	7.41	3.15
53	anatase, β-TiO ₂	3.99	172	4.90	3.99	3.16
69	anatase, β-TiO ₂	4.13	173	3.96	4.13	3.15
78	anatase, β-TiO ₂	3.86	202	3.86	3.86	3.08

*The big difference in the BET surface area for this sample and for the TiO₂-W sample might be due to instabilities occurred during the synthesis.

In order to investigate whether the mesoporous ordering will be influenced by the number of the extraction steps, a sample obtained after titania precipitation with ammonia was separated into two fractions. One fraction was extracted two times; the other fraction was extracted four times. SAXS pattern of both samples after extraction and after calcination are shown in Figure 23A. The patterns obtained after extractions were very similar and exhibited an intense first reflection and a weak second reflection which indicates formation of hexagonal ordered titania framework. After calcination the d₁₀₀ reflection disappeared in both samples and only a very broad peak could be detected. The presented results indicate that a) the mesoporous ordering was mainly destroyed during thermal treatment and b) that the number of the extraction steps will have only a minor influence on the mesoporous structure obtained after calcination. Small differences were obtained in BET surface area (two times: 196 m²/g, four times: 223 m²/g). These small differences could be caused either from instabilities of the synthesis process or from the different number of extraction steps. In general, the results are in good accordance with TGA results which showed only small differences in mass loss after two and four extractions.

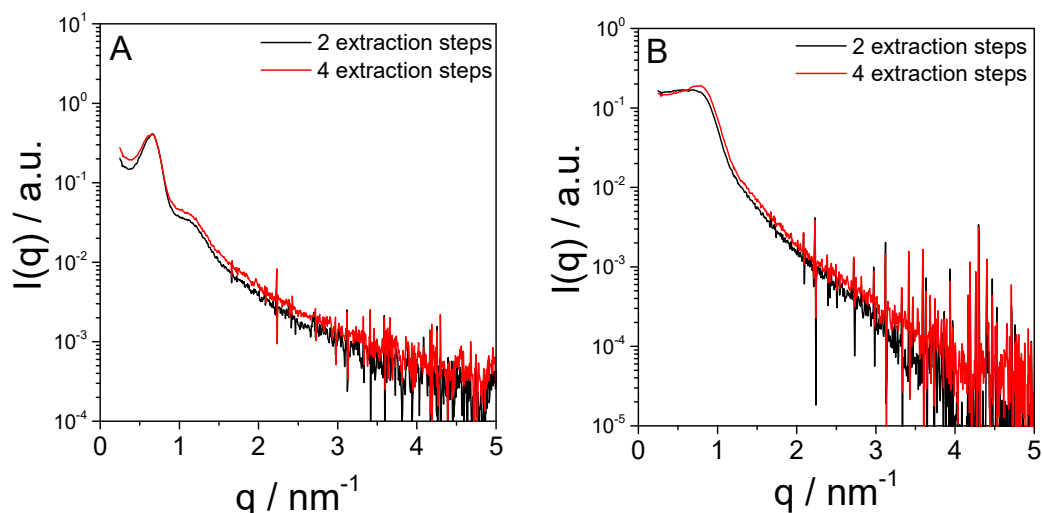


Figure 23. Influence of the number of extraction steps on the SAXS patterns **A)** after surfactant removal **B)** after calcination. (molar P123/(TiOⁱPr)₄ = 0.0163, T_{evap} = 40 °C, T_{extrac} = 78 °C, calcination: 25 – 450 °C with 1.2 °C/min in Ar than 2 h at 450 °C, 25 – 450 °C with 1.2 °C/min in O₂ than 2 h at 450 °C).

The obtained results indicate that the surfactant extraction step was necessary in order to obtain a titania framework which conserve the hexagonal ordered structure during calcination. However, two extraction steps seem to be sufficient for removing the surfactant. Extraction temperature should be as high as possible to remove the surfactant as far as possible in order to avoid a collapse of the ordered mesostructure during the following thermal treatment.

3.1.1.3 Molar surfactant/titanium ratio

Previous studies showed that surfactant/Ti-isopropoxide molar ratio is a key parameter to obtain a mesopore ordering of the amorphous titania framework present before calcination [90]. In this work, the P123 concentration is preserved constant at 32.5 Wt.% with the molar P123/Ti(OⁱPr)₄ ratio has been varied from 0.0105 to 0.04. The effect of the mol ratio of P123/Ti(OⁱPr)₄ on the overall properties of ordered mesoporous TiO₂ after thermal treatment was investigated. Figure A9 shows the XRD powder pattern of the TiO₂ materials with different molar ratios. All samples display the characteristic peaks of anatase (JCPDF card No. 01-073-1764) and minor reflexes of a β-TiO₂ phase (JCPDF card No. 00-035-0088). SAXS pattern of the materials after extraction and after calcination are presented in Figure 24. For molar P123/Ti(OⁱPr)₄ ratios between 0.0105 and 0.02, a hexagonal ordered titania framework was obtained after extraction. Materials prepared with molar P123/Ti(OⁱPr)₄ ratio of 0.025 and 0.04 display only a single broad reflection. After calcination ordered domains are still present in samples with the molar P123/Ti(OⁱPr)₄ ratio between 0.025 and 0.04. The results indicate the ordered mesoporous titania with semi-crystalline walls can be synthesized with molar P123/Ti ratios between 0.0105 and 0.02 when using Ti(OⁱPr)₄ as titania source.

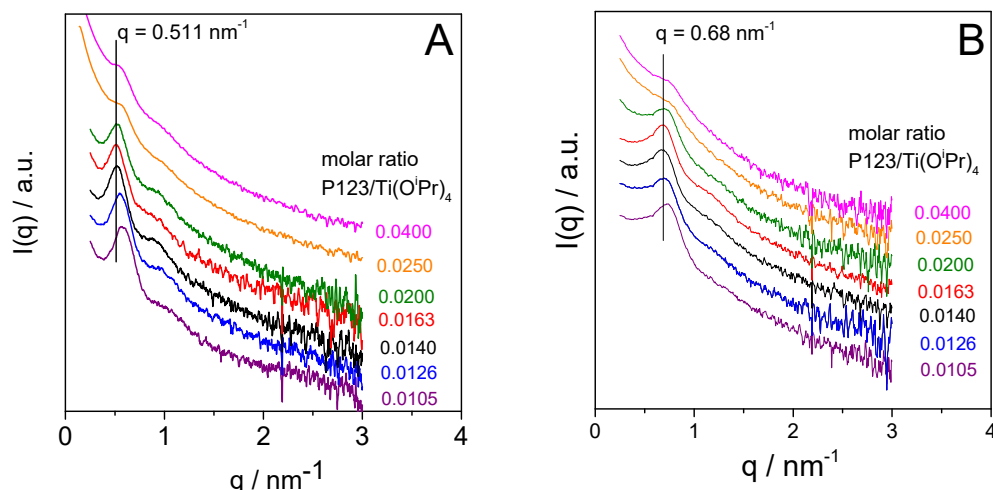


Figure 24. SAXS patterns of TiO_2 prepared with different molar $\text{P123/Ti(O}^i\text{Pr)}_4$ ratios (Tevap = 40 °C) A) after surfactant extraction (Texrac = 78 °C (4 times)), B) after calcination: calcination: 25 – 450 °C with 1.2 °C/min in Ar than 2 h at 450 °C, 25 – 450 °C with 1.2 °C/min in O_2 than 2 h at 450 °C).

Nitrogen adsorption–desorption isotherms (Figure A10) and the corresponding BJH pore size distributions (insert of Figure A10); obtained from an analysis of the adsorption branch of the isotherm, are presented in the Appendix. Samples obtained exhibit an isotherm of type IV, characteristic for mesoporous materials according to the IUPAC classification [153] with H2 type hysteresis. The isotherms with low molar $\text{P123/Ti(O}^i\text{Pr)}_4$ ratios exhibit sharp inflections in the P/P_0 range from 0.4 to 0.6 similar to their parent uncalcined samples. With additional increase in the molar $\text{P123/Ti(O}^i\text{Pr)}_4$ ratios above 0.0163 some changes can be seen from Figure A10 as the inflection of the isotherm and its sharpness is reduced and a shift toward higher P/P_0 range 0.5 to 0.9 compared to the uncalcined and lowers ratios. This indicates bigger pores are formed. Increasing the molar $\text{P123/Ti(O}^i\text{Pr)}_4$ ratio affects the structure and forms samples with more disordered structure. The BJH pore size distribution was calculated from the desorbed branch of the isotherm. At low molar $\text{P123/Ti(O}^i\text{Pr)}_4$ ratios for calcined samples the pore size distribution is more uniform and narrow compared with those obtained at high ratios above 0.0163. Table 4 presents the specific surface areas and the pore volumes for calcined samples. Differences in BET surface area of materials synthesized with a molar $\text{P123/Ti(O}^i\text{Pr)}_4$ ratio between 0.025 and 0.04 are relatively small and might be caused from the variation of the P123/Ti ratio or some instabilities in the synthesis process as reported before.

Table 4. Summary of the structure characteristics for materials synthesized with different molar P123/Ti(OⁱPr)₄ ratio after calcination .

molar ratio P123/Ti(O ⁱ Pr) ₄	BET (m ² /g)	V _p (cm ³ ·g ⁻¹)	d _p (nm)	crystallite size (nm)
0.0105	172	0.2139	3.86	5.2
0.0126	189	0.2941	3.86	4.1
0.0140	190	0.3136	3.86	3.9
0.0163	202	0.3585	3.86	3.8
0.0200	184	0.3238	3.86	3.1
0.0250	120	0.2371	3.86	3.5
0.0400	134	0.2338	3.86	3.1

3.1.1.4 *Changing of titanium source*

The effect of titanium source is an important factor affecting the textural and structural properties of TiO₂. It is directly related to its reactivity and, consequently, to the rates of the hydrolysis and condensation reactions [154]. Moreover, the effect of alkoxy group size in titanium precursor plays an important role in the hydrolysis reaction. The reaction rate of hydrolysis decreases with increasing size of alkoxy groups [155].

To study the influence of the titanium source on the formation of ordered mesoporous structure, titanium butoxide Ti(OⁿBu)₄ was used instead of Ti(OⁱPr)₄. The synthesis was carried out under the same conditions as used for preparation of the titania with Ti(OⁱPr)₄ as titania source. Additionally, one sample was synthesized by combination of both titanium sources with molar P123/Ti ratio of 0.0163. Figure 25 shows SAXS patterns of samples prepared using Ti(OⁿBu)₄ instead of Ti(OⁱPr)₄ after surfactant extraction and after calcination. Here, clear differences in shape of the SAXS patterns are visible between the single samples. When using a molar P123/Ti ratio of 0.014 and 0.0163 the degree of order was already relatively low after surfactant extraction. Only when using a molar P123/Ti ratio of 0.0194 a ordered structure was obtained as indicated by presence of two reflections in the scattering profile. Higher ordered material was obtained when using a combination of Ti(OⁿBu)₄ and Ti(OⁱPr)₄ as Ti source. After thermal treatment the materials which showed already low degree of order after extraction showed only a broad peak in the SAXS patterns which indicate the presence of a disordered structure after calcination. Also the order for the material synthesized with a molar P123/Ti(OⁿBu)₄ ratio of 0.0194 was relatively low after thermal treatment. Only the material synthesized with both titania sources can preserve the ordered structure during the thermal treatment.

Comparing the SAXS patterns of the samples after surfactant extraction using $\text{Ti}(\text{O}^n\text{Bu})_4$ (Figure 25A) with those prepared from $\text{Ti}(\text{O}^i\text{Pr})_4$ (Figure 24A) showed that all the reflections were shifted to higher q values when using $\text{Ti}(\text{O}^n\text{Bu})_4$ as Ti source. Moreover, a loss in the mesoporous ordering of TiO_2 framework was found with increasing amount of $\text{Ti}(\text{O}^n\text{Bu})_4$. The differences in ordering of mesoporous titania might be caused by the differences in size and structure of Ti alkoxide sources. $\text{Ti}(\text{O}^n\text{Bu})_4$ has a larger size and is less reactive towards water than $\text{Ti}(\text{O}^i\text{Pr})_4$ [156]. Due to the linearity and larger dimensions of $\text{Ti}(\text{O}^n\text{Bu})_4$, the reaction rates of hydrolysis might be reduced and co-condensation of the titania sub-units might be suppressed leading to the formation of smaller titania subunits (discrete oxo-oligomers or clusters) which affects the arrangement of these subunits around the micelles formed during solvent evaporation. This assumption was derived from the higher q values of the d_{100} reflection of the samples obtained after extraction when the materials were synthesized with $\text{Ti}(\text{O}^n\text{Bu})_4$. Moreover, the reduced d_{100} spacing (higher q values) indicates the formation of more densely packed titania subunits in these samples compared to the materials synthesized with $\text{Ti}(\text{O}^i\text{Pr})_4$.

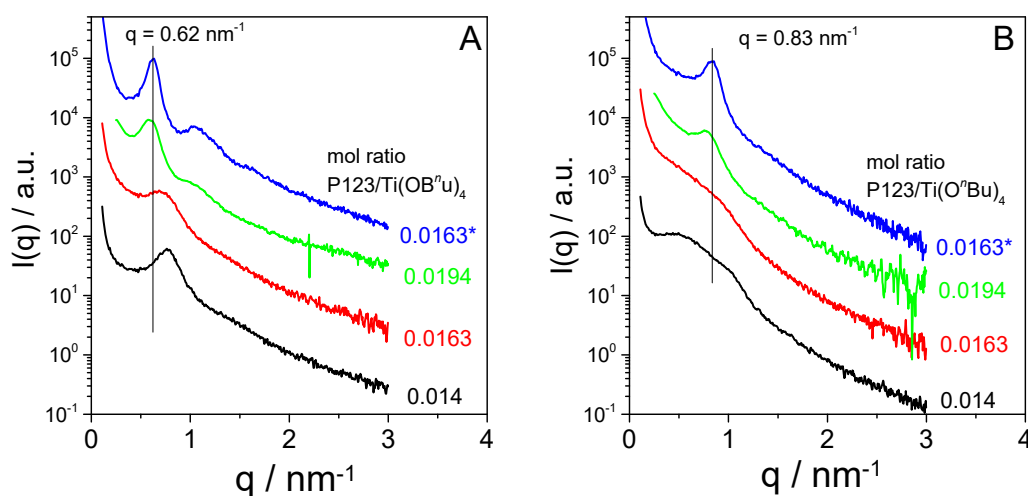


Figure 25. SAXS patterns for the materials prepared with different mol ratio P123/ $\text{Ti}(\text{O}^n\text{Bu})_4$ after surfactant extraction A), and after thermal treatment B); synthesis conditions: Texrac = 78 °C (2 times), calcination: 25 – 450 °C with 1.2 °C/min in Ar than 2 h at 450 °C, 25 – 450 °C with 1.2 °C/min in O_2 than 2 h at 450 °C).

The effect of titanium precursor can be seen also on BET surface areas of the calcined samples. The BET surface area for the materials prepared using $\text{Ti}(\text{O}^n\text{Bu})_4$ (Table 5) were lower than that area obtained using $\text{Ti}(\text{O}^i\text{Pr})_4$ (Table 5) when the same molar surfactant/Ti ratio was used. The mean pore size decreases slightly with increasing Ti amount when using $\text{Ti}(\text{O}^n\text{Bu})_4$ but was still in the same range as obtained when using $\text{Ti}(\text{O}^i\text{Pr})_4$. Mean crystallite

size after calcination was, in general, also in the same range. The reason for the lower degree of ordering for materials prepared with $\text{Ti}(\text{O}^n\text{Bu})_4$ might be the higher density of the titania framework formed during solvent evaporation which lead to thinner wall thickness at the same pore dimension compared to the material synthesized with $\text{Ti}(\text{O}^i\text{Pr})_4$. The thinner wall thickness in samples prepared with $\text{Ti}(\text{O}^n\text{Bu})_4$ was derived from the lower d_{100} spacing after extraction and the similar mean pore size after calcination (obtained from nitrogen sorption analysis) independent which Ti source was used. Furthermore, it was assumed that mean pore size determined after calcination was in the same range as after extraction. This assumption is supported by a result given in Table 5 where the same mean pore size was found before and after calcination. During calcination of the materials synthesized with $\text{Ti}(\text{O}^n\text{Bu})_4$ the formed crystallites destroy the ordered framework probably because of lower wall thickness in these samples compared with the wall thickness obtained when using $\text{Ti}(\text{O}^i\text{Pr})_4$. The lower wall thickness results from processes during solvent evaporation. It is assumed that titania species with higher density are formed when $\text{Ti}(\text{O}^n\text{Bu})_4$ instead of $\text{Ti}(\text{O}^i\text{Pr})_4$ is used, resulting in lower wall thickness of the amorphous ordered titania framework.

Otherwise, phase composition of the calcined material does not depend on Ti source. Independent whether $\text{Ti}(\text{O}^i\text{Pr})_4$ or $\text{Ti}(\text{O}^n\text{Bu})_4$ was used all samples show a mixture of anatase (main phase) and $\beta\text{-TiO}_2$.

Table 5. Structural characteristics of titania prepared with $\text{Ti}(\text{O}^n\text{Bu})_4$

molar ratio $\text{P123/Ti-(O}^n\text{Bu)}_4$	crystal phase	crystallite size nm	BET $\text{m}^2\cdot\text{g}^{-1}$	dp nm
0.0140	anatase, $\beta\text{-TiO}_2$	5.2	178	3.1
0.0163	anatase, $\beta\text{-TiO}_2$	4.4	156	3.6
0.0194	anatase, $\beta\text{-TiO}_2$	4.8	140	4.2
0.0163*	anatase, $\beta\text{-TiO}_2$	4.5	180	4.0

* This sample was synthesized by combination of both titanium sources.

3.1.2 Photocatalytic activity of the prepared materials

In order to investigate the photocatalytic activity of the synthesized mesoporous TiO_2 , the calcined samples were tested in phenol degradation applying different light sources and wavelengths.

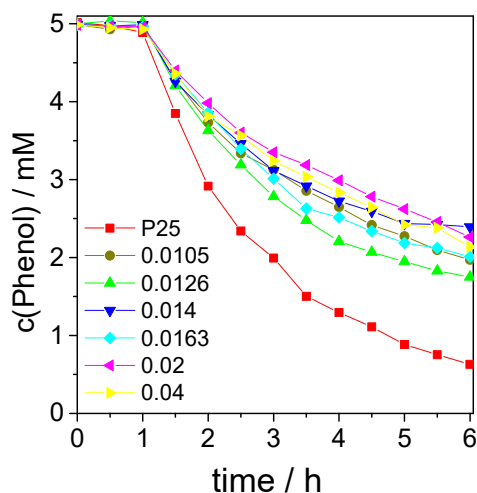


Figure 26. Influence of reaction time on phenol concentration for titania samples synthesized with different molar ratio of $\text{P123}/\text{Ti}(\text{O}^i\text{Pr})_4$ under UV irradiation (Hg lamp, synthesis conditions: molar $\text{P123}/\text{Ti}(\text{O}^i\text{Pr})_4$ = variable, $T_{\text{evap}} = 40^\circ\text{C}$, $T_{\text{extrac}} = 78^\circ\text{C}$ (4 times), calcination: $25 - 450^\circ\text{C}$ with $1.2^\circ\text{C}/\text{min}$ in Ar than 2 h at 450°C , $25 - 450^\circ\text{C}$ with $1.2^\circ\text{C}/\text{min}$ in O_2 than 2 h at 450°C).

Figure 26 compares the photocatalytic activity of mesoporous titania synthesized with different molar $\text{P123}/\text{Ti}(\text{O}^i\text{Pr})_4$ ratios sample (range: 0.0105 – 0.04) under UV irradiation. Adsorption of phenol on tiania surface was very low. The samples differ structural mainly in degree of ordering and BET surface area. As shown, all samples exhibit photocatalytic efficiency to degrade the phenol but it was less than that of P25 (Evonik) which is considered as a reference material. The influence of the structural parameters on photocatalytic activity in phenol degradation is relatively small and correlations between BET surface (Table 4) or degree of ordering (Figure 24) on activity could not be found. Photocatalytic phenol degradation using UV irradiation can be described by a pseudo first order reaction with rate constants between 0.16 and 0.27 min^{-1} .

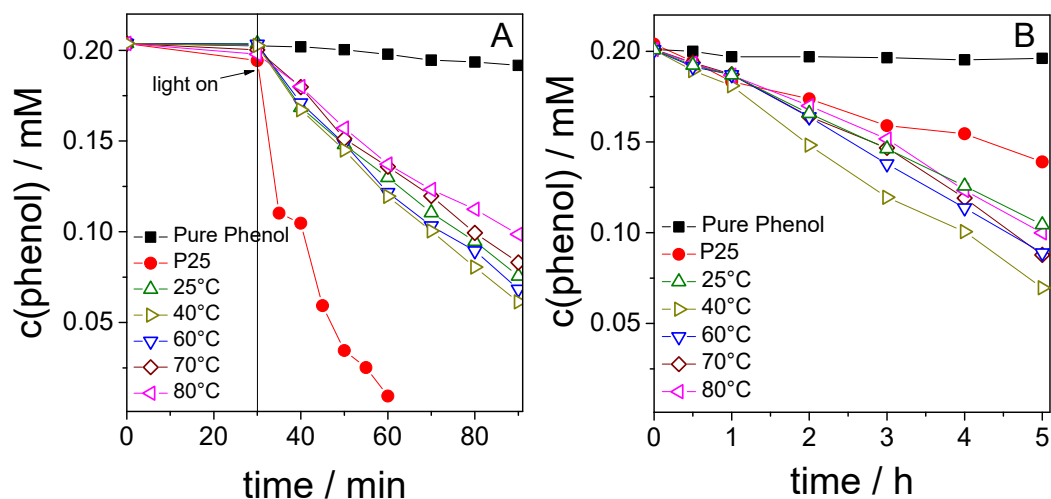


Figure 27. Influence of reaction time on phenol concentration for titania samples synthesized with different solvent evaporation temperature at irradiation with white light A) and visible light, $\lambda > 420$ nm B) (Xenon lamp, synthesis conditions: molar $\text{P123}/(\text{TiO}^{\text{I}}\text{Pr})_4$ = variable, T_{evap} variable, $T_{\text{extrac}} = 78$ °C (4 times), calcination: 25 – 450 °C with 1.2 °C/min in Ar than 2 h at 450 °C, 25 – 450 °C with 1.2 °C/min in O_2 than 2 h at 450 °C)).

Samples prepared with different solvent evaporation temperature were tested also in phenol degrading using a Xenon lamp as irradiation source. Results are presented in Figure 27. Adsorption of phenol on the titania surface during the dark period was again lower than 5% despite the high BET surface of the synthesized titania materials. Phenol bulk concentration in the presence of the titania and light decreases with reaction time. Decreasing of phenol concentration in presence of mesoporous titania photo-catalyst was much higher than in absence of the catalyst. Photocatalytic phenol degradation using white light (Figure 27A) can be again described by a pseudo first order reaction with rate constants between 0.012 and 0.019 min^{-1} . Here, phenol degradation increases slightly with increasing BET surface and mesoporous ordering but differences between the samples were relatively low. Phenol degradation with the synthesized mesoporous titania was clearly slower than degradation over P25 which had a rate constant of 0.091 min^{-1} . The same behavior was previously observed for methyl orange degradation and explained by the higher volume of the charge carrier recombination in the mesoporous titania [110]. The situation changed when the samples were irradiated with visible light containing wavelengths > 420 nm (Figure 27B). Here, the photocatalytic activity of the mesoporous titania was superior to that of P25. Under these conditions, phenol degradation followed a zero order reaction and the degradation rate was between 0.019 and 0.025 mmol/h. The highest activity was found for a sample with high mesoporous ordering and BET surface, but under visible light illumination, no significant influence of the BET surface, the mesoporous ordering or crystallite size on the photocatalytic

activity could be observed. The generally higher visible light photocatalytic activity of mesoporous titania compared to P25 is attributed to the presence of nitrogen and carbon species near the titania surface [136, 157]. Both elements are present in the synthesized titania even after calcination as proven by XPS (Figure 16).

Finally, samples prepared at different surfactant extraction temperature (Figure 28A) or synthesized with $\text{Ti}(\text{O}^n\text{Bu})_4$ instead of $\text{Ti}(\text{O}^i\text{Pr})_4$ (Figure 28B) were also tested also in phenol degradation using visible light. The photocatalytic activity of these samples was again superior to that of P25 but differences in activity between these samples were only small although the materials differ both in degree of ordering and BET surface area. Therefore, it might be assumed that the amount of nitrogen or carbon residuals of the materials after calcination was similar and approximately independent of the particular synthesis parameters. The nitrogen will be introduced during the titania precipitation step by ammonia and not completely removed during surfactant extraction. The carbon might originate from the surfactant or from not completely hydrolyzed alkoxide groups of the Ti source. The lower activity of sample were the surfactant was extracted at 23 °C and for the sample with the highest amount of $\text{Ti}(\text{O}^n\text{Bu})_4$ might be caused by the presence of higher amounts of carbon residuals in these samples.

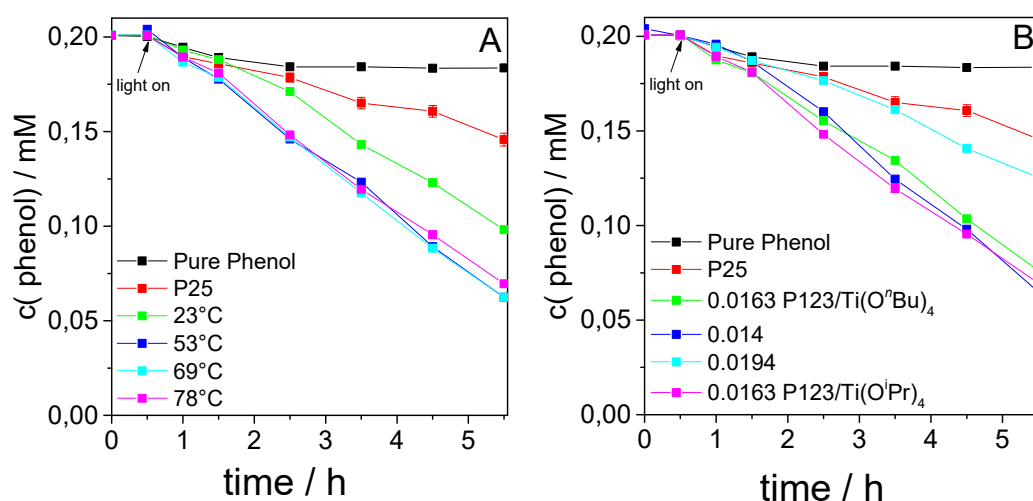


Figure 28. Influence of reaction time on phenol concentration for titania samples synthesized with different surfactant extraction temperatures (4 times) - A) and with $\text{Ti}(\text{O}^n\text{Bu})_4$ as Ti source - B); (Xenon lamp, visible light $\lambda > 420$ nm, A synthesis conditions: molar P123/Ti ratio = variable, $T_{\text{evap}} = 40$ °C, B): Textrac = 78 °C (2 times), calcination: 25 – 450 °C with 1.2 °C/min in Ar than 2 h at 450 °C, 25 – 450 °C with 1.2 °C/min in O_2 than 2 h at 450 °C).

3.2 Doped ordered mesoporous titanium dioxide

3.2.1 Metal-doped ordered mesoporous titanium dioxide

Fe, Co and Ni were used to synthesize doped mesoporous TiO₂ with different metals content (0.5 and 5 mol %) via the same method which used to synthesize pristine TiO₂ in order to study the effect of doping of a second metal on the structural characteristics and photocatalytic activity of ordered mesoporous titania.

3.2.2 Structural characteristics

SAXS was applied for monitoring changes in mesoporous structure between step c and d. SAXS patterns of pristine TiO₂ and titania doped with 0.5 or 5 mol% metal after treatment the mesophase with ammonia can be seen in Figure 29A-B (synthesis step c). Independent of the used metal salt, all patterns of the materials synthesized by adding 0.5 mol% of doping metal exhibited an intense first reflection (d_{100}) and a weaker second reflection which indicates presence of a ordered mesoporous structure after titania precipitation. Similar results were obtained after addition of 5 mol% Co or Ni. The d_{100} spacing peaked around 13.4 nm ($q = 0.46 - 0.47 \text{ nm}^{-1}$). The nearly identical d_{100} spacing indicates that the size of the hexagonal framework was not strong affected by the presence of the dopant. Only when 5 mol% Fe was added into the Ti precursor containing synthesis solution no ordering was observed after ammonia treatment indicated by absence of the (100) reflection. Extraction of the surfactant in boiling ethanol (step d) led only to a slight shrinking of the hexagonal structure. This seems to be approximately independent of the particular metal incorporated, but slightly influenced by its amount (Figure 29C-D). The d_{100} spacing peaked at around 12.6 nm ($q = 0.50 \text{ nm}^{-1}$) for the samples doped with 0.5 mol% and at 12.1 nm ($q = 0.52 \text{ nm}^{-1}$) for samples prepared with 5 mol% dopant. After the final thermal treatment at 450 °C (step e) the d_{100} reflection was shift to about 9.2 nm (0.5 mol% metal, $q = 0.68 \text{ nm}^{-1}$) and 9.7 nm (5 mol% metal, $q = 0.65 \text{ nm}^{-1}$). The shrinking of the mesoporous structured is attributed to titania densification caused by thermal induced crystallization and sintering processes. The shift in 100 reflections was connected with a broadening of the diffraction peaks and the low intense reflection could not be clearly resolved in these SAXS patterns. The broadening indicates a partial loss of the hexagonal ordering during thermal treatment. The loss is higher for the materials doped with 5 mol% metal in comparison to those doped with 0.5 mol%. Moreover, for the material doped with 5 mol% Co, the 100 reflection in SAXS pattern disappeared after thermal treatment which suggests that the mesoporous ordering in this sample collapsed during the thermal treatment.

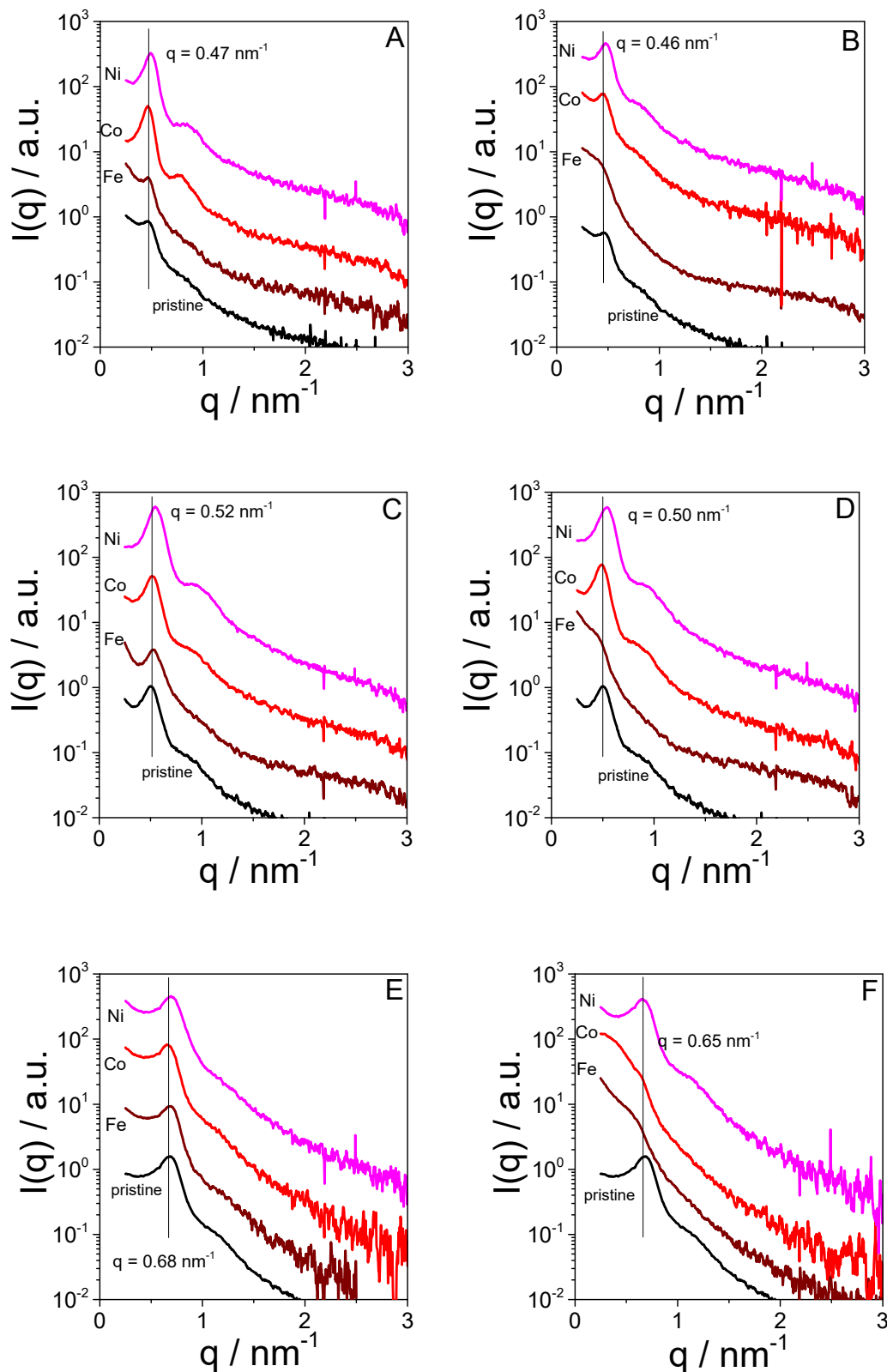


Figure 29. SAXS patterns pristine and doped titania prepared with 0.5 (A, C, and E) and 5 mol% metal (B, D and F) after different synthesis steps: (A, B) after treatment with NH_3 gas - step c, (C, D) after treatment in boiling ethanol - step d, and (E, F) after thermal treatment at 450°C - step e; the single SAXS pattern was vertical shifted by multiplication with a constant factor.

Scanning transmission electron microscopy (STEM) was applied in order to obtain further insight in the morphology of materials formed after thermal treatment (step e). STEM HAADF images of the samples synthesized with 0.5 mol% Fe, Co, and Ni are presented in Figure 30. All three images show a hexagonal ordered titania framework in accordance with the presented SAXS patterns. Differences in hexagonal ordering between the samples doped with the particular metal were relatively low. The walls of the titania framework are composed of small crystalline grains, which are orientated in all directions without any order (See Appendix Figure A11). EDX analysis confirms the presence of the particular doping element (Figure A12-Figure A14).

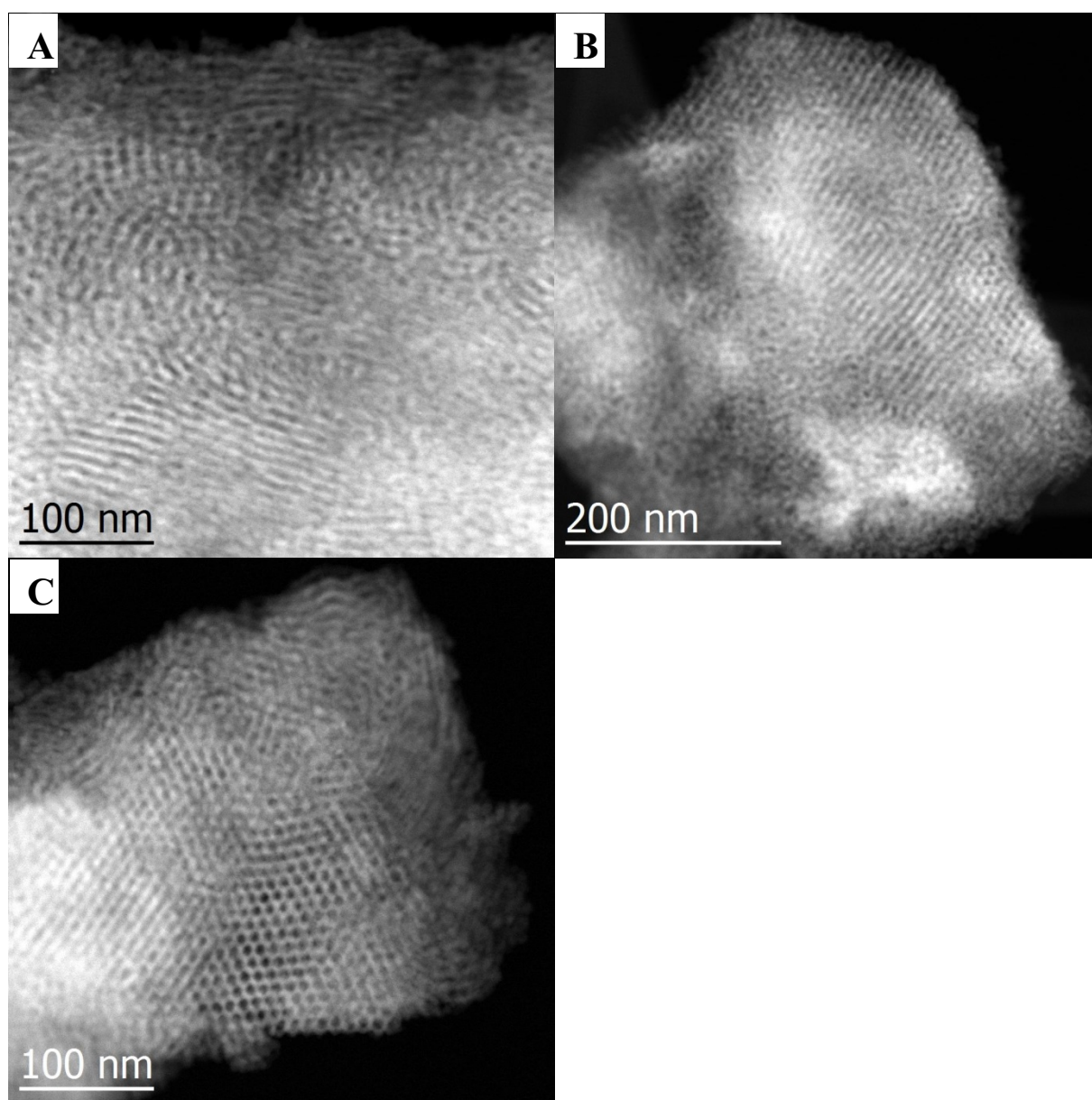


Figure 30. STEM-HAADF images of titania doped with 0.5 mol% metal after thermal treatment, A) Fe, B) Co, C) Ni.

Moreover, results of EDX analysis suggests that the doping metal might be homogenous distributed over the particle either being attached to or integrated into TiO_2 crystallites.

Selected STEM HAADF images of calcined materials synthesized with 5 mol% doping metal are presented in Figure 31 for samples containing Fe and Ni. The image of the Fe doped sample (Figure 31A) exhibits a mesoporous framework with low ordering. Here, the size of the mesopores within of a single particle differs considerably from each other. This observation explains the absence of the d_{100} reflection in the SAXS pattern. In contrast, identical amounts of Ni did not lead to a loss in mesoporous ordering in the calcined material (Figure 31B). Here, the same hexagonal framework was obtained as in the doped sample with 0.5 mol% Ni. EDX analysis of the Fe and Ni containing samples again confirms the presence of the particular metal (Figure A15-Figure A18) and its relative homogenous distribution. For the doped sample with 5 mol% Ni, nanoparticle of about 20 nm containing Ni or NiO coexists together with smaller nanoparticles (about 2 nm) on the titania surface (Figure A18).

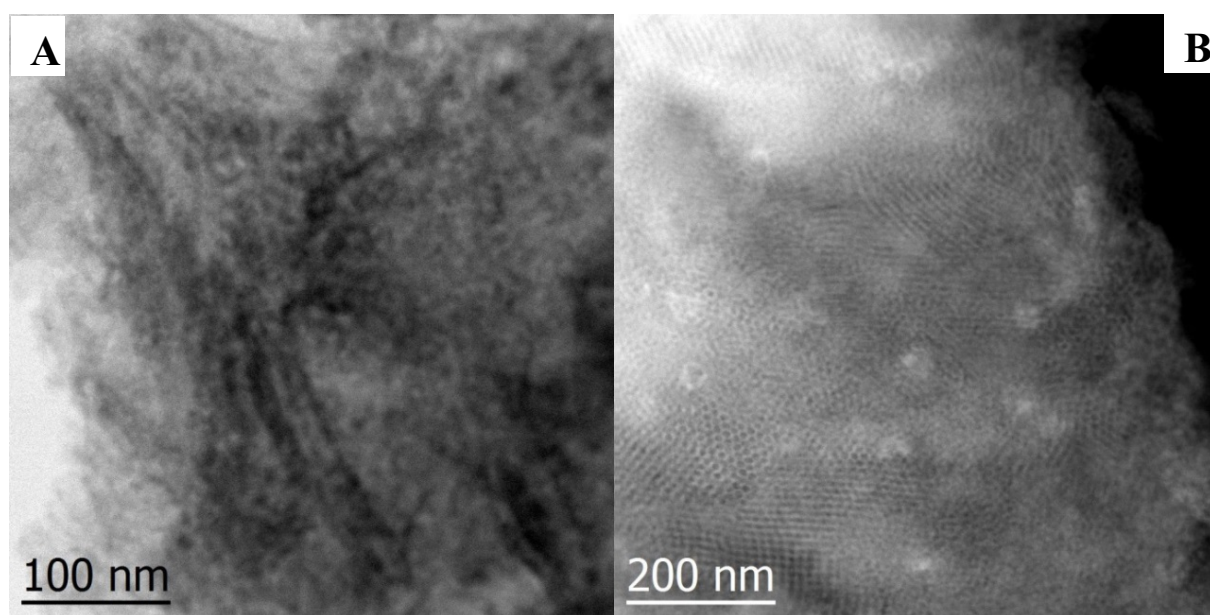


Figure 31. STEM-HAADF images of titania samples doped with 5 mol% metal after thermal treatment, A) Fe, B) Ni.

XRD patterns of calcined materials synthesized with 0.5 and 5 mol% doping metal are shown in Figure 32A-B. Independent of the particular metal and its concentration the samples show intense reflexes of anatase (ICDD 03-065-5714) together with low intense reflexes of β - TiO_2 (ICDD 00-035-0088). The same phase composition was also obtained at absence of any dopant. For the doped sample with 5 mol% Co, the β - TiO_2 phase was not detected. Reflexes from phases separate phases containing the doping metal or a shift of the 101 titania reflexes were not observed in presence of the doping metal (Figure A19). The average crystallite size

of the primary particles estimated using the Scherrer equation is listed in Table 6. For the doped samples with 0.5 mol% metal, the mean crystallite diameter was about 4 nm and differences were in general lower than 0.5 nm (range: 3.9 - 4.3 nm). For the doped samples with 5 mol% metal, larger differences in crystallite size were obtained. While for the Ni doped samples, the mean crystallite diameter was nearly identical to the diameter obtained with 0.5 mol% metal, larger crystallite diameters were estimated for Fe (5.9 nm) and Co (6.7 nm).

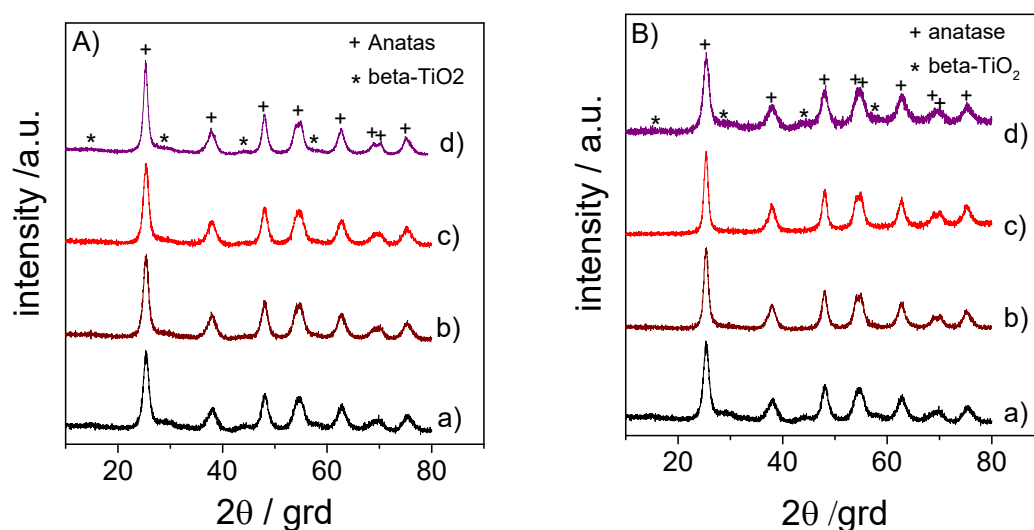


Figure 32. XRD patterns of calcined mesoporous titania prepared with A) 0.5 and B) 5 mol% doping metal; a)-pristine, b) Fe, c) Co and d) Ni.

N₂ adsorption–desorption isotherms of calcined samples doped with 0.5 or 5 mol% metal are presented in Figure A20A-B. All samples exhibited an isotherm of type IV pattern, which is characteristic for mesoporous materials [141]. Samples doped with 0.5 mol% metal showed a H2 hysteresis loop, which indicates the occurrence of regular and narrow pores [158, 159]. A H2 hysteresis loop was also observed for materials doped with 5 mol% Co and Ni. However, for the doped material with 5 mol% Fe, the hysteresis loop changed to H3 type indicated by a reduced sharpness of the inflection and shifting of the pressure range toward higher values (0.45 - 1.0 P/P₀). H3 hysteresis loop indicates the occurrence of irregular long and narrow pores [141].

BET surfaces, pore volumes (V_p) and maximum of the pore diameter distribution (d_p) are summarized in Table 6. The respective BET surface areas of pristine TiO₂ and those of samples doped with 0.5 mol% Fe or Ni was similar (180-200 m²/g). On the contrary, for the doped titania with low amounts of Co the BET surface area decreased to about 173 m²/g.

Observed differences in the BET surfaces and pore volumes of the doped titania samples with 0.5 mol% metal might be caused from instabilities in the synthesis process and/or the presence of the doping metal. Doping with 5 mol% Fe or Co led to a clear decrease in BET surface (115 m²/g). In contrast, for the doped material with 5 mol% Ni, the BET surface was in the same range than that of the sample doped with 0.5 %. Figure 33 exhibits the pore diameter distribution estimated from the adsorption branch. For doping with 0.5 mol% metal the samples showed a nearly identical pore size distribution independent of the particular metal, with a maximum located at about 4 nm. When the titania was doped with 5 mol% metal, obvious differences in pore size distribution between samples containing the particular doping metal were visible.

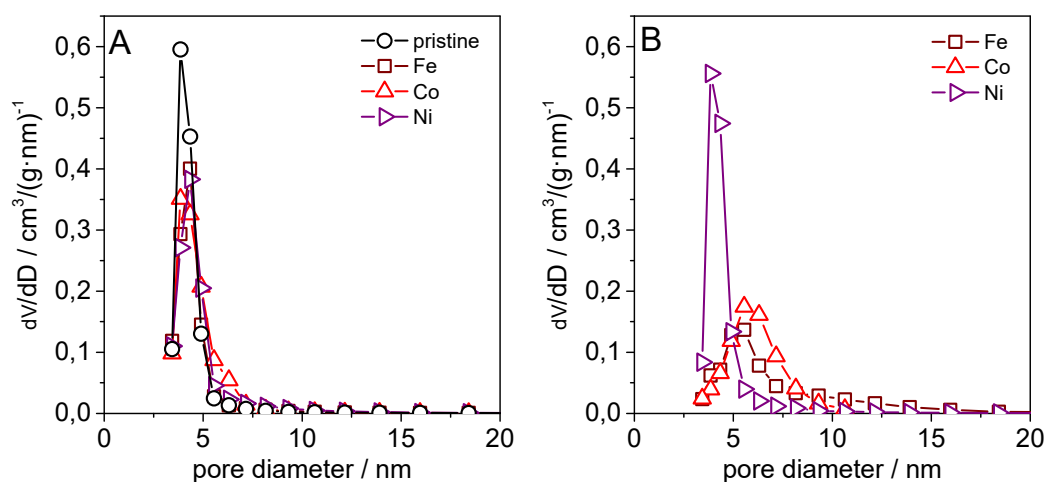


Figure 33. Pore size distribution of doped mesoporous titania calcined at 450 °C, A) 0.5 mol% metal, and B) 5 mol% metal.

Table 6. Characteristics of calcined TiO₂ doped with 0.5 or 5 mol% metal.

sample	crystal phase	metal content mol%	BET m ² /g	V _p cm ³ /g	d _p nm	cryst. size nm	band gap eV
Pristine TiO ₂	anatase, β-TiO ₂	-	202	0.36	3.9	3.9	3.16
Fe/TiO ₂	anatase, β-TiO ₂	0.5	182	0.30	4.3	4.7	3.06
		5	116	0.30	5.6	5.9	2.60
Co/TiO ₂	anatase, β-TiO ₂	0.5	173	0.34	3.9	4.7	2.98
		5	115	0.32	5.6	6.7	2.78
Ni/TiO ₂	anatase, β-TiO ₂	0.5	199	0.32	4.3	3.9	3.10
		5	212	0.36	3.9	3.4	2.84

In order to study the oxidation state and local environment of doping metal, the titania doped with Fe obtained after thermal treatment have been characterized by EPR spectra as shown in Figure 34. The sample doped with 0.5 mol% Fe showed an unsymmetrical signal at $g = 4.3$ and a symmetrical peak at $g = 1.99$ with $\Delta H_{pp} = 67$ G Figure 34. The signal located at $g = 1.99$ shows the presence of isolated high spin Fe^{3+} cations in octahedral symmetry [160]. Moreover, the signal indicates an uniform distribution of the Fe^{3+} ions inside the titania framework by substitution of Ti^{4+} sites [161, 162]. Radii of Ti^{4+} and Fe^{3+} are very similar. The signal at 4.3 is attributed to isolated Fe^{3+} ions in orthorhombic state located either inside the anatase phase adjacent to a charge compensating oxide anion vacancy [161, 163] or on the titania surface [162, 164]. Because the relative intensity of the surface Fe^{3+} signal ($g = 4.3$) was much lower than that of the Fe^{3+} in the bulk phase ($g = 1.99$) it can be assumed that most of the Fe^{3+} ions being integrated in the crystal lattice. The iron content was below the solubility limit of iron (around 1 wt.%) in the anatase phase [165]. This assumption is further supported by XPS analysis of this sample where no iron signal was detected (Figure A21). Additional to the already observed signals, the EPR spectra of the sample loaded with 5 mol% Fe showed a new broad peak superimposed on the signal at $g = 1.99$. This new signal was attributed to spin-spin interactions among neighboring Fe^{3+} ions and indicates the presence of Fe^{3+} in an iron oxide cluster [160, 164].

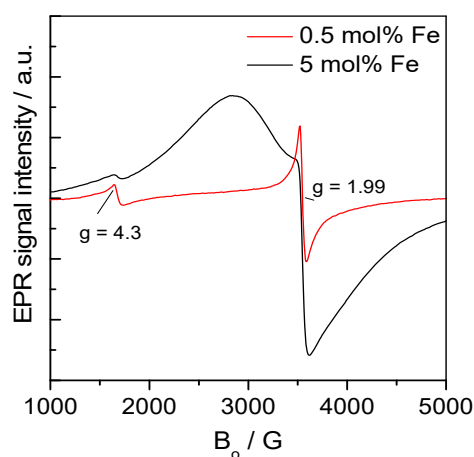


Figure 34. EPR spectra of the calcined mesoporous titania doped with iron (the spectra were recorded at 295 K).

Diffuse reflectance spectra are presented in Figure 35A-B. The pristine TiO_2 shows only absorbance in the wavelength region < 400 nm [166, 167]. This absorbance was attributed to the intrinsic band gap absorption of anatase due to the ligand-metal charge transfer between titanium Ti^{4+} (3d) and oxygen ligand O^{2-} (2p) [168]. The doped samples showed enhanced absorption at wavelengths higher than 400 nm. The extent of the red shift depends on the

particular metal and its concentration. It was general higher for samples synthesized with 5 mol% of dopants. The 0.5 mol% Fe containing sample showed light absorption between 400 and 500 nm. An absorption band around 415 nm was attributed to electronic transition from Fe^{3+} energy level to the conduction band of titania [169]. The Fe^{3+} energy level was obtained by substitution of Ti^{4+} ions by Fe^{3+} ions. This finding is in good accordance with EPR results. When the amount of Fe was increased to 5 mol%, the absorption wave length increased up to 650 nm with a shoulder at about 500 nm. This new band could result from d-d transition of Fe^{3+} species [60] and indicates the presence of iron containing clusters in the sample. A band at 530 nm was previously attributed to the presence of $\alpha\text{-Fe}_2\text{O}_3$ [162]. The doped sample with 0.5 mol% Co exhibited light absorption between 370 and 800 nm. Such red shift was attributed to sp-d exchange interactions between the band electrons and the localized d-electrons of the Co^{2+} ions substituting Ti^{4+} cations [170]. Judging by the ionic radius, the Co^{2+} ion can easily replace the Ti^{4+} ion. d-d-transitions of Co^{3+} in octahedral coordination were observed between 350 and 440 nm [171]. With the doping concentration of Co increasing to 5 mol%, the absorption intensity in the visible range further increased and a new band around 620 nm (Figure 35B) was detected which was attributed to Co^{2+} ions in tetrahedral coordination. The appearance of this band along with absorption bands between 350-440 nm and 450-550 nm hints at the presence of spinel Co_3O_4 phase in this sample [171]. Doping with 0.5 mol% Ni results only in a weak red shift of the light absorption compared to the other metals. Absorption between 400 and 450 nm indicates presence of Ni^{2+} ions in octahedral environment. The doped sample with 5 mol% Ni shows an additional band at wavelengths higher than 600 nm which may result from the presence of a NiO [171] observed by TEM.

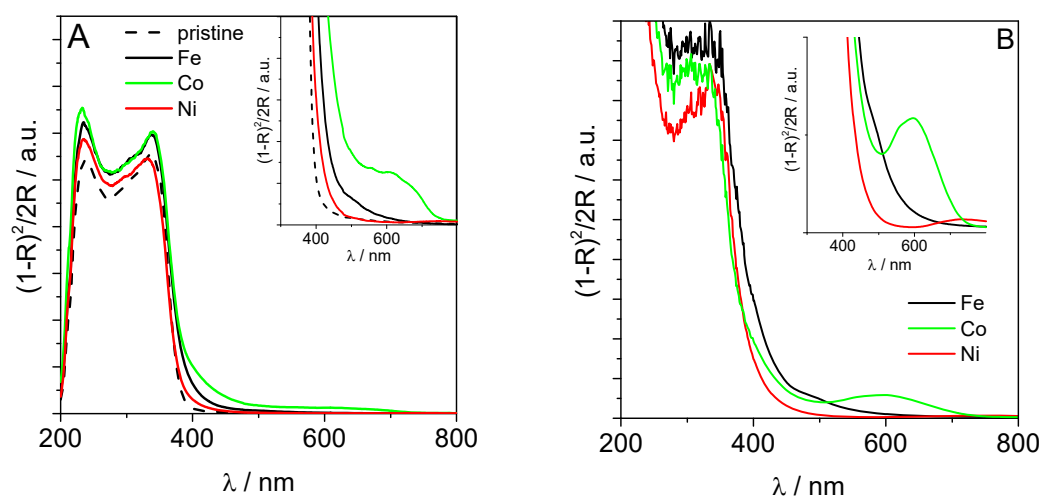


Figure 35. UV-Vis diffuse reflectance spectra (DSR) of calcined un-doped mesoporous TiO_2 and doped mesoporous TiO_2 prepared with a) 0.5 and b) 5 mol% metal.

The optical band gap (BG) energies were calculated from the Tauc's plot [143] and are listed in Table 6. The estimated band gap energies for doped TiO₂ were lower than that of undoped TiO₂ as natural consequence of the shift of the band gap energy toward the visible region in the presence of the dopant. For the doped samples with 0.5 mol%, the band gap shift was lower than 0.3 compared to the pristine sample. The shift might result from charge transfer transitions between d-electrons of the dopant ions which creates impurity electron levels in the band gap of the titania and the TiO₂ valance or conduction band [172]. On the other hand, for the doped samples with 5 mol% metal, the decrease in band gap energy was much higher compared to the doping level of 0.5 mol%. At this high dopant content, the observed strong decrease in band gap energy may be associated with the presence of X-ray amorphous oxidic phases containing the doping metal which are able to absorb light in the visible range [173].

3.2.3 Photocatalytic activity of metal doped mesoporous titanium dioxide

The photocatalytic activity of the mesoporous TiO₂ nanopowders was evaluated using phenol. Although the tested titania samples had a relatively high BET surface, phenol adsorption on the titania surface during the dark reaction was very low (Figure 36). For comparison, commercial titania P25 was also tested and plotted in same Figure 36. Phenol degradation starts immediately after switching on of the UV-light. The decrease in phenol concentration with time depends on the particular metal and its content. For the doped samples with 0.5 mol% Fe or Co about 80% of phenol was converted within 6 h (Figure 36A). This degradation was much higher as observed for the Ni doped and the pristine titania samples. Addition of 5 mol% of these metals resulted in a material with clearly lower photocatalytic activity. Here phenol degradation after 6 h dropped to 46, 51, and 38%, respectively and was lower than observed for pristine titania. First order rate constant of phenol degradation presented in Table 3 supports the above statements. These results differs from those obtained with Zn doping where photocatalytic activity was similar at Zn content below 10 wt.% [116].

The presented results indicate that material properties such as specific surface area, pore volume, crystallite size, and degree of order have a relatively small influence on the photocatalytic activity of the titania materials in phenol degradation at irradiation with UV light. Photocatalytic activity of the mesoporous titania was mainly determined by the presence of the particular metal and its concentration. Phenol photo-oxidation efficiency is regularly mediated by a hydroxyl-radical pathway [174]. In a first step electron-hole pairs are generated

in the titania bulk by light absorption with energy equal or greater than the titania bandgap. In further steps the generated charge carriers can recombine or migrate to the surface where they can react. Hydroxyl-radicals are assumed to be formed by reaction of positive charged holes with adsorbed OH^- and/or water molecules and electrons are removed by reaction with oxygen molecules [136, 175]. Depending on the particular doping element, its amount, local structure, and oxidation state, the donor might act as a recombination centers or as a trap for the particular charge carrier [113]. Since the irradiation energy applied was in the spectral range of titania band gap (UV irradiation), the rate of carrier generation might be comparable for samples doped with 0.5 mol% metal and the pristine titania. In this case, the observed differences in photocatalytic activity might be explained by interaction of the doping element itself (Fe, Co and Ni) or defects created in their environment with the charge carriers. These sites will act as a charge carrier trap and altering the electron/hole pair recombination rate [176]. Because the higher photo-activity of the samples doped with 0.5 mol% Fe, Co, Ni compared to pristine titania the incorporated metal ions might acting preferred as electron trap so that the holes can migrate to the surface and react with OH^- or adsorbed water molecules [59], which lead to higher photoactivity compared to pristine titania. It is known that Fe^{3+} ions in low concentration can act under UV irradiation both as electron and hole trap and therefore can reduce the photo-generated hole-electron recombination rate [161]. EPR and UV/Vis of the calcined titania doped with 0.5 mol% Fe indicate the presence of isolated Fe^{3+} ions both inside of the titania framework and on its surface. The increase in phenol degradation rate at 0.5 mol% iron doping in comparison to the pristine titania is attributed to the presence of these isolated Fe^{3+} ions. An increase in activity in phenol degradation after iron doping (1 wt%) was already observed using nano sized-iron doped anatase [165]. On the other hand, at higher content of the doping metal, surface modifications due to formation of Fe, Co and Ni amorphous oxides phases on the titania surface appeared as proven by EPR and UV/Vis spectroscopy. These new oxides structures might reduce the rate and number of generated charge carrier, the number of phenol adsorption sites on titania and/or act as recombination centers which reduce the life time of the charge carrier compared to pristine titania [161]. Therefore, the photocatalytic activity of samples with 5 mol% doping metal is lower than that of pristine titania.

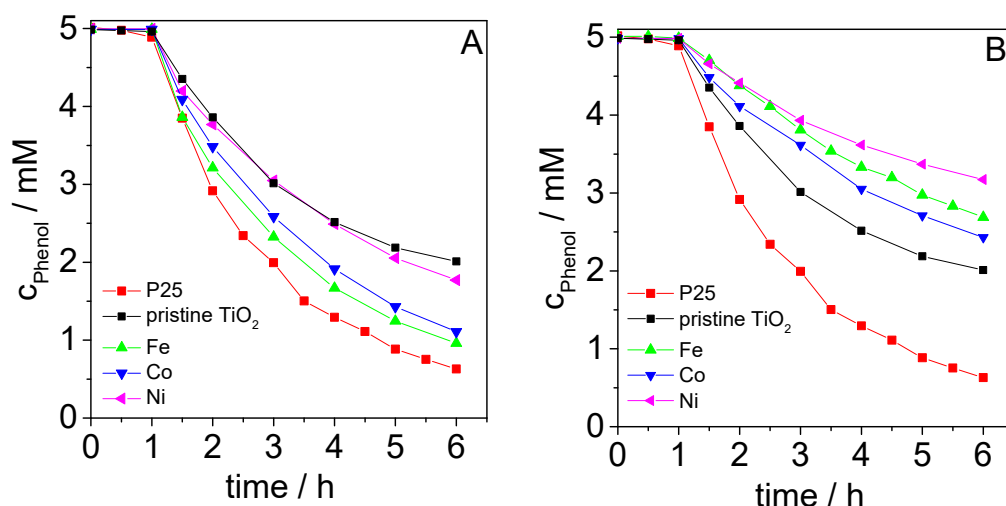


Figure 36. Degradation of phenol under UV irradiation as function of time, A) samples doped with 0.5 mol% metal and B) samples doped with 5 mol% metal, synthesis conditions: molar $\text{P123}/(\text{TiO}^{\text{I}}\text{Pr})_4 = 0.0163$, $T_{\text{evap}} = 40\text{ }^{\circ}\text{C}$, $T_{\text{extrac}} = 78\text{ }^{\circ}\text{C}$ (4 times), calcination: $25 - 450\text{ }^{\circ}\text{C}$ with $1.2\text{ }^{\circ}\text{C}/\text{min}$ in Ar than 2 h at $450\text{ }^{\circ}\text{C}$, $25 - 450\text{ }^{\circ}\text{C}$ with $1.2\text{ }^{\circ}\text{C}/\text{min}$ in O_2 than 2 h at $450\text{ }^{\circ}\text{C}$).

Table 7. Comparison of pseudo first order rate constants in phenol degradation over doped mesoporous titania under UV irradiation.

dopants	0.5 mol%		5 mol%	
	k_{obs} h^{-1}	R^2	k_{obs} h^{-1}	R^2
P25*	0.43	0.9902		
TiO_2^*	0.21	0.9496		
Fe/ TiO_2	0.35	0.9859	0.13	0.9872
Co/ TiO_2	0.31	0.9953	0.15	0.9866
Ni/ TiO_2	0.22	0.9817	0.10	0.9747

*pristine titania

Moreover, the photocatalytic activity of these samples was tested in phenol degradation under Xenon lamp as shown in Figure 37. Ordered mesoporous titania doped with 0.5 mol% Fe or Ni exhibited higher photocatalytic activity than the pristine titania at irradiation with white light, but, Co-doped showed less photoactivity (Figure 37A). According to results presented in Figure 37A, photocatalytic activities of the samples were in the order of $\text{Fe} > \text{Ni} > \text{pristine TiO}_2 > \text{Co}$. The observed differences in photocatalytic activity might be explained by interaction of the doping element itself or defects created in their environment with the charge carriers. For Fe and Ni -doped samples, the significant improvement in the photoactivity of TiO_2 to degrade the phenol might be that the Fe and Ni ions promote the separation of photogenerated charge carriers. For Co-doped sample, however, it might be

assumed that Co ions could increase the rate of the recombination of electron-hole pairs. This was because Co ions might be played the role of recombination centers. Phenol degradation followed a pseudo first order reaction and the degradation rate was presented in Table 8.

Whereas, reducing of the photocatalytic activity of Fe and Ni has been found under visible light illumination (Figure 37B). Under these conditions, no significant influence of the metal doped on the photocatalytic activity of the titania was observed. The metal ions might be serving as electron-hole recombination centers. In contrast, the photocatalytic activities of all obtained samples have been found to be higher than P25 under visible light illumination (Figure 37B). The reason has already been explained. From the results in Table 8, it can be seen that phenol degradation followed a zero order reaction. The degradation rate of phenol was also presented in Table 8.

Comparing the photocatalytic performance of these samples under white light illumination (Figure 37A) with those under UV irradiation (Figure 36A), it can be seen that there are differences in phenol degradation between the Ni and Co-doped samples. This might be attributed to the difference in the testing conditions. Here the experiments were performed under Xenon lamp (using white light) and UV irradiation. Moreover, both experiments were carried out at different setups including amount of metal doped-TiO₂ photocatalyst, concentration of phenol, and volume of solution.

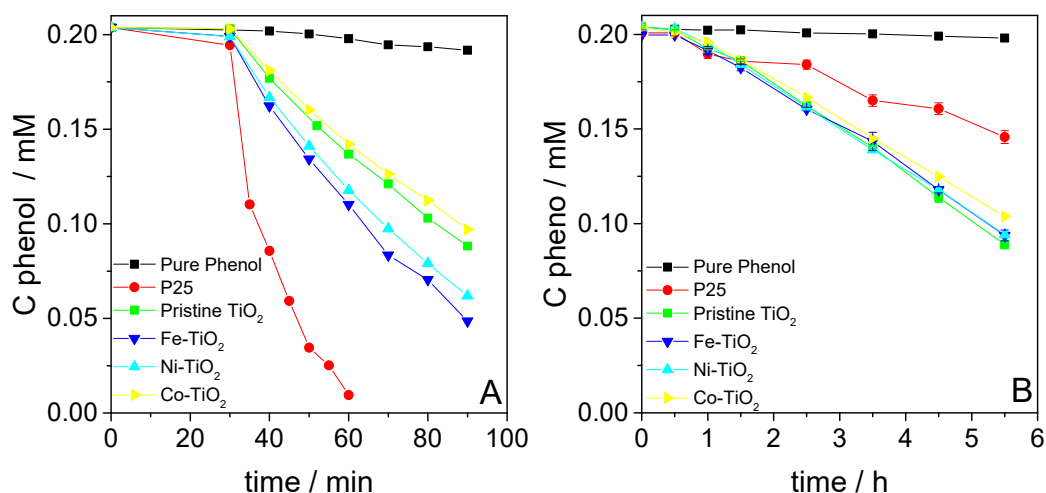


Figure 37. Degradation of phenol under Xenon lamp as function of time samples doped with 0.5 mol% metal A) white light and B) visible light ($\lambda > 420$ nm), synthesis conditions: molar P123/(TiO₂Pr)₄ = 0.0163, Tevap = 40 °C, Textrac = 78 °C (4 times), calcination: 25 – 450 °C with 1.2 °C/min in Ar than 2 h at 450 °C, 25 – 450 °C with 1.2 °C/min in O₂ than 2 h at 450 °C).

Furthermore, in order to investigate the influence of repeated synthesis of metal-doped TiO_2 on the photocatalytic activity, the 0.5 mol% Fe-doped titania sample was synthesized again and applied in phenol degradation (molar ratio $\text{P123}/(\text{TiO}^i\text{Pr})_4$ 0.0163, at 40 °C evaporation temperature, 4 times surfactant extraction, calcination at 450 °C). Figure 38A indicates that small differences in photocatalytic activity between both samples appeared. In order to evaluate whether there was an error in temporal evolution of phenol concentration in a single experiment, a fresh 0.5 mol% Fe-doped titania sample was tested two times with the same conditions under visible light illumination. Figure 38B shows that only minor differences in phenol degradation between the two tests were observed.

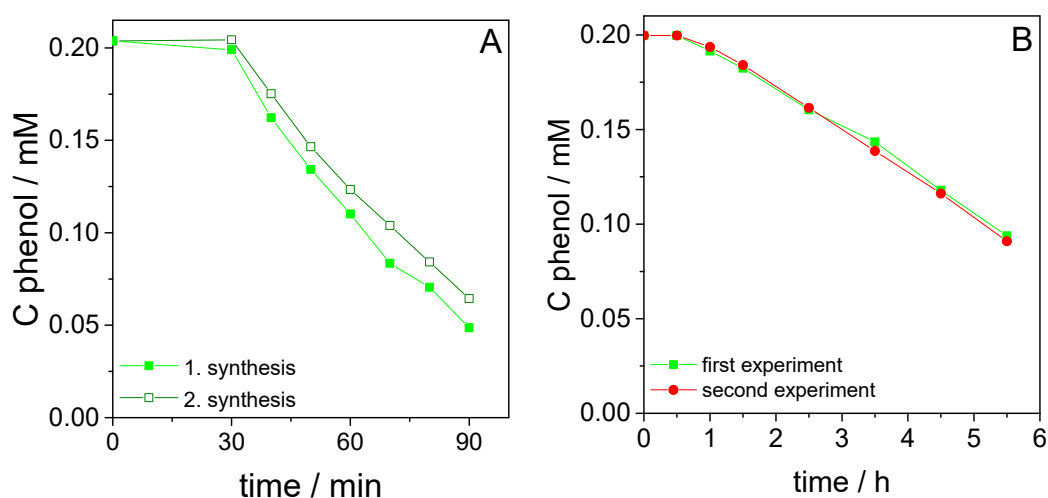


Figure 38. Influence of reaction time on phenol concentration for titania doped with 0.5 mol% Fe A) repeated synthesis (Xenon lamp without filter) and B) two tests of the same material under identical conditions ($\lambda > 420$ nm), (synthesis conditions: molar $\text{P123}/(\text{TiO}^i\text{Pr})_4$ = variable, $T_{\text{evap}} = 40$ °C, $T_{\text{extrac}} = 78$ °C (4 times), calcination: 25 – 450 °C with 1.2 °C/min in Ar than 2 h at 450 °C, 25 – 450 °C with 1.2 °C/min in O_2 than 2 h at 450 °C).

Table 8. Comparison of zero and first order rate constants in phenol degradation over doped mesoporous titania under Xenon lamp.

dopants	Xenon lamp		Xenon lamp with filter	
	k_{obs} h^{-1}	R^2	k_{obs}	R^2
P25*	0.10	0.9703	0.19	0.9785
TiO_2^*	0.13	0.9979	0.20	0.9944
Fe/ TiO_2	0.18	0.9897	0.20	0.9978
Co/ TiO_2	0.12	0.9991	0.20	0.9974
Ni/ TiO_2	0.19	0.9964	0.20	0.9992

* Pristine titania

3.3 Nitrogen doped ordered mesoporous titania

It has been shown (section 3.1.1.1.) that the repeated synthesis can be led to materials that differ in degree of ordering after calcination even if the synthesis was performed using identical preparation parameters. In order to exclude that instabilities of the synthesis process superimpose the results of thermally induced crystallization in presence of gaseous ammonia, titania samples obtained after surfactant extraction from six single preparations were mixed together resulting in 8 g of precursor material. The single titania sample was synthesized with a molar ratio $\text{P123}/(\text{TiO}^{\text{I}}\text{Pr})_4$ of 0.0163, a solvent evaporation temperature of 40 °C and two surfactant extraction steps at 78 °C. The mixture of the material obtained after surfactant extraction is referred as am-TiO₂. A small fraction of this mixture was calcined under condition as applied before (calcination under argon and oxygen). This sample is called TiO₂-Ar/O₂.

Figure 39A presents the XRD patterns of am-TiO₂ and TiO₂-Ar/O₂. It can be seen that titania obtained after surfactant extraction was amorphous. After thermal treatment, obvious reflexes of anatase phase (JCPDF card No. 01-073-1764) and minor reflexes β -TiO₂ phase (JCPDF card No. 00-035-0088) were observed.

SAXS patterns of am-TiO₂ and TiO₂-Ar/O₂ are presented in Figure 39B. An ordered mesoporous structure has been noted for am-TiO₂ (Figure 39B) as shown by the presence of the d_{100} reflexes. The strong broadening of the d_{100} reflexes in the pattern of TiO₂-Ar/O₂ indicates a loss of mesoporous ordering during the calcination step as already observed previously. The presence of hexagonal ordered domains inside both samples (am-TiO₂ and TiO₂-Ar/O₂) was confirmed by STEM-HAADF (Figure 40A and B).

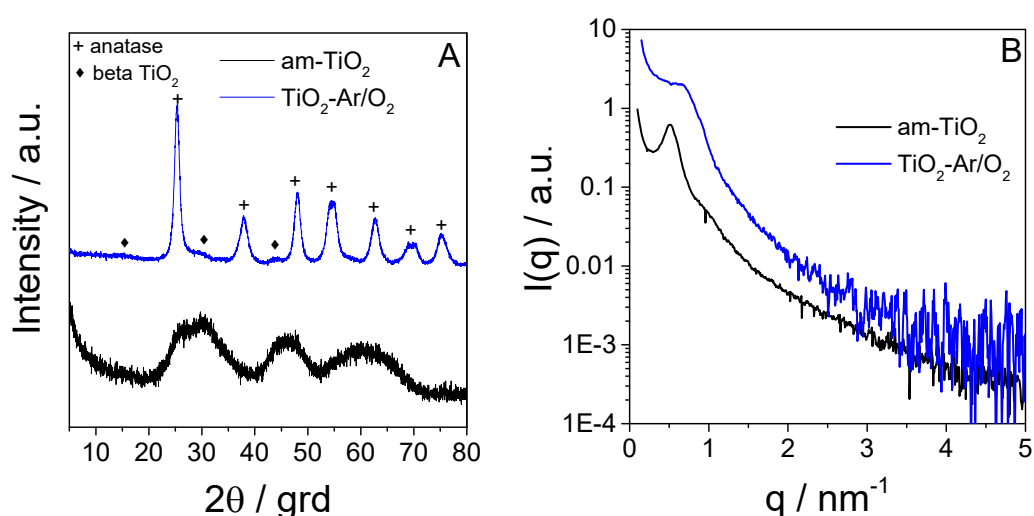


Figure 39. A) XRD powder patterns and B) SAXS patterns of am-TiO₂ and of TiO₂-Ar/O₂ (am-TiO₂ after heating under Ar, 22-450 °C/6.5 h followed from treatment under O₂ (450 °C, 2 h)).

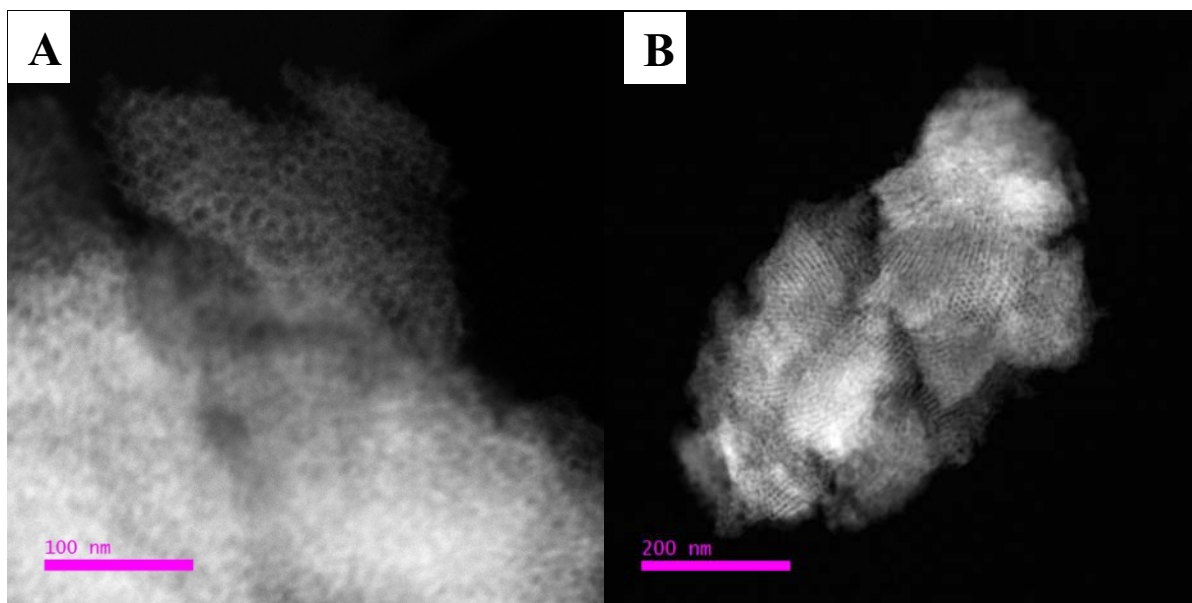


Figure 40. STEM-HAADF A) of am-TiO₂ and B) of TiO₂-Ar/O₂ (am-TiO₂ after heating under Ar followed from treatment in oxygen atmosphere (Ar: 22-450 °C/6.5 h followed from treatment under O₂ atmosphere (450 °C, 2 h)).

Figure 41A shows the ATR-IR spectra of am-TiO₂ and TiO₂-Ar/O₂ samples. The spectrum of am-TiO₂ showed a strong absorption bands around 3200 cm⁻¹, which was ascribed to the surface -(OH) stretching vibrations and/or adsorbed water molecules [177]. The band located at 1633 cm⁻¹ can be attributed to the bending vibration of O-H bond resulting from surface adsorbed water molecules [178]. The band at 1433 cm⁻¹ can be attributed to bending vibrations of NH₄⁺ [177]. The presence of this band indicates that during surfactant extraction in boiling ethanol ammonia species were not completely removed. The protons of NH₄⁺ are considered as strong Lewis acid that can bind to oxygen [177]. NH₄⁺ was formed by reaction of protonated Ti-species with ammonia during the precipitation step. Thermal treatment of the sample in Ar/O₂ atmosphere led to a significant change of the IR spectrum. Intensity of the broad absorption band around 3200 cm⁻¹ and that of the band at 1633 cm⁻¹ were decreased which might indicate that a part of the water was removed during calcination. Moreover, the band located at 1433 cm⁻¹ was nearly disappeared and new peaks were located at 3735 and 1511 cm⁻¹ appeared which might be attributed to the stretching vibrations of Ti⁴⁺-OH surface hydroxyl groups (3735 cm⁻¹) and NH₂ or NO₂/NO groups (1511 cm⁻¹), respectively [177]. UV/vis spectra of both samples are presented in Figure 41B. Absorption in the visible light range was higher, when the sample was thermally treated. This might be attributed to nitrogen incorporation into the TiO₂ lattice and the formation of new electronic state above the valence band [179].

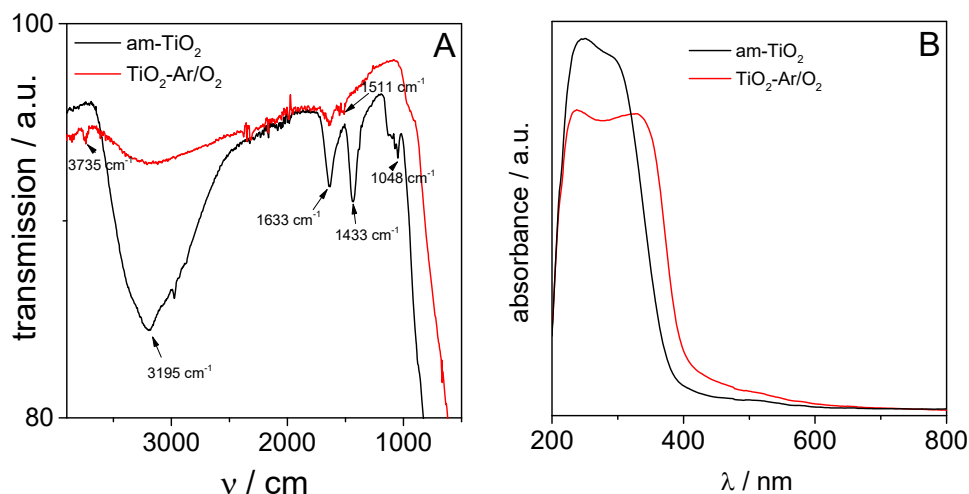


Figure 41. A) UV/Vis spectra and B) ATR-IR spectra of titania obtained after surfactant extraction (am-TiO₂) and after calcination (TiO₂-Ar/O₂, 22-450 °C/6.5 h, followed from oxygen treatment (450 °C, 2 h).

Finally, the surface region of the amorphous TiO₂ was characterized by XPS (see Figure 42). The core level Ti (2p 3/2) spectra contain two peaks located at 458.51 eV and 457.46 eV. The peak located at 458.51 eV was attributed to Ti⁴⁺ and that peak at 457.46 eV might be assigned to Ti³⁺ [146, 180] or the presence of Ti⁴⁺ in different environment indicated by formation of β-TiO₂ phase after thermal treatment. The core level O (1s) spectra showed a main peak at 529.7 eV due to formation of Ti-O bonds [181]. The nature of the small peak at 525.48 eV is presently unknown. Furthermore, XPS spectra of sample am-TiO₂ indicated the presence of both carbon residuals and nitrogen on the titania surface that was already observed by ATR-IR. The peaks in the C(1s) spectra were located at 284.56 and 288.39 eV, which might be assigned to C-C and O-C=O bonds, respectively [146]. Carbon residues resulting from the titania precursor (Ti(OⁱPr)₄) or the surfactant (P123) still stay in the sample after extraction. The carbon content on the surface achieved 26.4 wt.%. XPS spectra of the N (1s) region showed peaks located at 397.74 and 400.21 eV. The assignment of these peaks to nitrogen species is still under debate. E.g., Ti-N (N substitutional) and Ti-O-N (N interstitial) bonds were attributed to both different signals [145].

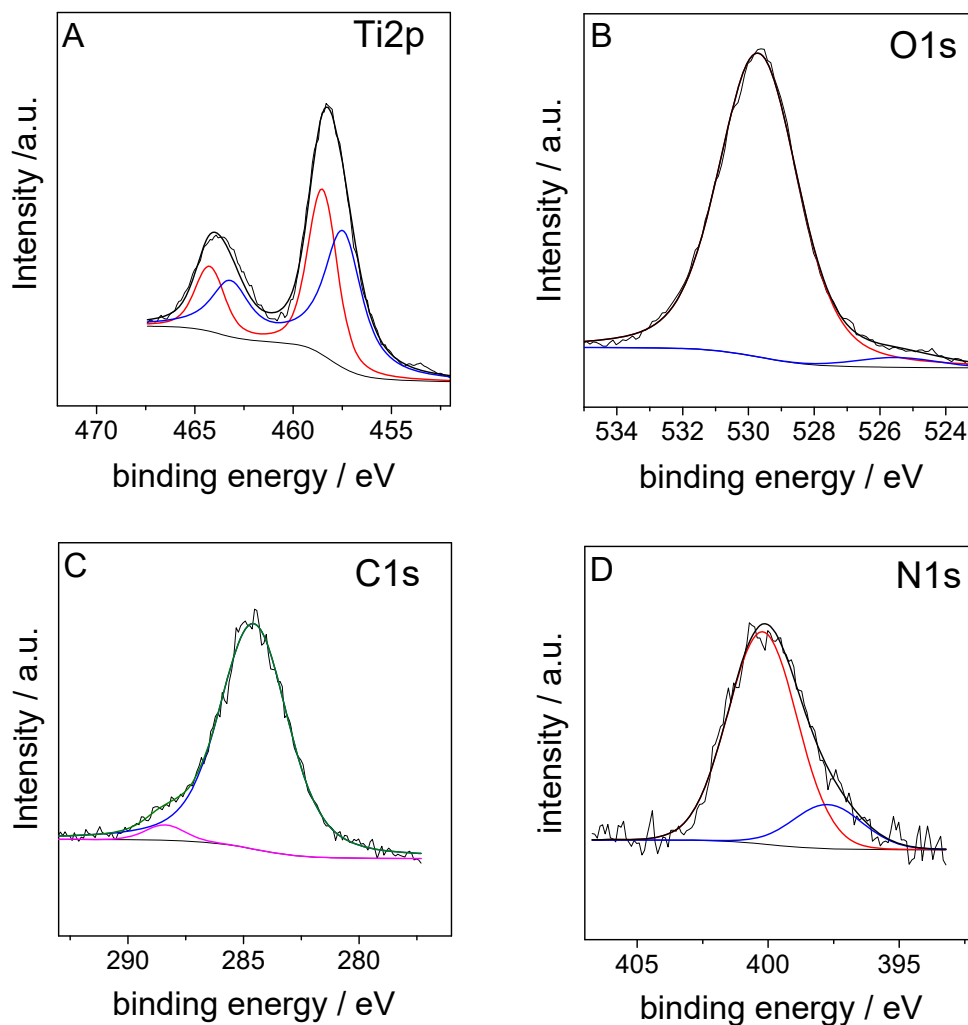


Figure 42. HR XPS spectra from am-TiO₂, A) Ti2p, B) O1s, C) C1s, and D) N1s.

3.3.1 Effect of the temperature

In order to investigate the effect of the heating temperature in presence of gaseous ammonia on the structural characteristics and photocatalytic activity of the formed mesoporous TiO₂, single fractions of the mixed titania powder (am-TiO₂) were heated in presence of ammonia with different temperature values (350, 450, and 550 °C). The samples obtained at different heating temperatures were referred as N-TiO₂-350NH₃, N-TiO₂-450NH₃ and N-TiO₂-550NH₃.

Figure 43A shows XRD patterns of the N-doped mesoporous TiO₂ obtained by heating at different temperatures in ammonia atmosphere. The sample treated at 350 °C was still amorphous. Crystalline samples were obtained when the am-TiO₂ was heated to 450 and 550°C. This indicates that the titania crystallinity was increasing with raising heating temperature. The main reflexes in the XRD patterns could be indexed to an anatase phase of

TiO₂ (JCPDS File: 00-064-0863). In addition, minor reflexes of a β -TiO₂ phase (JCPDS File: 00-046-123, JCPDS File: 01-075-644) were also observed. As shown in Table 9, crystallite size gradually increases with increasing heating temperature. This might be due to the nitrogen is uniformly distributed either in the TiO₂ crystal structure or occupying interstitial or substitutional sites [182].

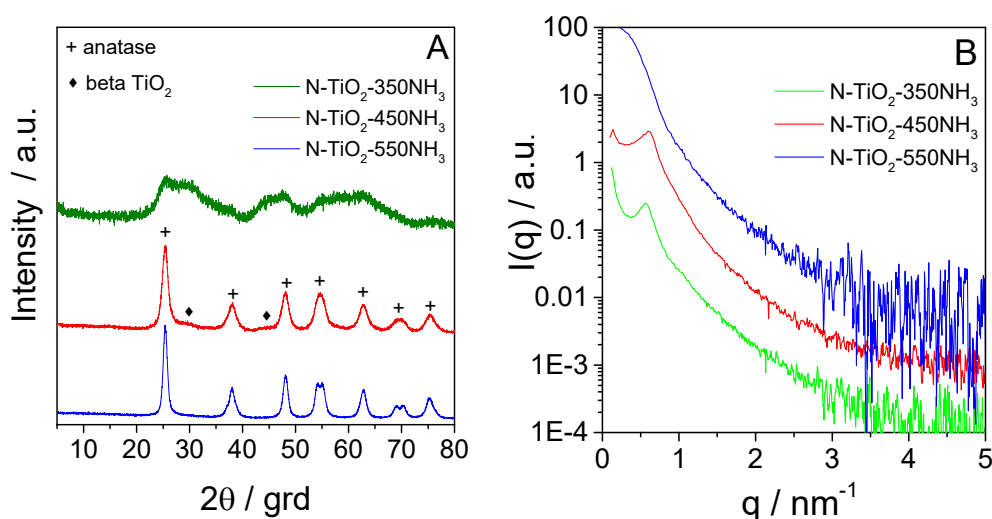


Figure 43. A) XRD powder patterns and B) SAXS patterns of am-TiO₂ samples heated under NH₃ atmosphere using different heating temperatures 350, 450, and 550 °C.

SAXS patterns of samples synthesized with different heating temperature are presented in Figure 43B. Until a temperature of 450 °C mesoporous ordering seems to be only slightly effected from temperature. In contrast, heating sample to 550 °C leads to a collapse of the mesoporous ordering. One reason might be the formation of bigger titania crystallites with increasing temperature (see Table 9) due to the mean crystallite size increases from 5.4 to 7.0 nm with raising temperature from 450 to 550 °C. The presence of hexagonal ordered mesoporous domains in N-TiO₂-450NH₃ was also confirmed by STEM-HAADF. The image (Figure 44), shows the regular arrangement of the mesopores inside of a single particle. Moreover, the STEM-HAADF image and the EELS spectrum (Figure 45) confirm not only the presence of nitrogen; but they prove also that the nitrogen is located mainly on the surface of titania.

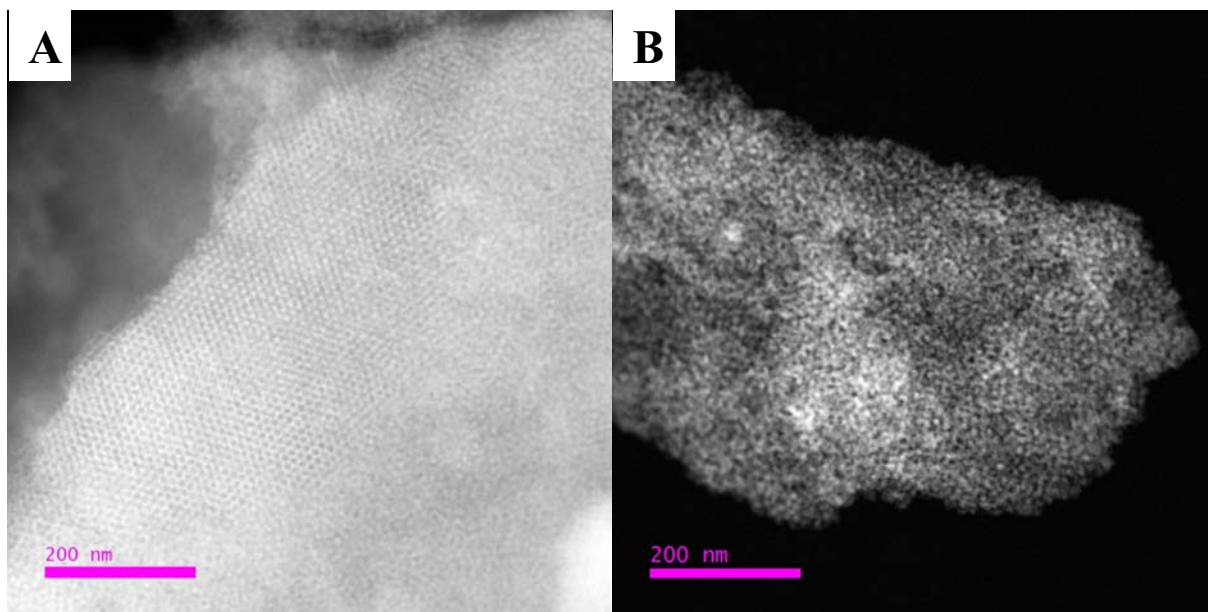


Figure 44. STEM-HAADF images of A) N-TiO₂-450NH₃ obtained after heating under NH₃ atmosphere at 450 °C and B) N-TiO₂-450NH₃/O₂ (sample was obtained after successive heating O₂ (450 °C, 2 h)).

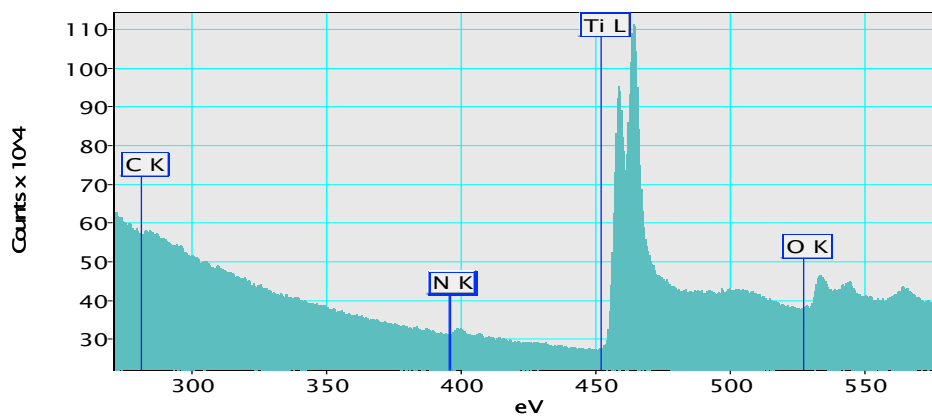
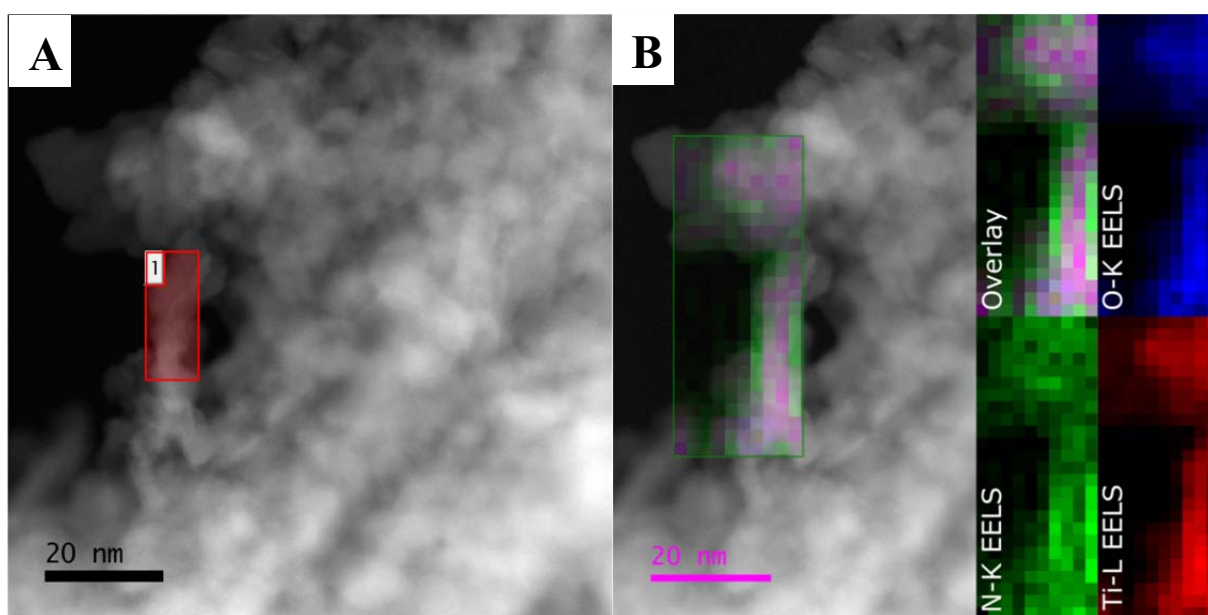


Figure 45. Sample N-TiO₂-450NH₃ A) STEM-HAADF image with marked area used for spectrum C, B) HAADF overlaid with elemental maps of Ti, O, and N. C) The EELS spectrum showed the presence of nitrogen on the surface of TiO₂.

Figure 46B presents ATR-IR spectra of N-TiO₂-350NH₃, N-TiO₂-450NH₃ and N-TiO₂-550NH₃. All samples show an IR-absorption band at 3200 cm⁻¹ similar to am-TiO₂, which was ascribed to the surface-(OH) stretching vibrations of the coordinated water molecules. The band located around 1630 cm⁻¹, attributed to the bending vibration of O-H bond from surface adsorbed water, was also visible. The position of the band located around 1430 cm⁻¹, assigned to the presence of NH₄⁺ [183], was slightly different in the single samples. Moreover, intensity of this band compared to intensity of the band located at 1630 cm⁻¹ decreased with increasing heating temperature. This indicates that amount of NH₄⁺ decreases with increasing heating temperature despite presence of ammonia in gas phase. General characteristics of samples obtained after ammonia treatment are summarized in Table 9. Results presented there confirm that increasing heating temperature lead to a decrease of the nitrogen content.

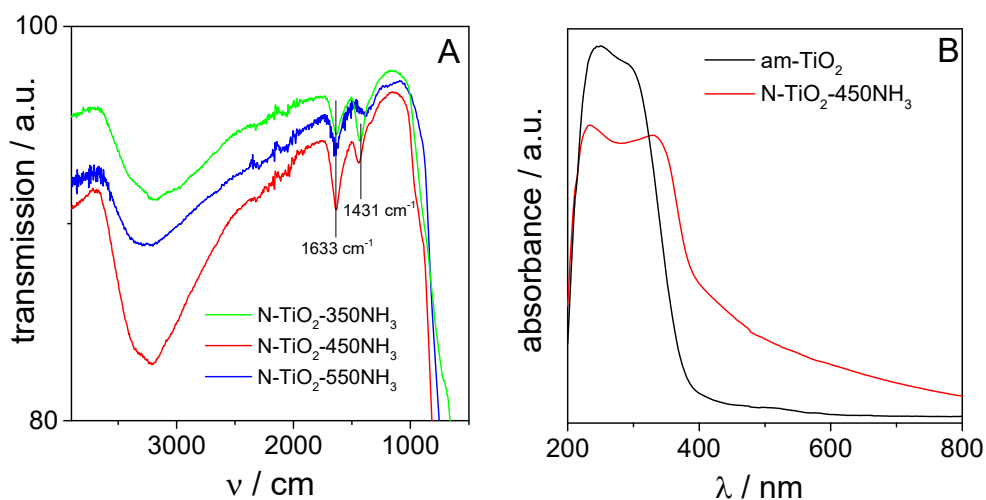


Figure 46. A) ATR-IR spectra of am-TiO₂ samples heated under NH₃ atmosphere using different heating temperatures and B) UV/Vis absorption spectra.

The UV/Vis spectra of sample N-TiO₂-450NH₃ and am-TiO₂ are shown in Figure 46A. The absorption spectra of the amorphous titania (am-TiO₂) shows only low light absorption in the visible light range. Here, absorption in the visible range might be attributed to the presence of carbon species and/or nitrogen. The sample heated in ammonia atmosphere show much higher light absorption in the visible range compared to am-TiO₂. Wang et al. [181] observed an increase in the absorption in visible region with increasing of NH₃ treatment temperature to 600°C. The calculated band gap of sample N-TiO₂-450NH₃ (3.03 eV) was clearly lower than that of am-TiO₂ (3.38 eV) although the sample am-TiO₂ also contains nitrogen. Here, the nitrogen might be weaker bounded on the titania surface. The reducing of the band gap after heating in ammonia atmosphere might be considered as an indication that during the thermal treatment some nitrogen was introduced into the titania lattice [146].

Table 9. General characteristics for samples obtained after heating under NH₃ at different temperatures and after following treatment in oxygen flow (450 °C, 2 h).

Samples	N* wt. %	BET m ² /g	V _p cm ³ /g	d _{pore} nm	d _{cryst.} nm	band gap eV
m-TiO ₂	1.3	-	-	-	-	3.38
N-TiO ₂ -350NH ₃	1.3	-	-	-	-	-
N-TiO ₂ 350NH ₃ /O ₂	<0.06	188	0.3	4.4	5.4	3.14
N-TiO ₂ -450NH ₃	0.3	277	0.49	4.9	5.2	3.03
N-TiO ₂ -450NH ₃ /O ₂	<0.09	238	0.43	5.3	4.9	3.15
N-TiO ₂ -550NH ₃	0.2	-	-	-	7.0	-
N-TiO ₂ -550NH ₃ /O ₂	<0.06	150	0.36	6.7	7.0	3.10

*the nitrogen amount was determined by CHN-analysis using the corresponding titania sample

In order to investigate the chemical surface states after treatment in ammonia atmosphere, N-TiO₂-450NH₃ have been characterized by XPS (Figure 47). The core level Ti (2p_{3/2}) spectra shows after deconvolution peaks located at 457.9, 458.7, and 459.7 eV, which might be attributed to Ti³⁺ and Ti⁴⁺ 2p_{3/2}, [146, 180]. The presence of Ti³⁺ indicates the removal of oxygen from TiO₂ lattice, which produces oxygen vacancies [184]. The core level O (1s) spectrum shows the presence of two different oxygen bonds. The first binding energy located at 529.7 due to formation of Ti-O. The second peak with binding energy located at 530.9 eV might be attributed to the hydroxyl group (-OH) [145, 185]. The N (1s) region showed signals at 399.7 and 401.4 eV, which indicates the presence of anionic N in N-Ti-O bonds and oxidized N in Ti-O-N bonds [186]. The core level C (1s) spectra showed two peaks at 284.8 and 288.03, which can be assigned to C-C and O-C=O bonds, respectively [146].

Generally, as well known, the assignment of the XPS peak of N1s in titania is still under debate and controversial hypothesis have been presented [72, 187]. Previous reports indicate that a peak at about 396 eV can be attributed to substitutional nitrogen doping ($\text{TiO}_{2-x}\text{N}_x$) [188, 189]. In contrast, the peak at higher binding energies in the range (399-404 eV) is attributed to interstitial nitrogen doping (TiO_2N_x) [145]. It was found that binding energy of interstitial nitrogen is higher than that of substitutional nitrogen. This might be because the nitrogen doping into the TiO_2 lattice reduces the electron density on the nitrogen due to the high electronegativity of oxygen. These changes in the nitrogen environment led to significant differences in the nitrogen 1s XPS spectral region [187]. In contrast, other studies assumed that the peak in the range 397.8-399.9 eV has to be attributed to substitutional nitrogen as N-Ti-N and O-Ti-N [145, 178].

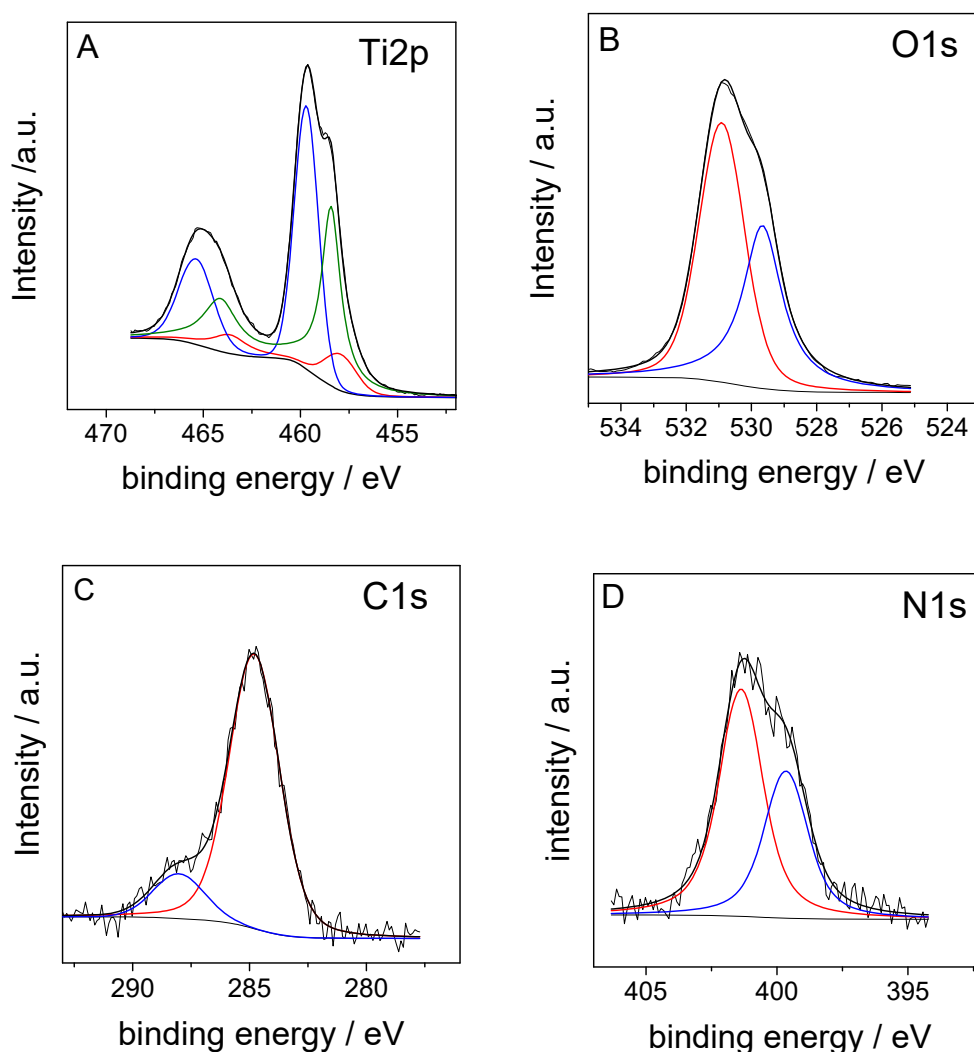


Figure 47. HR XPS spectra from am-TiO₂ after heating in NH₃ to 450 °C, A) Ti2p, B) O1s, C) C1s, and D) N1s.

Next, the effect of the successive oxygen treatment was studied. For that reason, the samples prepared under ammonia atmosphere at different temperatures were calcined in oxygen flow at 450 °C. Figure 48 presents the X-ray diffraction and SAXS patterns of these samples. The material synthesized under ammonia at 350 °C shows after treatment with oxygen at 450 °C reflexes of anatase and β -TiO₂. Interestingly, the mean crystallite sizes obtained after treatment with ammonia does not increase during the oxygen treatment (see Table 9). However, the SAXS patterns show a loss of mesoporous ordering after oxygen treatment for samples prepared under ammonia at 350 and 450 °C which might indicate that at comparable temperature the presence of oxygen has a larger effect on ordering of the mesoporous structure as the presence of ammonia. STEM-HAADF image of N-TiO₂-450NH₃/O₂ (Figure 44B) confirm the loss of mesoporous ordering during treatment with oxygen at 450 °C as derived from SAXS pattern. The loss of ordering during oxygen treatment is also supported by results of nitrogen sorption. As shown in Table 9, BET surface decreases after treatment with oxygen from 277 to 238 m²/g. Interestingly, the sample prepared under ammonia atmosphere at 450 °C showed after successive oxygen treatment relatively high BET surface areas.

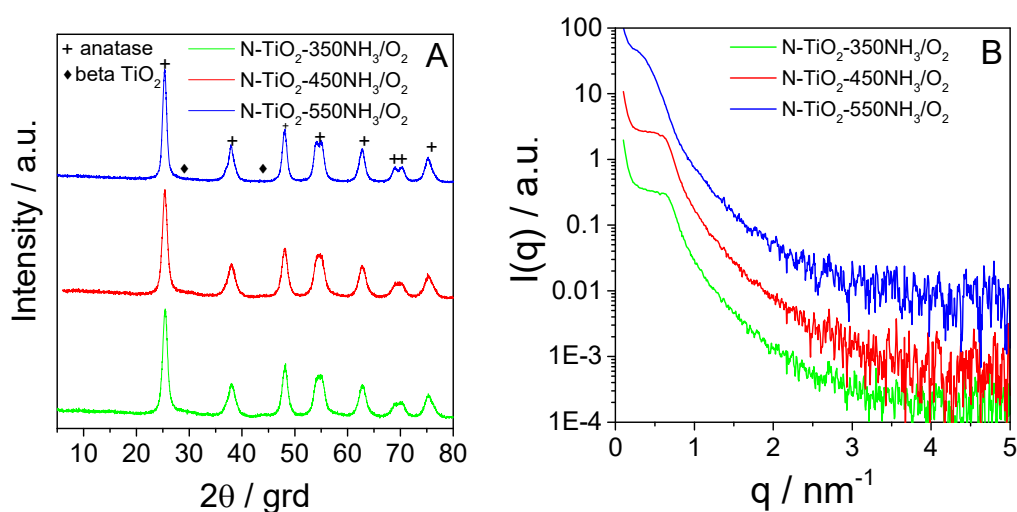


Figure 48. A) XRD patterns and B) SAXS patterns of samples calcined under NH₃ using different heating temperatures followed from successive oxygen treatment (450 °C, 2 h).

Figure 49A shows the ATR-IR spectra of N-TiO₂-350NH₃/O₂, N-TiO₂-450NH₃/O₂ and N-TiO₂-550NH₃/O₂. In all three samples a broad absorption band located at 3200-3250 cm⁻¹ was observed similar to the bands found in the samples after ammonia treatment. The band located at 1633 cm⁻¹ was also still there. This shows that all samples contained water probably adsorbed on the titania surface. However, the band located at 1433 cm⁻¹ was disappeared after

oxygen treatment. Because the band was attributed to the presence of NH_4^+ it has to be assumed that the NH_4^+ was removed during oxygen treatment. This conclusion is supported by results of elemental analysis which show a clear decrease of nitrogen amount after treatment with oxygen in all samples (see Table 9). Figure 49B shows the UV-vis spectra of the samples treated with oxygen. It can be seen that all samples show light adsorption the visible range between 400 and 620 nm. An effect of the final heating temperature on light absorption is also visible. Light absorption in the visible range after oxygen treatment was lower than after treatment with ammonia (see Figure 46B). This indicates again that during the treatment with oxygen a large part of nitrogen located near the titania surface after ammonia treatment was removed. Moreover, the band gap estimated after oxygen treatment was higher than the bandgap obtained when the samples were treated only in ammonia atmosphere (see Table 9). The visible light absorption shoulder indicates that some localized states in the band gap of TiO_2 are responsible for the visible light absorption. Moreover, the significant increase of the absorption in the visible range can be assigned to the contribution of both the doped nitrogen atoms and oxygen vacancies in the lattice. This is due to the interstitial nitrogen atoms induced the local states near the valence band edge and the oxygen vacancies give rise to the local states below the conduction band edge [181]. The presence of oxygen vacancies are confirmed by XPS analysis (see Figure 50). The different light absorption of the samples might be due to different nitrogen species.

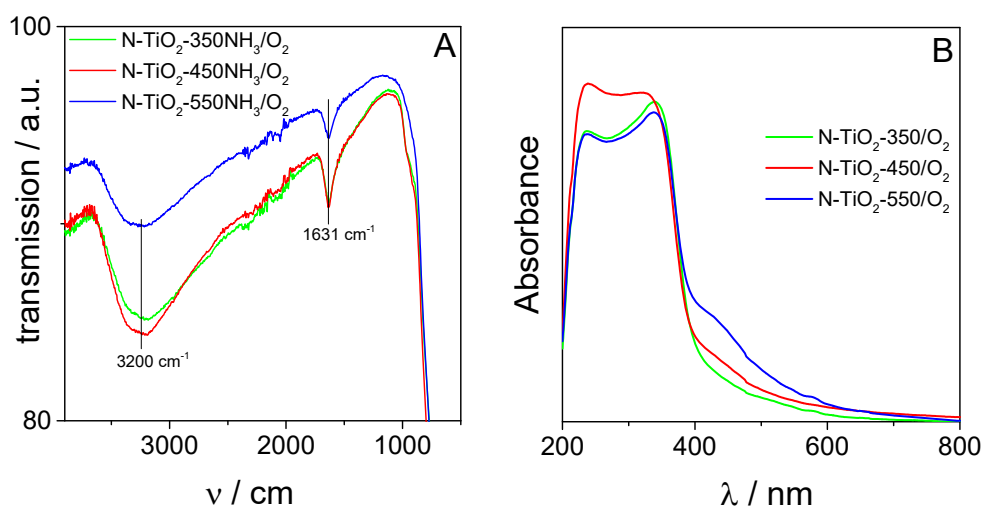


Figure 49. A) ATR-IR spectra and B) UV/Vis absorption spectra of samples heated under NH_3 using different heating temperatures followed from successive oxygen treatment (450 °C, 2 h).

To get further information about the influence of the oxygen treatment on the state of the titania surface, the sample N-TiO₂-450NH₃/O₂ was also characterized by XPS. The influence of heating under oxygen on the spectra of Ti 3p, O 1s, N 1s, and C 1s was observed

through shifting in the binding energies. The first peak of Ti 2p changed from 457.9 eV to lower binding energy of 456.75 eV. This peak could be assigned as Ti^{3+} . The second and third peaks were shifted by -0.36 and +0.26 eV, respectively. These peaks (458.34 and 459.96 eV) are related to Ti^{4+} . The core level O (1s) spectra showed a main peak at 530.45 due to formation of Ti-O bond and a peak at 528.71 eV attributed to the oxygen of surface hydroxyl groups [145, 185]. In addition, a new peak located at 527.6 eV appeared. The nature of this peak is unknown. In the N1s spectra, the first peak was shifted from 399.7 eV to lower binding energy of 397.7 eV. This peak belongs to substitutional nitrogen in Ti-N-O bonds. The shift indicates a substitution of O^- by N^- to form Ti-N-O [81]. The second peak N1s was shifted from 401.4 eV to 400.1 eV which corresponding to oxidized nitrogen (interstitial N) such as NO or NO_2 [81]. Upon heating under oxygen, the C1s peak at 288.1 disappeared and a new peak at 282.3 eV appeared. This new peak might be attributed to the Ti-C bond [190] where the carbon replace some oxygen into the titanium oxide lattice near the surface.

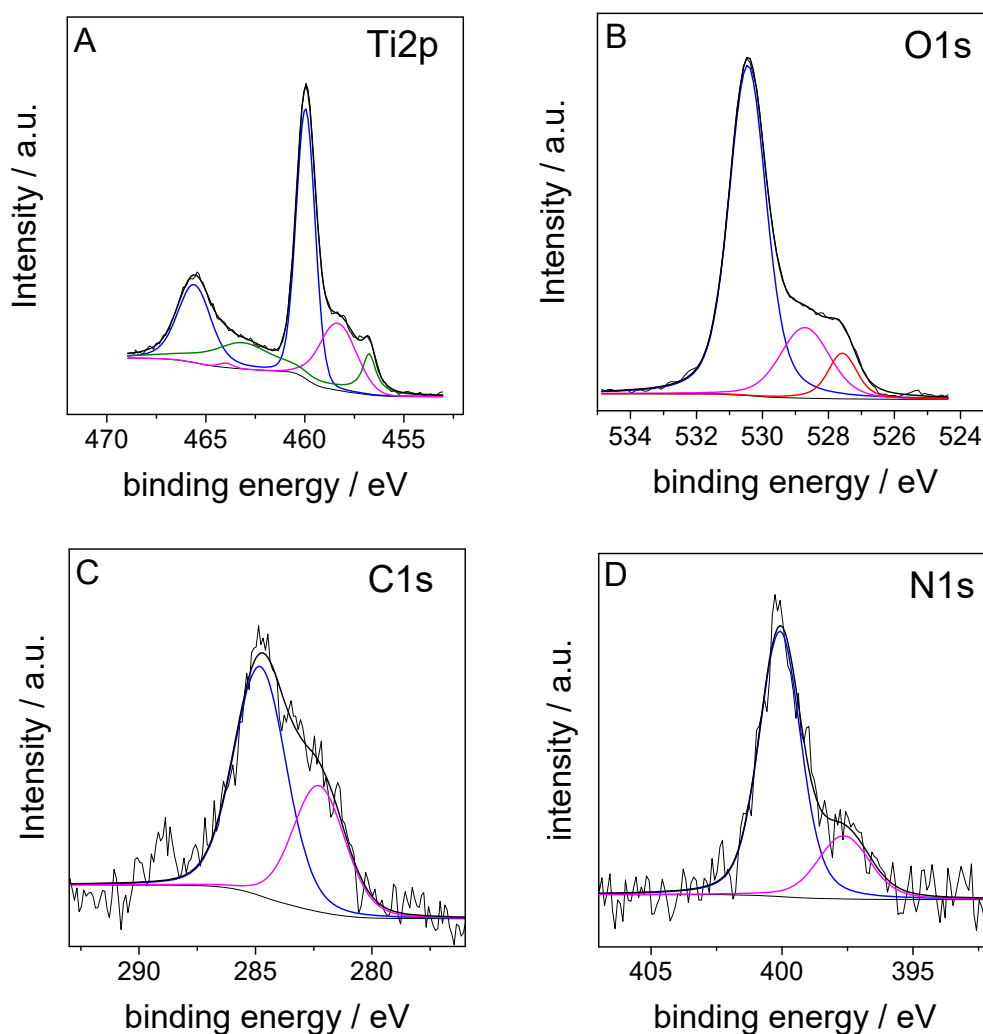


Figure 50. HR XPS spectra from am- TiO_2 after heating in NH_3 to 450 °C ($\text{N-TiO}_2\text{-450NH}_3$) followed from successive treatment in oxygen atmosphere (450 °C/2 h), A) Ti2p, B) O1s, C) C1s, and D) N1s.

In order to investigate the photocatalytic activity of the N-doped mesoporous TiO_2 selected samples obtained after ammonia treatment were tested applying Xenon lamp as irradiation source. Figure 51 shows results of phenol degradation for the sample which was treated in ammonia atmosphere at 450°C . The presented samples differ in the amount of am- TiO_2 (86 or 500 mg) used and in time of treatment in ammonia atmosphere after achieving 450°C (0.5 or 2 h). When using white light, differences in activity between the samples are relatively small. At irradiation with visible light, clear differences in photocatalytic activity were found. Here, the sample prepared with a lower amount of am- TiO_2 showed a higher activity than the sample synthesized using a larger amount of am- TiO_2 . This indicates that the accessibility of ammonia to the powder surface during the thermal treatment might be important for the amount of nitrogen which was adsorbed or built in into the titania lattice. In order to circumvent such problems and to study the effect of single parameters, all further experiment were conducted using 500 mg of am- TiO_2 because the amount of 86 mg was too low for an extended characterization in combination with photocatalytic experiments. Furthermore, the presented results indicate that an extended treatment with ammonia at the same temperature does not lead to material with an improved photocatalytic activity.

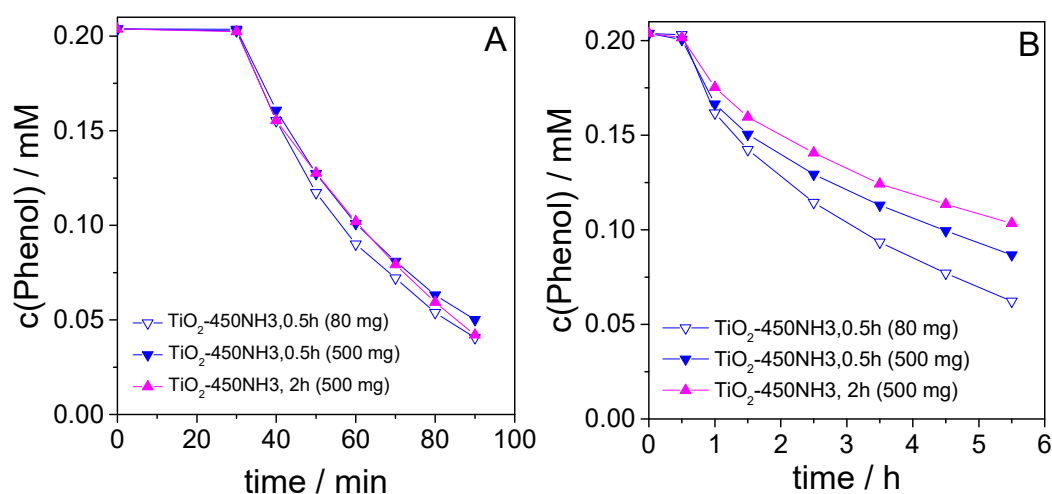


Figure 51. Degradation of phenol under Xenon lamp irradiation as function of time for samples heated under NH_3 at 450°C A) white light and B) visible light ($\lambda > 420\text{ nm}$).

Photocatalytic results obtained at irradiation with white or visible light after successive treatment of the samples with oxygen are presented in Figure 52. Photocatalytic activities at irradiation with white light were in the order of $P25 > N-TiO_2-450NH_3/O_2 > N-TiO_2-350NH_3/O_2 \sim N-TiO_2-550NH_3/O_2 \sim TiO_2-Ar/O_2$ (Figure 52A). Photocatalytic activities of the samples treated with oxygen at irradiation with visible light ($\lambda > 420$ nm) were in the order $N-TiO_2-450/O_2 > N-TiO_2-350NH_3/O_2 \sim N-TiO_2-550NH_3/O_2 \sim TiO_2-Ar/O_2 > P25 > \text{pure phenol}$ (Figure 52A). At both irradiations, the sample $N-TiO_2-450NH_3/O_2$ shows higher photocatalytic activity than the other prepared samples. The photocatalytic activity of the sample prepared under Argon followed from oxygen treatment results from the presence of nitrogen and carbon residuals. The presence of these elements after surfactant extraction was sufficient to obtain after calcination in Argon and oxygen similar photocatalytic activity than in samples prepared under ammonia treatment at 350 or 550 °C and successive oxygen treatment. In both cases the substitutional (nitrogen replaced oxygen atom of the TiO_2 lattice) and/or interstitial nitrogen (on the surface of TiO_2) will be present affecting the electronic structure of TiO_2 and improve the photocatalytic activity in the visible light region. It was assumed that interstitial nitrogen leads to formation of oxygen vacancies in the structure [75], which are responsible to increase the photocatalytic activity. The higher photocatalytic activity of the sample $N-TiO_2-450NH_3/O_2$ compared to the other prepared samples might results from the formation of Ti-C.

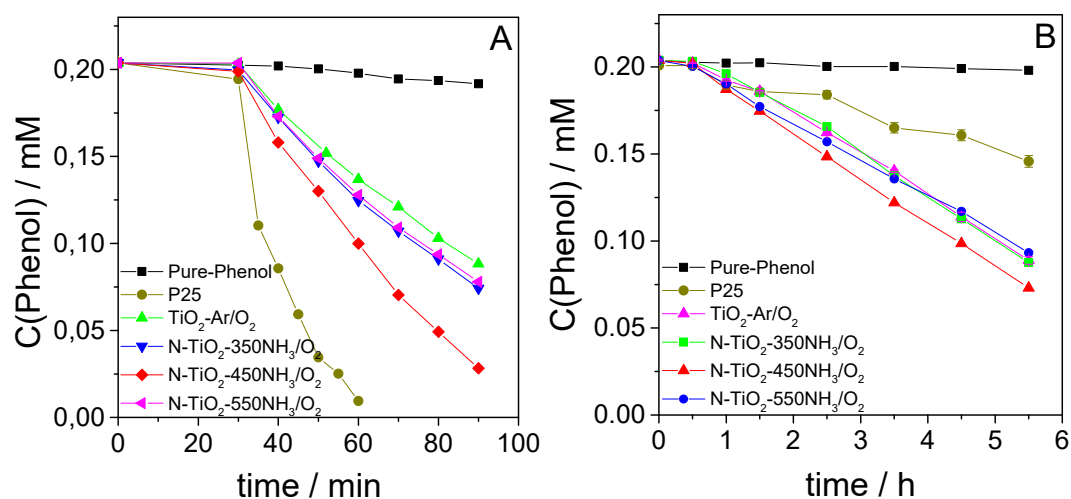


Figure 52. Degradation of phenol under Xenon lamp irradiation as function of time for samples heated under NH_3 at different heating temperatures followed from treatment in oxygen atmosphere (450 °C, 2 h), A) white light and B) visible light ($\lambda > 420$ nm).

3.3.2 Influence of the heating rate

In order to investigate the effect of the heating rate on the structural characteristics and photocatalytic activity, experiments were carried out under NH_3 atmosphere using three different heating rates (0.6, 1.2, and 2.4 $^\circ\text{C}/\text{min}$). The final temperature was always 450 $^\circ\text{C}$. The samples obtained at different heating rates were referred as $\text{N-TiO}_2\text{-0.6NH}_3$, $\text{N-TiO}_2\text{-1.2NH}_3$ and $\text{N-TiO}_2\text{-2.4NH}_3$, respectively. Additionally, all samples were also successive treated with oxygen at 450 $^\circ\text{C}$ for 2 h. These samples were referred as $\text{N-TiO}_2\text{-0.6NH}_3/\text{O}_2$, $\text{N-TiO}_2\text{-1.2NH}_3/\text{O}_2$ and $\text{N-TiO}_2\text{-2.4NH}_3/\text{O}_2$.

Figure 53A shows XRD patterns of the materials after heating in ammonia. For all samples, the peaks in the XRD patterns could be indexed to the anatase phase (JCPDS File: 00-064-0863). In addition, a small fraction of the $\beta\text{-TiO}_2$ phase is also observed (JCPDS File: 00-046-123, JCPDS File: 01-075-644). Values for the crystallite size are given in Table 10. The crystallite size was approximately independent on the heating rate and peaks around 5 nm. Treatment of these samples in oxygen atmosphere led to a small increase in crystallite size. In addition, from patterns given in Figure 53B it can be derived that the phase composition was not affected by heating in O_2 atmosphere. All samples showed after oxygen treatment reflexes of anatase and $\beta\text{-TiO}_2$ as already observed after ammonia treatment.

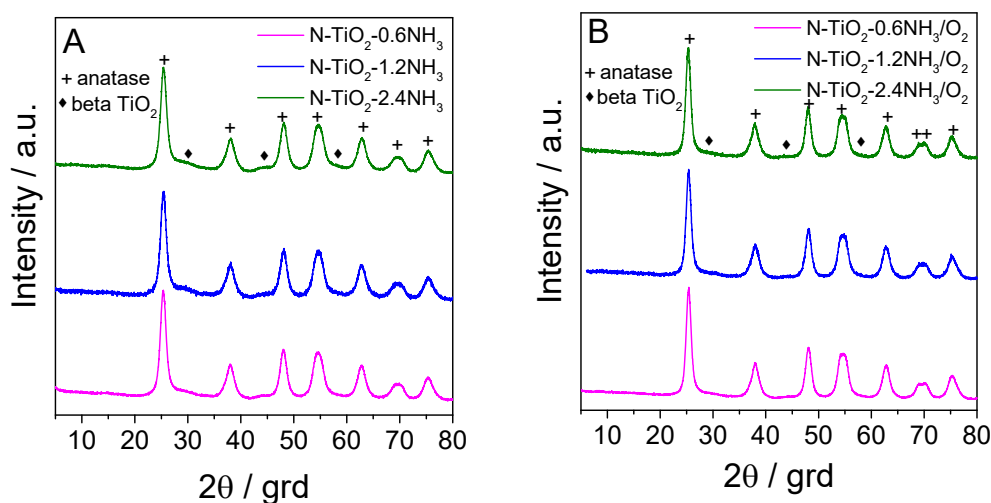


Figure 53. A) XRD powder pattern of am- TiO_2 treated with ammonia at different heating rates (0.6, 1.2, and 2.4 $^\circ\text{C}/\text{min}$) and B) SAXS patterns obtained after a successive treatment with oxygen (450 $^\circ\text{C}$, 2 h).

SAXS patterns of samples prepared at different heating rate under ammonia flow and after the following oxygen treatment are presented Figure 54. Samples obtained at different heating rates under ammonia (Figure 54A) exhibited, independent which heating rate was used, a strong d_{100} diffraction peak, which indicate the presence of ordered mesoporous titania

domains in all samples. The result hints that heating rate has only a marginal effect on mesoporous ordering in comparison to the final heating temperature. SAXS patterns of the samples obtained after successive heating in oxygen (450 °C, 2 h) are shown in Figure 54B. Here, the patterns show a clear broadening of the d_{100} reflexes compared to sample obtained under ammonia atmosphere. These results again indicate that treatment in oxygen might lead to a stronger loss of mesoporous ordering than treatment under ammonia. However, it has to be kept in mind that treatment in oxygen after achieving 450 °C was longer (2 h) than treatment in ammonia (0.5 h). The BET surface area after ammonia treatment showed a maximum for the sample heated with a heating rate of 1.2 °/min (see Table 10). Both lower (0.6 °C/min) as well as higher heating rates (2.4 °C/min) lead to lower BET surface areas. As already observed in the chapter before, BET surface area decreased when the material was successive treated with oxygen. This suggests that pores walls were lost during the oxygen treatment although the mean pore size does not increase strongly. The BET surface area for the materials heated in gaseous NH_3 (Table 10) was higher than that surface area obtained at using argon followed by oxygen for titania crystallization (see e.g. Table 2).

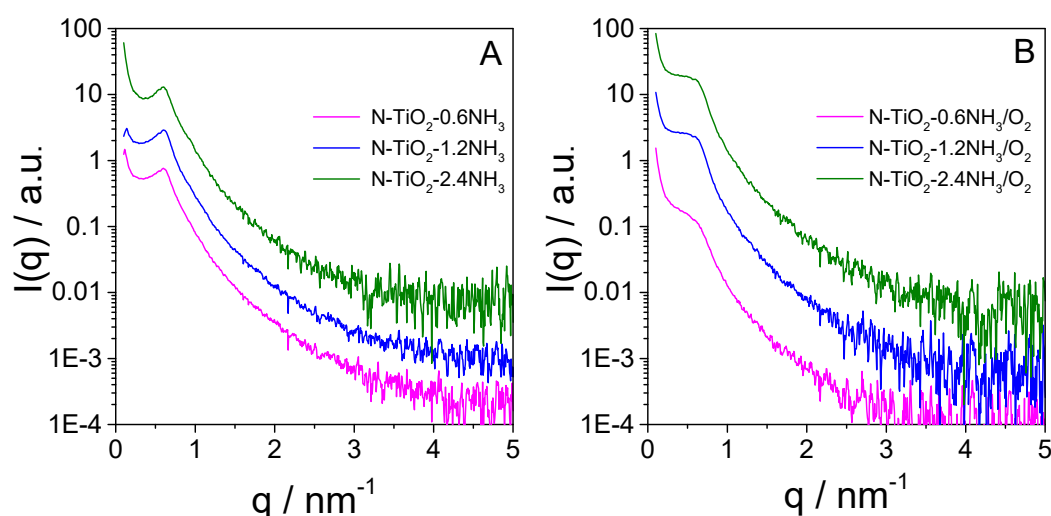


Figure 54. A) SAXS patterns of am-TiO₂ treated with ammonia at different heating rates (0.6, 1.2, and 2.4 °C/min) and B) SAXS patterns obtained after a successive treatment with oxygen (450 °C, 2 h).

Table 10. General characteristics of samples prepared with different heating rate under NH_3 atmosphere and following treatment with oxygen (450 °C, 2 h).

samples	N wt. %	BET m^2/g	V_p cm^3/g	d_{pore} nm	$d_{\text{cryst.}}$ nm	band gap eV
N-TiO ₂ -0.6NH ₃	0.2	250	0.46	5.2	5.1	3.03
N-TiO ₂ -0.6NH ₃ /O ₂	<0.06	199	0.35	5.1	5.8	3.15
N-TiO ₂ -1.2NH ₃	0.3	277	0.49	4.9	4.9	3.03
N-TiO ₂ -1.2NH ₃ /O ₂	<0.09	238	0.43	5.3	5.2	3.15
N-TiO ₂ -2.4NH ₃	0.2	249	0.44	4.3	4.8	3.07
N-TiO ₂ -2.4NH ₃ /O ₂	<0.06	197	0.35	5	5.6	3.11

Figure 55 compares UV/Vis spectra of samples obtained using different heating rate with those obtained after successive oxygen treatment. As shown in Figure 55, the heating rate has approximately no influence on the light absorption in the visible range when the samples were treated with gaseous ammonia. That might be considered as indication that the amount of nitrogen bound to the titania surface does not depend on the applied heating rate. As already observed in the previous chapter visible light absorption decreases considerably when the sample was treated with oxygen. The reason for the decrease in light absorption is the loss of nitrogen. This can be concluded from results of elemental analysis presented in Table 10 which show considerable lower nitrogen content in all samples after oxygen treatment.

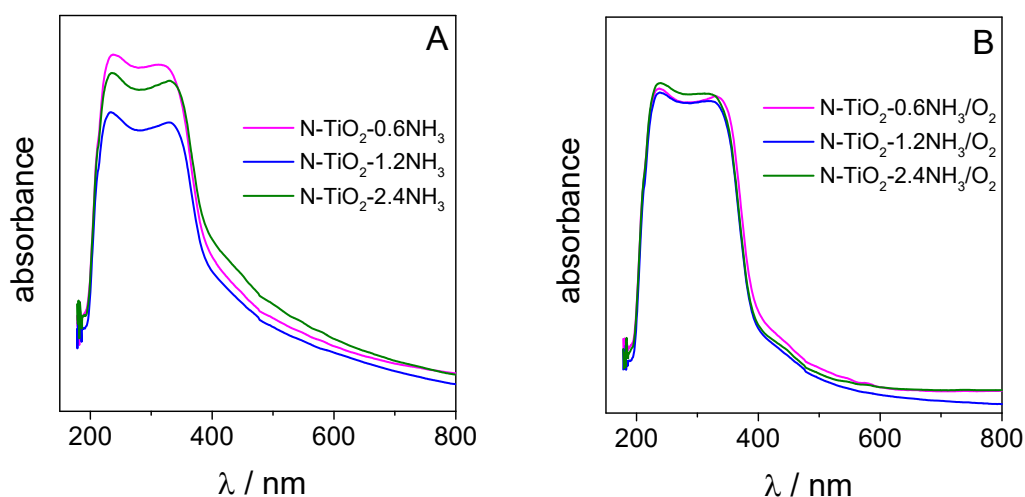


Figure 55. A) UV/vis spectra of am-TiO₂ treated with ammonia at different heating rates (0.6, 1.2, and 2.4 °C/min) and B) UV/vis spectra obtained after a successive treatment with oxygen (450 °C, 2 h).

The effect of the successive oxygen treatment on the photocatalytic activity has been also investigated. The photocatalytic activities of the samples at irradiation under white light (Figure 56A) were in the order of N-TiO₂-1.2-O₂ > N-TiO₂-0.6-O₂ ~ N-TiO₂-2.4-O₂ > TiO₂-Ar/O₂. According to results presented in Figure 56B, photocatalytic activities of the samples under visible light irradiation were in the order of N-TiO₂-1.2-O₂ > N-TiO₂-0.6-O₂ ~ TiO₂-Ar/O₂ > N-TiO₂-2.4-O₂.

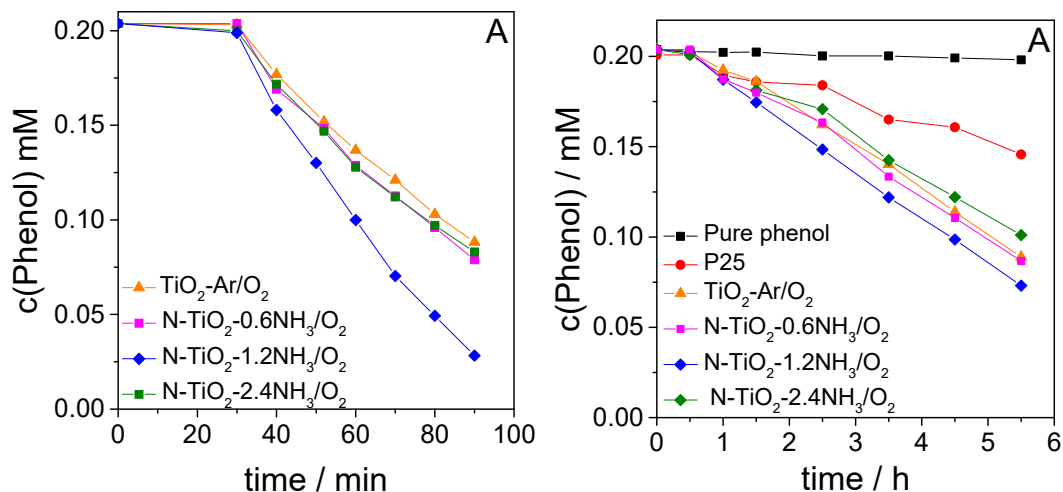


Figure 56. Degradation of phenol as function of time under Xenon lamp irradiation for samples obtained using different heating rates (0.6, 1.2, and 2.4 °C/min) under NH_3 atmosphere followed from successive treatment under oxygen (450 °C, 2 h); A) white light and B) visible light $\lambda > 420 \text{ nm}$.

3.3.3 Influence of the presence of water vapor

Finally, the influence of water vapor on the structural features and photocatalytic activity of nitrogen-doped mesoporous TiO_2 was studied. For that reason, the am- TiO_2 material was heated in a gas mixture containing NH_3 , N_2 , and water vapor. The samples obtained at different heating temperatures were assigned N- TiO_2 -200 $\text{NH}_3/\text{N}_2/\text{H}_2\text{O}$, N- TiO_2 -350 $\text{NH}_3/\text{N}_2/\text{H}_2\text{O}$ and N- TiO_2 -450 $\text{NH}_3/\text{N}_2/\text{H}_2\text{O}$, respectively.

XRD patterns of the samples synthesized in presence of water vapor are shown in Figure 57A. It can be seen from that Figure that the sample N- TiO_2 -200 $\text{NH}_3/\text{N}_2/\text{H}_2\text{O}$ contains already crystalline anatase domains. At absence of water vapor crystalline anatase domains were not obtained at such low temperature. With increasing the heating temperature from 350 to 450°C, the intensity of the anatase phase reflexes increases and the reflexes become narrower. Again, the XRD patterns did not show any nitrogen containing phase. Moreover, reflexes of the β - TiO_2 phase were also not observed. This indicates to that the presence of water vapor has a strong influence on the crystallization of the titania. Mean crystallite sizes in presence the water vapor (Table 11) where obvious higher than those sizes obtained in absence of water vapor and increases with increasing temperature.

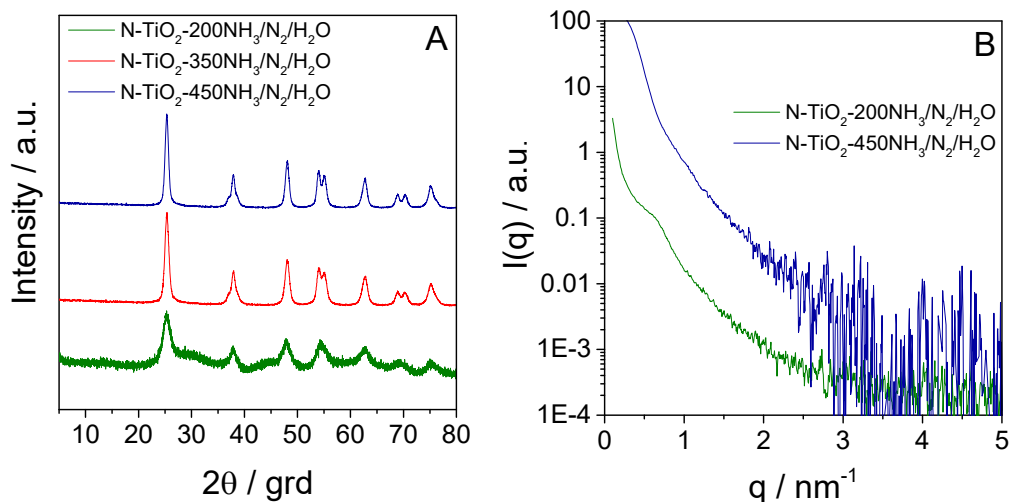


Figure 57A) XRD patterns and B) SAXS patterns of the am-TiO₂ after heating the sample under gas mixture of NH₃, N₂, and water vapor.

SAXS patterns for the samples prepared at 200 or 450 °C are presented in Figure 57B. The pattern shows that the material lost the mesoporous order already after heating to 200 °C where both amorphous and crystalline domains were present. This indicates that already at 200 °C the structure of amorphous domains are changed by the water vapor. The pattern of the samples prepared at 450 °C show that the ordered structure was completely collapsed. The collapse of the mesoporous ordering is connected with considerable decrease in BET surface area as shown in Table 11.

UV–Visible spectra of N-TiO₂-200NH₃/N₂/H₂O, N-TiO₂-350NH₃/N₂/H₂O and N-TiO₂-450NH₃/N₂/H₂O together with the spectra of m-TiO₂ are shown in Figure 58A. Interestingly, UV/Vis spectra of am-TiO₂ and N-TiO₂-200NH₃/N₂/H₂O are very similar. With increasing temperature the UV intensity is shifted to slightly higher wavelength. Absorption in the visible range is general lower than in the other materials obtained in presence of gaseous ammonia. Also the estimated band gap (Table 11) was generally higher in comparison to the other samples prepared at presence of gaseous ammonia but at absence of water (see Table 9 and Table 10). The high band gap indicates that the amount of nitrogen bounded to the titania surface should be only low.

Table 11. General characteristics for samples heated under a mixture of NH₃, N₂, and water vapor.

Samples	BET m ² /g	V _p cm ³ /g	d _{pore} nm	d _{cryst.} nm	band gap eV
N-TiO ₂ -200NH ₃ /N ₂ /H ₂ O	388	0.73	6.6	-	3.23
N-TiO ₂ -350NH ₃ /N ₂ /H ₂ O	162	0.51	9.1	8.2	3.19
N-TiO ₂ -450NH ₃ /N ₂ /H ₂ O	137	0.51	11.6	9.8	3.20

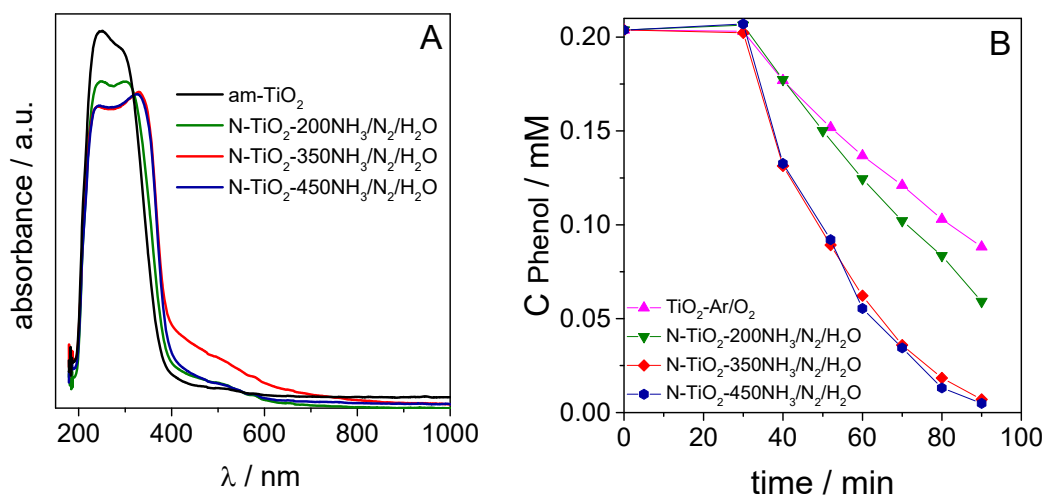


Figure 58. A) UV/Vis spectra and B) phenol degradation of as function of time under Xenon lamp irradiation (white light) for samples heated under mixture of NH₃, N₂, and water vapor.

Because of the assumed low nitrogen content the samples prepared under water vapor were tested in phenol degradation using white light. The results are presented in Figure 58B. It can be seen that all samples prepared in presence of water vapor showed higher photocatalytic activity than that of TiO₂-Ar/O₂. Moreover, activity was clearly higher than photocatalytic activity of the other samples prepared under ammonia atmosphere. This might be due to the effect of H₂O on the surface of TiO₂, which produced defects in the titania structure and formed hydroxyl group or more oxygen vacancies [191]. In addition, the higher crystallinity or lower defect density might be played role in enhanced the photocatalytic activity of materials obtained. This indicates that crystallinity has a larger effect than surface area or mesoporous structure.

XPS spectra of the treated at 450 °C with the NH₃+N₂+H₂O mixture are presented in Figure 59. The Ti 2p_{3/2} region shows after deconvolution signals at 458.1 eV, 460.3 eV, and 461.4 eV. While the the signal at 458.1 eV might be assigned to Ti³⁺ the binding energy of the two signals is very high compared to binding energy given for Ti⁴⁺ [146, 180]. In the O 1s spectra three chemical states of oxygen were separated. The peak at 529.9 eV is characteristic for oxygen in TiO₂. The signal at 532.2 eV might be attributed to surface TiO_x species, OH groups binding with two Ti atoms or C=O. A peak at 532.0 eV was also attributed to a Ti-O-N structure [189]. The largest signal located from at 533.2 eV was previously assigned to surface oxygen in Ti-OH and C-OH. [68]. The high amount of surface Ti-OH species might be also the reason for higher photocatalytic activity of the samples prepared in presence of

water vapor at irradiation with white light in comparison to the activity of samples prepared without water vapor. Furthermore, the samples synthesized with water vapor show also the highest crystallinity. The spectrum in the C 1s region shows two signal with binding energies of 284.8 and 288.1 eV. The broad peak at higher binding energy indicate presence of C=O, O=C-O and C-N bondings on the titania surface. The N 1s region shows after deconvolution peaks located at 399.5 and 401.0 eV which might indicate presence of interstitial and substitutional doped nitrogen.

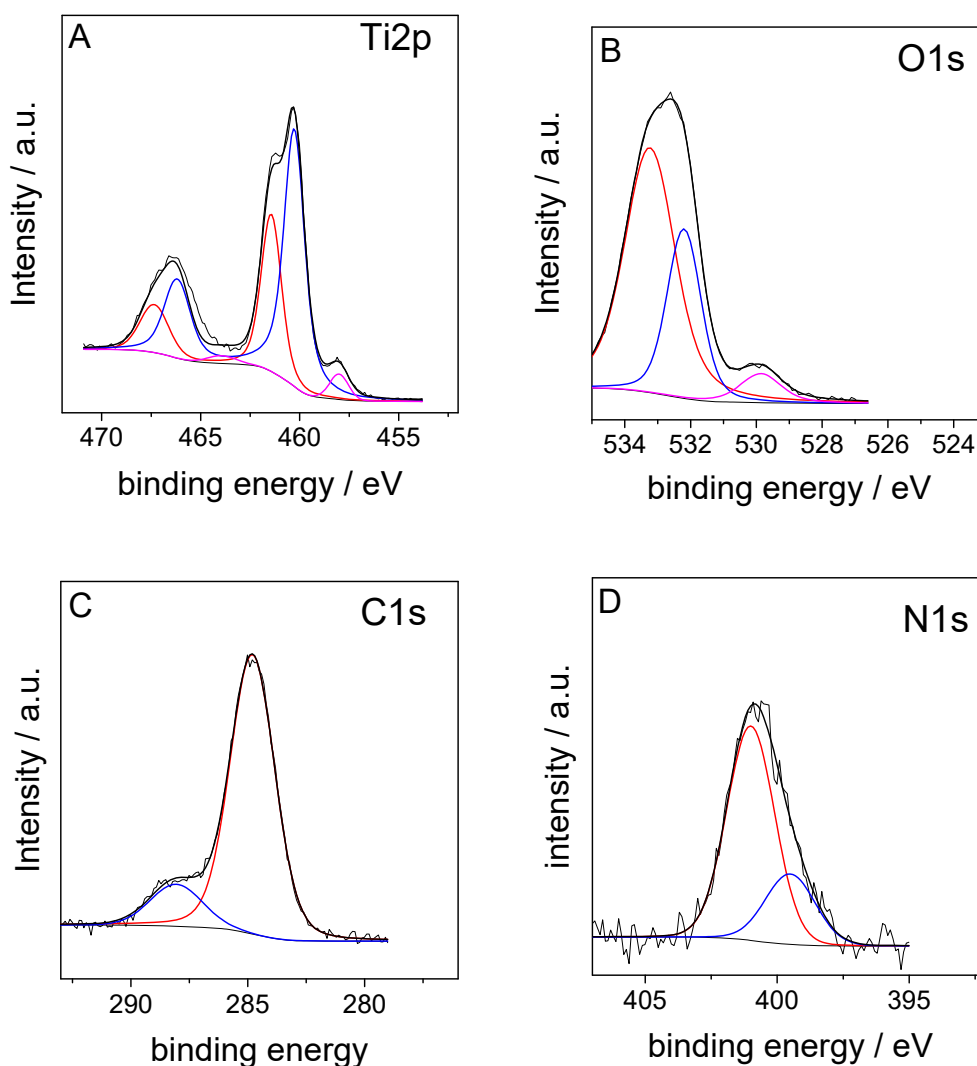


Figure 59. HR XPS spectra from am-TiO₂ after heating in NH₃ /N₂ /H₂O to 450 °C, A) Ti2p, B) O1s, C) C1s, and D) N1s.

4 Summary and Conclusions

First, for pristine ordered mesoporous titania, the characterization results showed that the solvent evaporation, extraction conditions step, the molar molar P123/Ti(OⁱPr)₄ ratio and titanium source play an important role in structural characteristics in the synthesis process of ordered mesoporous titania framework. The temperature of solvent evaporation had affected the structural characteristics of the finally obtained pristine titania after calcination step. Moreover, it was found that the best evaporation temperatures to prepare ordered mesoporous TiO₂ were 40 or 60 °C. In addition, the obtained results form study conditions of removal surfactant indicated that the surfactant extraction step was necessary in order to obtain a titania framework which conserves the hexagonal ordered structure during the thermal induced crystallization. In contrast, two extraction steps seem to be sufficient for removing the surfactant. Extraction temperature should be high as possible to remove the surfactant as far as possible in order to avoid collapse of the ordered mesostructure during the following thermal treatment. The effect of molar P123/Ti(OⁱPr)₄ ratio indicted that the high molar ratio leads to collapse of ordered mesoporous TiO₂. The effect of titanium source on the textural and structural properties of TiO₂ showed that the high order mesoporous structure was obtained by using titanium isopropoxide as titanium source. Based on the effect of the previous parameters, it can be concluded that the best hexagonal ordered mesoporous TiO₂ was obtained with 0.0163 molar P123/ Ti(OⁱPr)₄ ratio, 40 °C evaporation temperature, 2 or 4 times extraction at 78 °C, and 450 °C calcination temperature under Ar for 6.5 h then O₂ for 2 h. Generally, the phase composition of obtained materials has been not influenced by above various parameters. The crystal phase obtained after thermal treatment were mainly anatase TiO₂ together with minor reflections attributed of β-TiO₂.

Moreover, the pristine mesoporous titania showed high catalytic activity for photodegradation of phenol under visible light. The reason for that is the presence of carbon and nitrogen, which leads to enhancement of the photocatalytic activity in visible region. The total nitrogen and carbon content was very low. The carbon was assumed to be residuals originating from residuals of the titanium precursor and/or the surfactant. The nitrogen was presented from treatment of gel in ammonia atmosphere. The influence of the structural parameters on photocatalytic activity of phenol degradation is relatively small. There is no correlation between BET surfaces area and degree of ordering.

Second, for the metal (Fe, Co, and Ni)-doped titania, the obtained results showed that ordering of mesoporous titania framework obtained after the thermal induced crystallization is influenced by the amount of added doping metal. For 0.5 mol% Fe, Co and Ni, the hexagonal ordered mesoporous structure successfully observed after titania precipitation was mainly maintained during the crystallization process. The reason for that might be due to the homogenous distribution of metal ions inside the gel formed during solvent evaporation. Moreover, the low content of the doping metal has no obvious effect on the titania crystallization during thermal annealing. This is due to formation of crystallites with nearly identical particle size as obtained in pristine titania. On the other hand, at higher metal content (5 mol%), the synthesis of hexagonal ordered mesoporous titania was influenced by the particular Fe or Co. While for higher Ni content after annealing the same ordered mesoporous structure was obtained as for low Ni content, the sample doped with Co loses their mesoporous ordering during the calcination process. Additional processes like surface segregation might occur during titania crystallization leading to formation of bigger titania crystallites and amorphous doped metal oxide surface structures. The 0.5 mol% Fe, Co and Ni-doped ordered mesoporous TiO₂ showed BET surface areas higher than 5 mol% Fe, Co and Ni-doped ordered mesoporous TiO₂.

Moreover, the photocatalytic activity of the 0.5 mol% Fe, Co and Ni-doped ordered mesoporous TiO₂ showed enhanced phenol degradation under UV light irradiation compared to the pristine TiO₂. In addition, the samples doped with 0.5 mol% Fe and Ni-doped showed also higher photocatalytic activity than the pristine TiO₂ under white light irradiation. These results prove that the doping metal is involved in processes running after generation of the charge carrier by irradiation of the sample with light. The charge carrier might interact both with the doping element itself or defects created in their environment.

All the metal-doped TiO₂ samples and pristine TiO₂ showed higher photoactivity degradation of phenol than P25 under visible light. The reason for this higher photoactivity might be due to the acting of these metals as charge carrier trap. Otherwise, it cannot be excluded that the photocatalytic activity in the visible range is caused by the presence of nitrogen or carbon which were not completely removed during the extraction in boiling ethanol and the following thermal treatment. This assumption would explain also the low differences in photocatalytic activity between the pristine and the metal doped materials when using visible light irradiation ($\lambda > 420$ nm).

Third, for the N-doped titania, the obtained results indicate that the parameters used for titania crystallization have influences on the structural characteristics and the photocatalytic activity. Factors studied were the crystallization temperature, the heating rate, and the influence of water vapor. Moreover, the effect of the successive oxygen treatment has been also explored.

The temperature applied for titania crystallization has a strong influence on the mesoporous ordering. The presence of hexagonal ordered mesoporous domains in at crystallization at 450 °C was confirmed by SAXS and STEM-HAADF. Moreover, the EELS spectrum indicates that the nitrogen was located mainly on the surface of titania when heating the sample in ammonia. XPS analysis showed the presence of interstitial nitrogen doping (TiO_2N_x) and substitutional nitrogen doping ($\text{TiO}_{2-x}\text{N}_x$). Higher crystallization temperature (550 °C) led to a loss of the mesoporous ordering. On the other hand, the titania crystallinity was increasing with raising heating temperature.

The successive treatment in oxygen led to a loss of mesoporous ordering independent which temperature was used for crystallization under ammonia. This indicates that the treatment with oxygen has a larger effect on ordering of the mesoporous structure as the presence of ammonia. BET surface area decreased when the material was successive treated in oxygen. This suggests that pores walls were lost during the oxygen treatment although the mean pore size does not increase strongly. The photocatalytic results obtained under irradiation with white or visible light after successive oxygen treatment showed higher photocatalytic activity for the sample prepared at 450 °C under ammonia than the samples prepared at 350 or 450 °C. It was assumed that interstitial nitrogen led to formation of oxygen vacancies in the structure.

The effect of the heating rates (0.6, 1.2, and 2.4 °C/min) under ammonia atmosphere on the structural characteristics and photocatalytic activity were also investigated. The ordered mesoporous structure, crystal phase and crystallite size were approximately independent of the heating rate. After a successive oxygen treatment, a strong loss of mesoporous ordering was found when the material was prepared at heating rate of 0.6 and 2.4 °C/min under ammonia atmosphere. Again, BET surface area decreased when the material was successive treated with oxygen. Moreover, it was found that the heating rate has approximately no influence on the light absorption in the visible range when the samples were treated with gaseous ammonia. This might be considered as indication that the amount of nitrogen bound to the titania surface does not depend on the applied heating rate. The photocatalytic results

obtained under irradiation with white or visible light showed the highest photocatalytic activity for the sample prepared under ammonia with a heating rate of 1.2 °C/min. The reason the higher photocatalytic activity of this sample is still unclear.

The effect of presence of water vapor on the structural characteristics of N-doped TiO₂ has been investigated via different heating temperatures (200, 350, and 450 °C). The presence of water vapor had a strong influence on the crystallization of the titania phase. Here, crystalline anatase domains were already obtained after treatment at 200 °C. Moreover, increasing crystallite size was found with increasing heating temperature. In addition, the presence of water vapor had a strong influence on the ordering of the mesoporous structure. It has been found that already for the sample heated at 200 °C the ordered mesoporous structure was nearly collapsed. The collapse of the mesoporous ordering is connected with a considerable decrease in BET surface area. The photocatalytic activity of the crystallized samples prepared under presence of water vapor at irradiation with white light was higher than activity of samples prepared under ammonia and successive oxygen treatment. This might be due to the effect of H₂O on the surface of titania, which produced hydroxyl groups. Another reason for the observed effect might be the higher crystallinity connected with a lower defect density.

5 Appendix

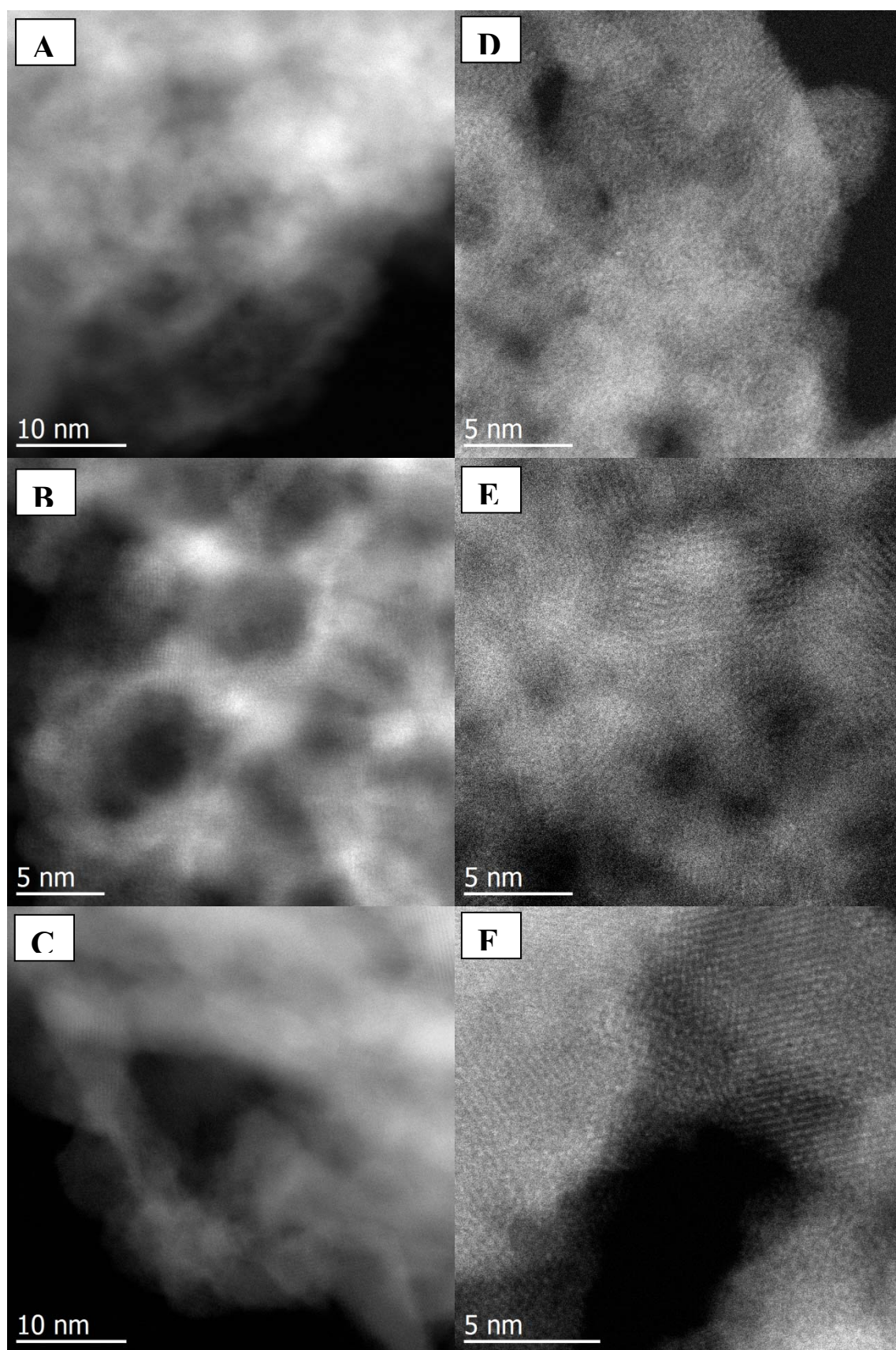
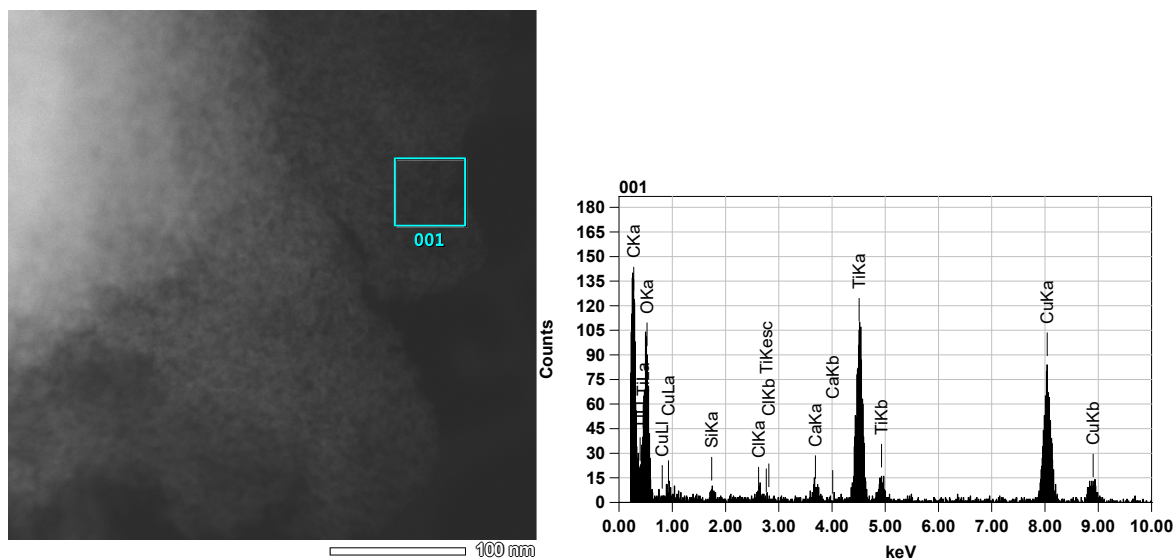
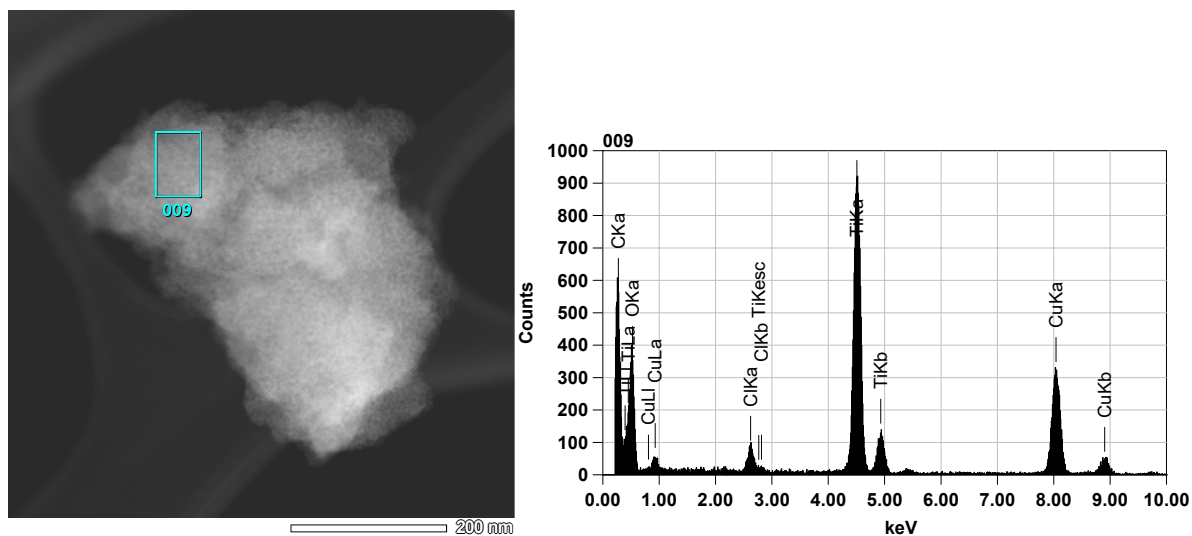


Figure A1. STEM-HAADF images of the material were the solvent was evaporated at 40 °C (A,B,C) and 70 °C (D,E,F); (A,D) after treatment with ammonia, (B,E) after surfactant extraction, and (C,F) after calcination.



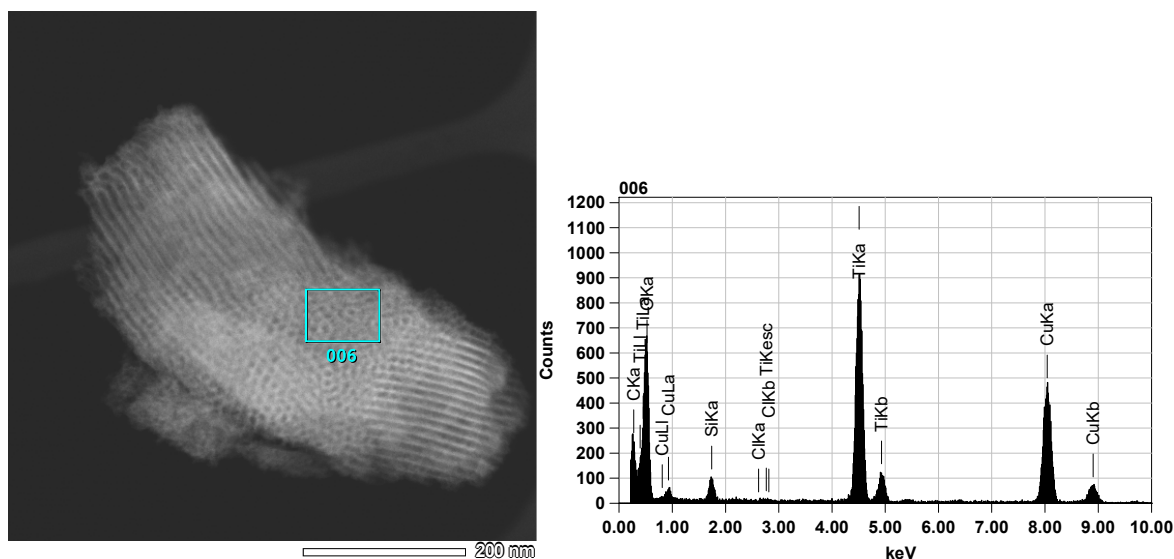


Figure A4. STEM-HAADF image of the sample synthesized with solvent evaporation temperature of 40 °C after surfactant removal in boiling ethanol – (left) and the EDX spectra of the marked area – (right) (the sample was deposited on Cu-grid).

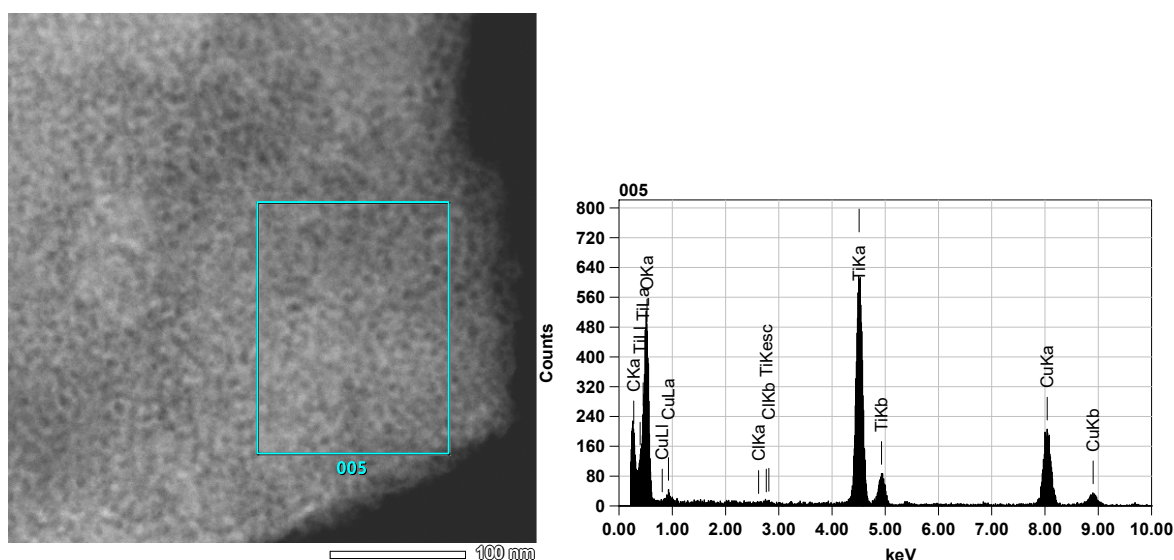


Figure A5. STEM-HAADF image of the sample synthesized with solvent evaporation temperature of 70 °C after surfactant removal in boiling ethanol – (left) and the EDX spectra of the marked area – (right) (the sample was deposited on Cu-grid).

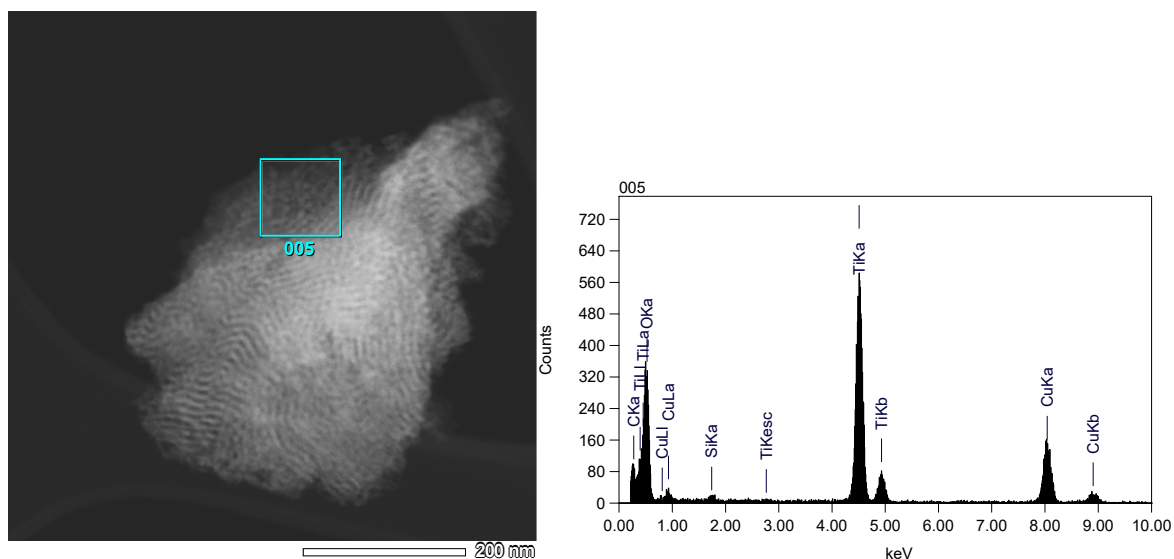


Figure A6. STEM-HAADF image of the sample synthesized with solvent evaporation temperature of 40 °C after thermal treatment at 450 °C – (left) and the EDX spectra of the marked area – (right) (the sample was deposited on Cu-grid).

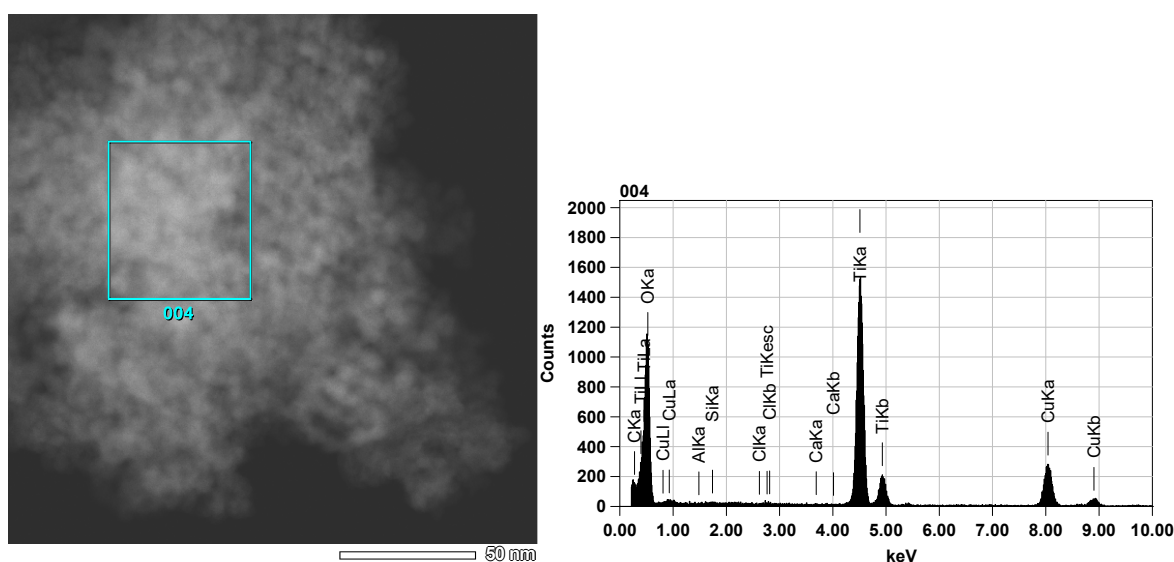


Figure A7. STEM-HAADF image of the sample synthesized with solvent evaporation temperature of 70 °C after thermal treatment at 450 °C – (left) and the EDX spectra of the marked area – (right) (the sample was deposited on Cu-grid).

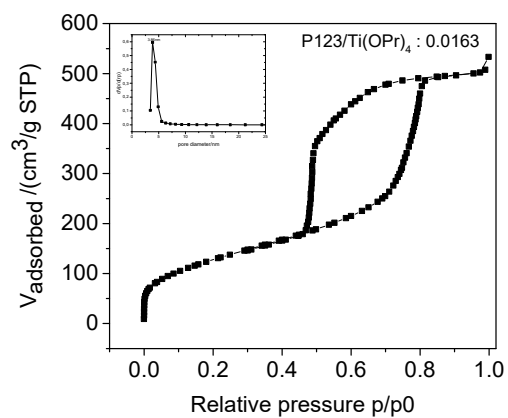


Figure A8. Nitrogen adsorption–desorption isotherm and the corresponding BJH pore size distribution (inset) of the sample synthesized with solvent evaporation temperature of 40 °C after surfactant extraction.

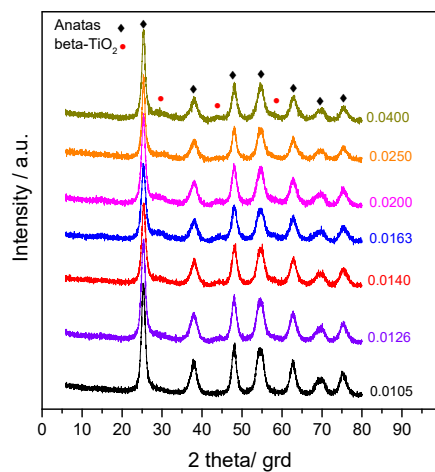


Figure A9. XRD patterns of TiO₂ prepared with different molar P123/Ti(OiPr)₄ ratios in 5.4 M of HCl at 40 °C, after calcination.

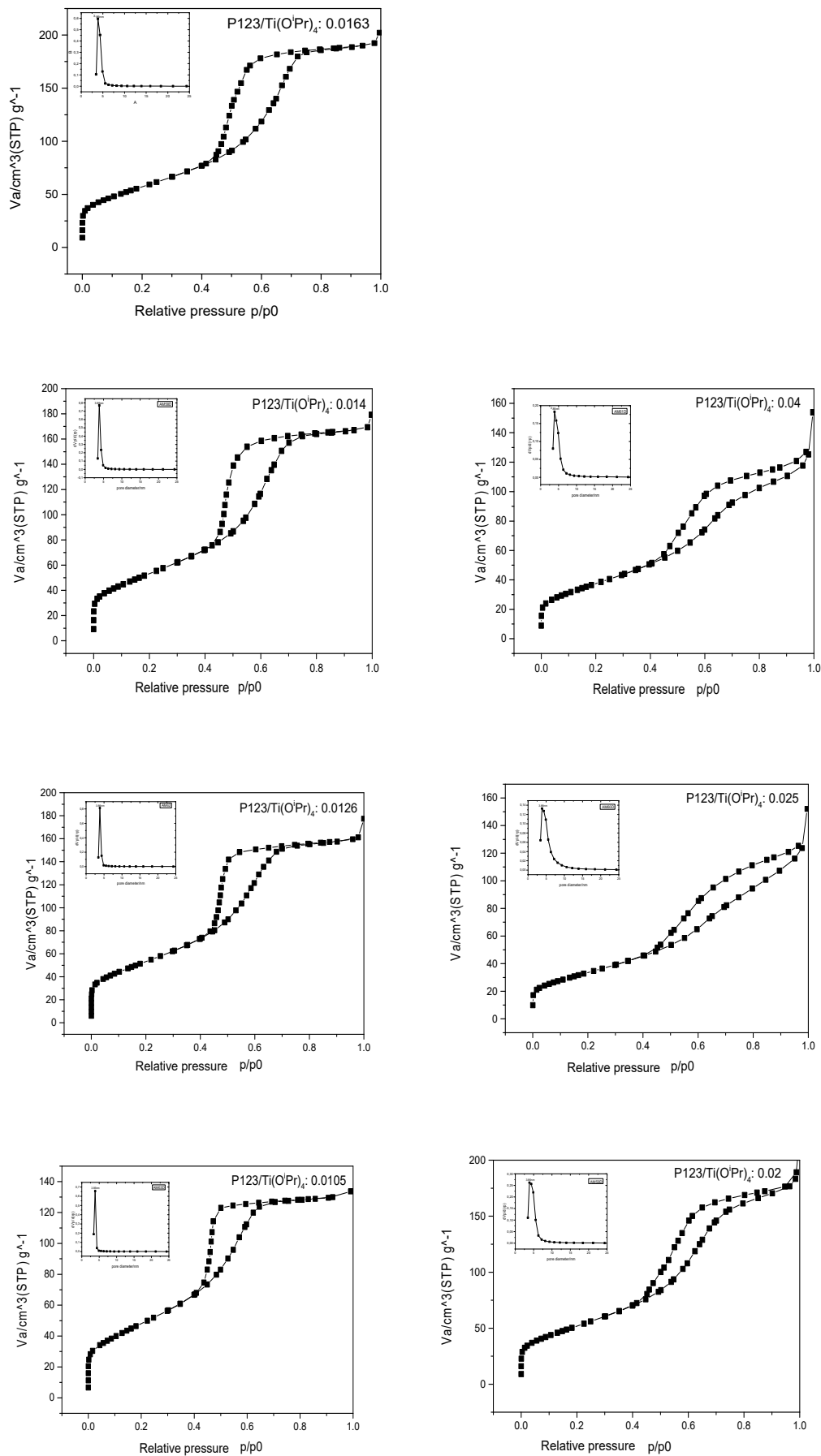


Figure A10. Nitrogen adsorption –desorption isotherms and the corresponding BJH pore size distributions for different molar P123/Ti(O'Pr)₄ ratio.

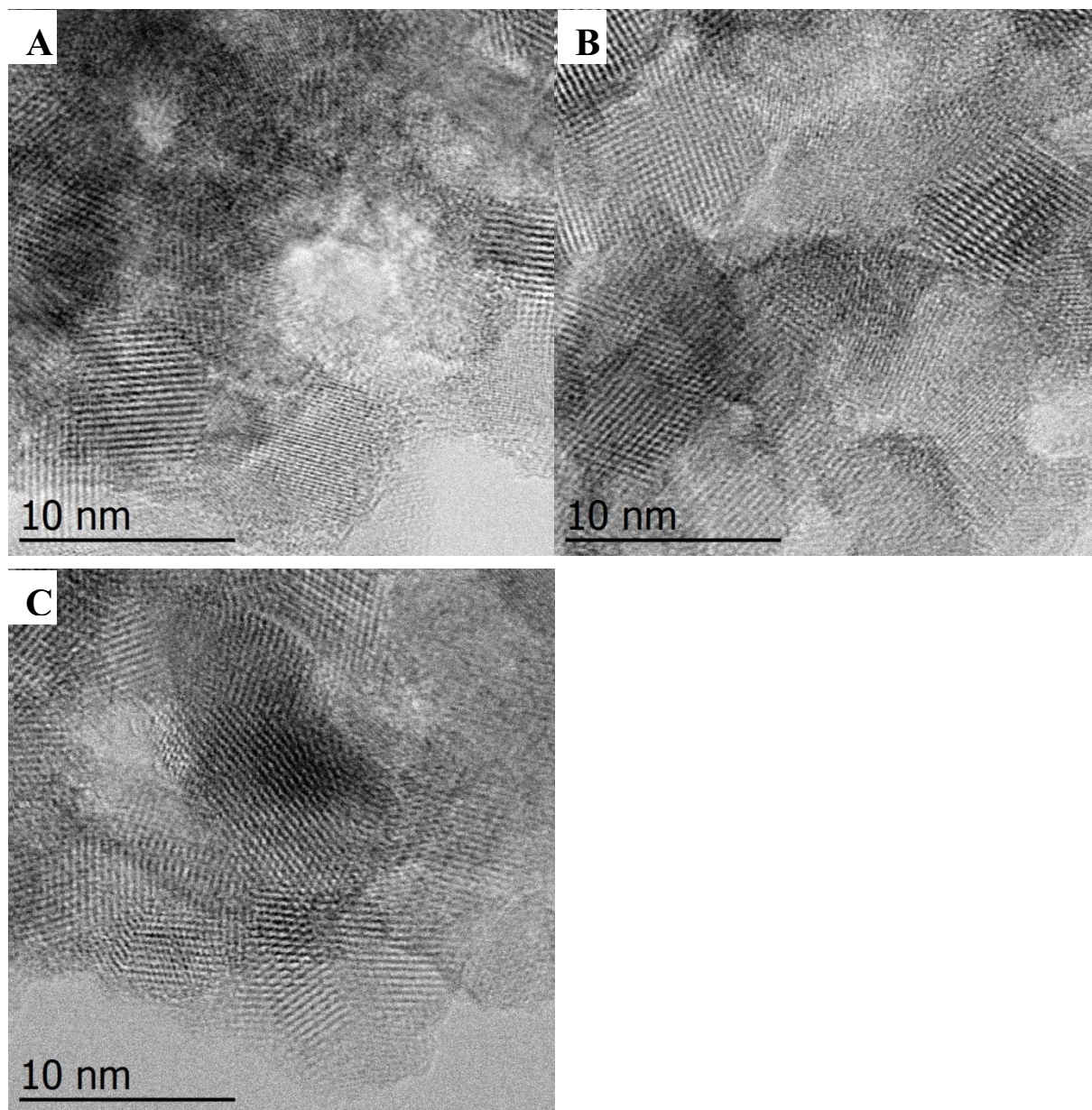


Figure A11. High resolution STEM ABF images of doped titania samples obtained after thermal treatment A) doped with 0.5 mol% Fe, B) doped with 0.5 mol% Co, C) doped with 0.5 mol% Ni, (to see better the lattice planes STEM ABF was applied because of the higher depth of the focus compared to STEM HAADF).

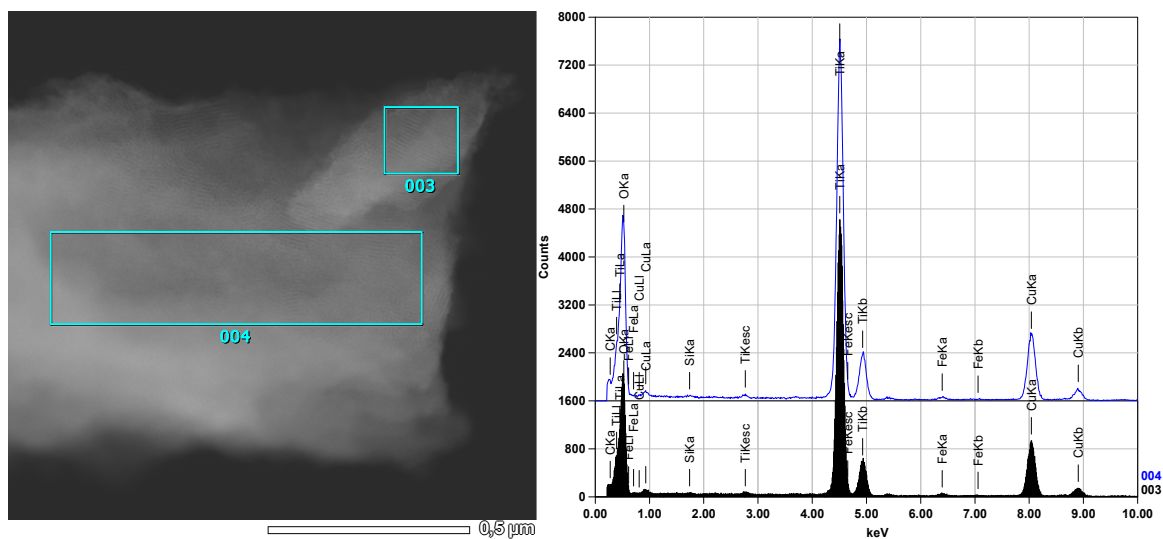


Figure A12. EDX spectra of the sample doped with 0.5 mol% Fe at two different areas.

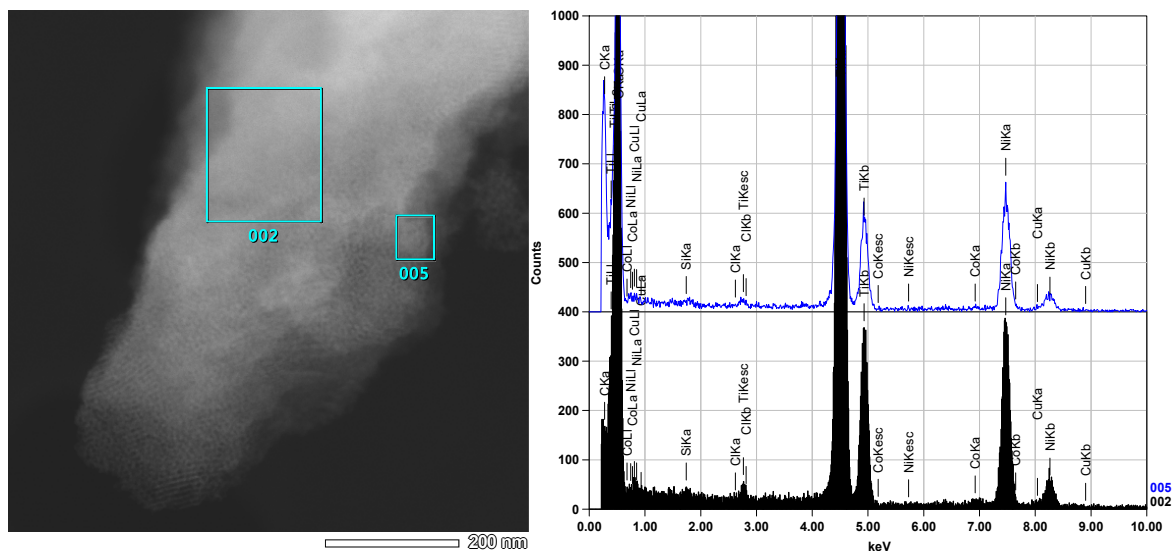


Figure A13. EDX spectra of the sample doped with 0.5 mol% Co at two different areas.

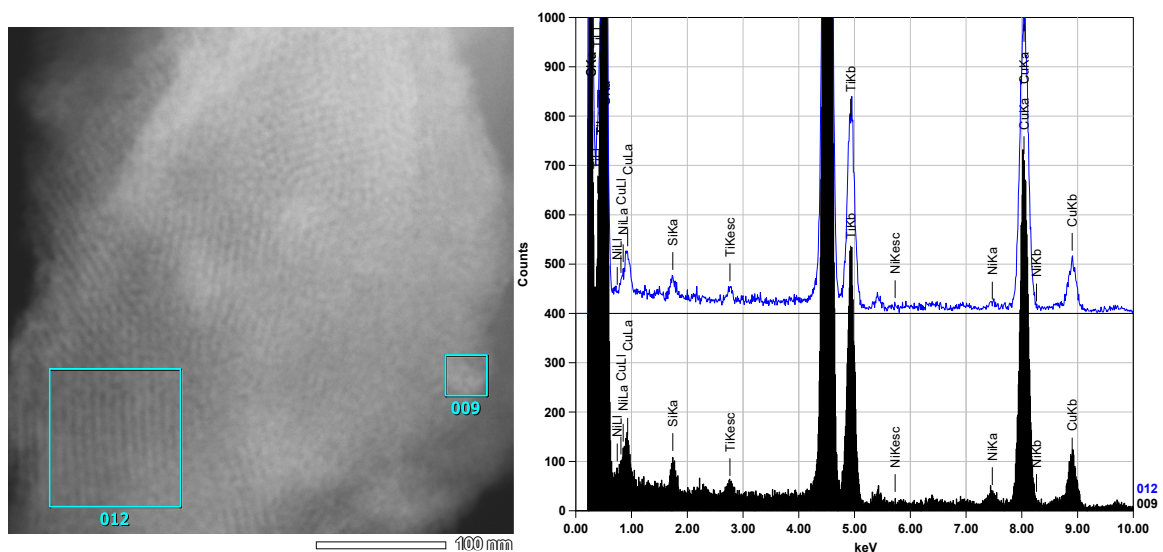


Figure A14. EDX spectra of the sample doped with 0.5 mol% Ni at two different areas.

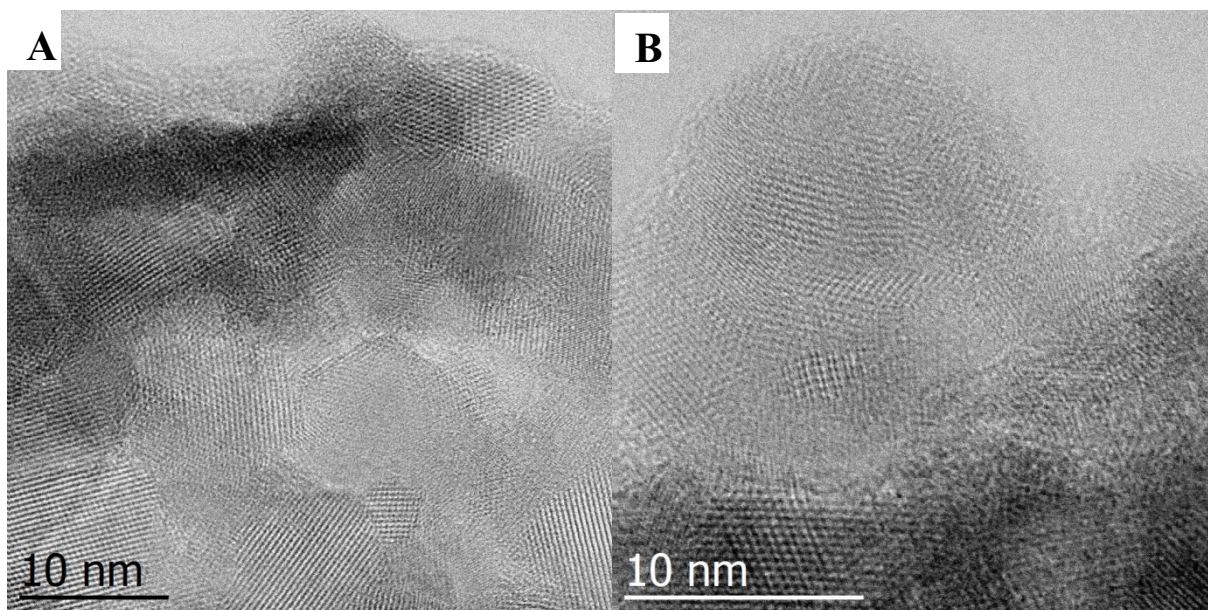


Figure A15. High resolution STEM ABF images of doped titania samples obtained after thermal treatment, A) doped with 5 mol% Fe, B) doped with 5 mol% Ni (to see better the lattice planes STEM ABF was applied because of the higher depth of the focus compared to STEM HAADF).

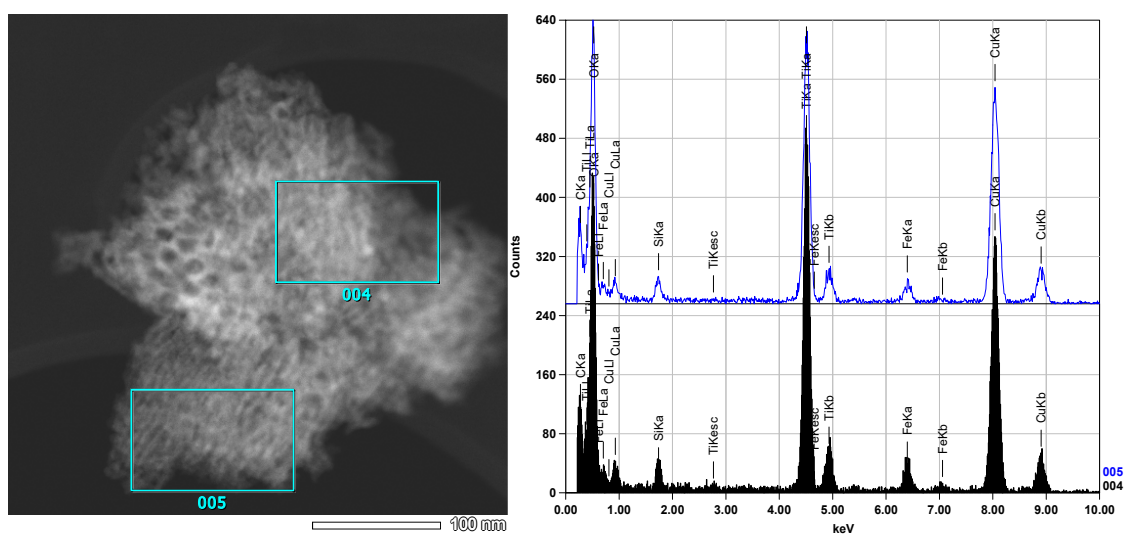


Figure A16. EDX spectra of the sample doped with 5 mol% Fe at two different areas; area (004) Ti/Fe= 12.0/88.0 wt%, area (005) Ti/Fe= 9.5/90.5 wt%.

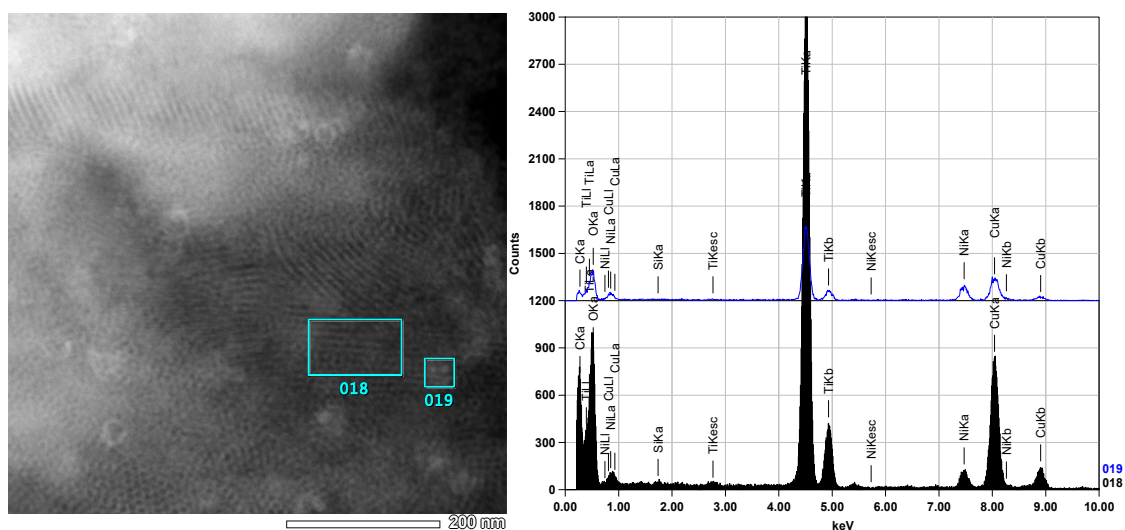


Figure A17. EDX spectra of the sample doped with 5 mol% Ni at two different areas; area (018) Ti/Ni= 93.3/6.1 wt%, area (019) Ti/Ni= 74.2/25.8 wt% (larger NiO nanoparticle was included).

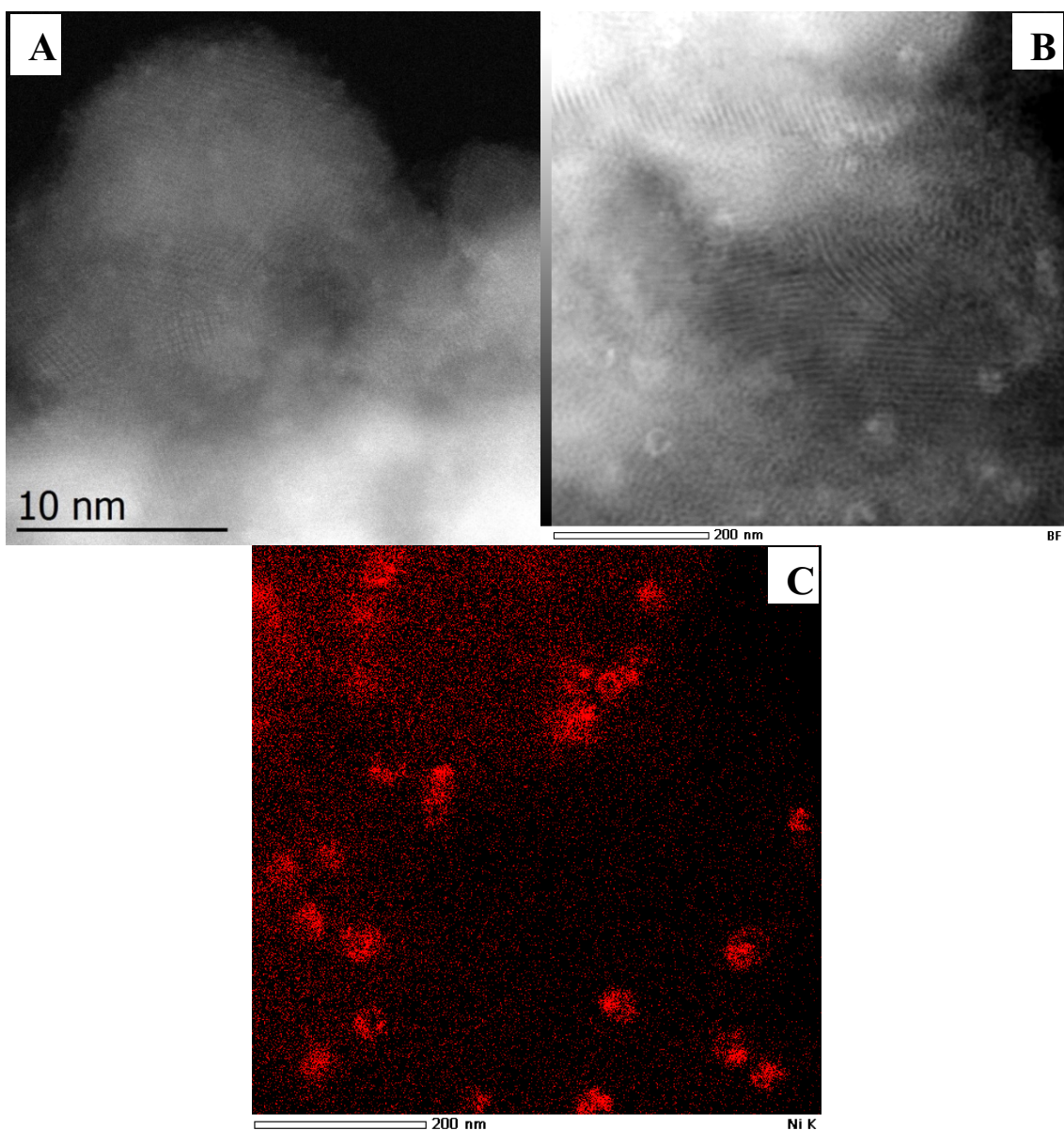


Figure A18. HAADF STEM images of the sample prepared with 5 mol% Ni in different magnification (A and B) and results of EDX mapping using the NiK α line (C).

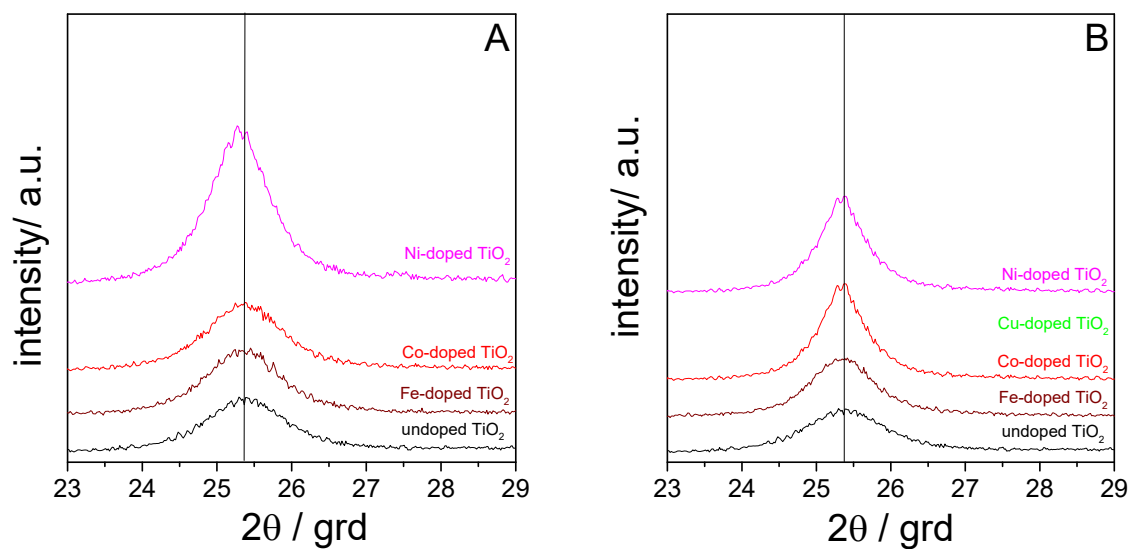


Figure A19. Comparison of the position of the 002 reflexes of anatase in calcined samples doped with A) 0.5 mol% and B) 5 mol%.

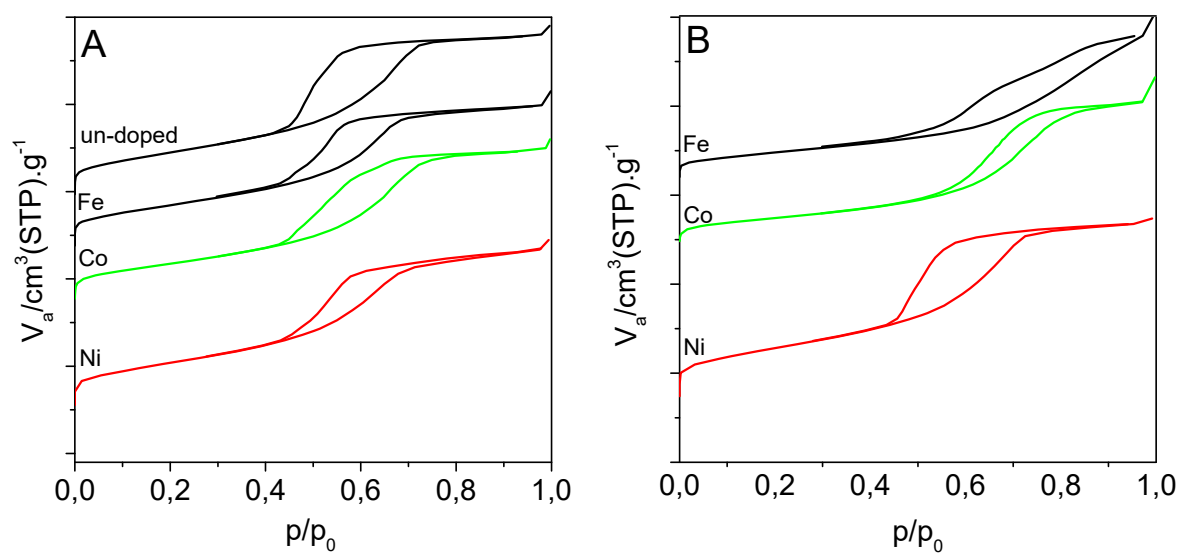


Figure A20. Adsorption-desorption isotherms for calcined materials synthesized with - A) 0.5 mol% metal and B) 5 mol% metal.

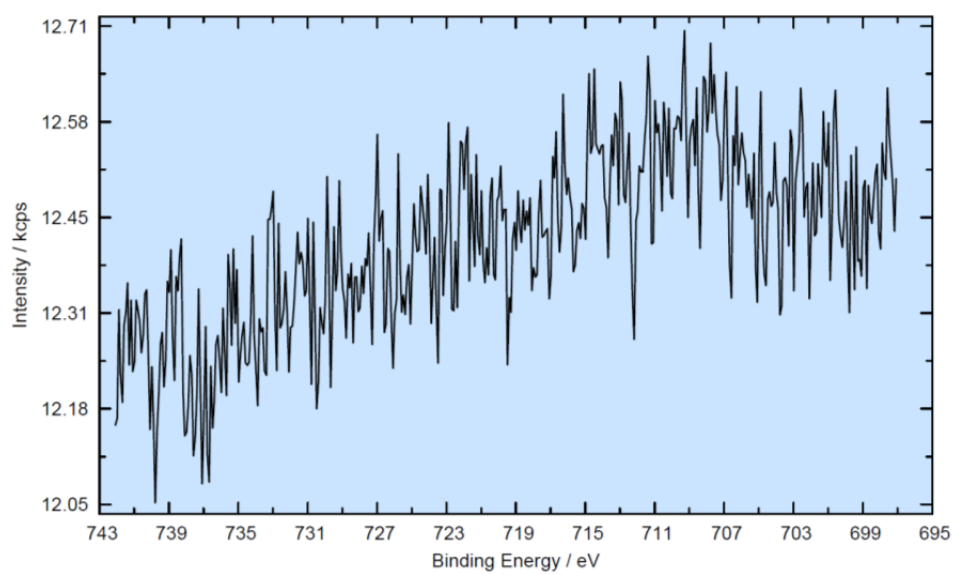


Figure A21. XPS spectra of the Fe2p_{3/2} region for the sample doped with 0.5 mol% Fe

6 References

- [1] X. Chen, S.S. Mao, *Chem. Rev.*, 107 (2007) 2891-2959.
- [2] R. Zhang, A.A. Elzatahry, S.S. Al-Deyab, D. Zhao, *Nano Today*, 7 (2012) 344-366.
- [3] A.A. Ismail, D.W. Bahnemann, *J. Mater. Chem.*, 21 (2011) 11686-11707.
- [4] J. Peral, X. Domenech, D.F. Ollis, *J. Chem. Technol. Biotechnol.*, 70 (1997) 117-140.
- [5] R.J. Tayade, R.G. Kulkarni, R.V. Jasra, *Ind. Eng. Chem. Res.*, 45 (2006) 5231-5238.
- [6] D. Kanakaraju, B.D. Glass, M. Oelgemöller, *Env. Chem. Lett.*, 12 (2014) 27-47.
- [7] P. Dzik, M. Veselý, M. Kete, E. Pavlica, U.k.L.i. Štangar, M. Neumann-Spallart, *ACS App. Mat. Int.*, 7 (2015) 16177-16190.
- [8] W.-N. Zhao, Z.-P. Liu, *Chem. Sci.*, 5 (2014) 2256-2264.
- [9] K. Nakata, A. Fujishima, *J. Photochem. Photobiol., C*, 13 (2012) 169-189.
- [10] T.L. Thompson, J.T. Yates, *Chem. Rev.*, 106 (2006) 4428-4453.
- [11] A. Fujishima, T.N. Rao, D.A. Tryk, *J. Photochem. Photobiol., C*, 1 (2000) 1-21.
- [12] T. Wang, X. Meng, P. Li, S. Ouyang, K. Chang, G. Liu, Z. Mei, J. Ye, *Nano Energy*, 9 (2014) 50-60.
- [13] V. Binas, D. Venieri, D. Kotzias, G. Kiriakidis, *Journal of Materiomics*, 3 (2017) 3-16.
- [14] J. Schneider, M. Matsuoka, M. Takeuchi, J. Zhang, Y. Horiuchi, M. Anpo, D.W. Bahnemann, *Chem. Rev.*, 114 (2014) 9919-9986.
- [15] S. Mugundan, B. Rajamannan, G. Viruthagiri, N. Shanmugam, R. Gobi, P. Praveen, *Appl. Nanosci.*, 5 (2015) 449-456.
- [16] A. Fujishima, K. Honda, *Nature*, 238 (1972) 37.
- [17] M.R.D. Khaki, M.S. Shafeeyan, A.A.A. Raman, W.M.A.W. Daud, *J. Environ. Manage.*, 198 (2017) 78-94.
- [18] Z. Liu, Y.G. Andreev, A.R. Armstrong, S. Brutti, Y. Ren, P.G. Bruce, *Prog. Mater Sci.:Mat. Intern.*, 23 (2013) 235-244.
- [19] Y. Li, X. Sun, H. Li, S. Wang, Y. Wei, *Powder Technol.*, 194 (2009) 149-152.
- [20] A.A. Gribb, J.F. Banfield, *Am. Mineral.*, 82 (1997) 717-728.
- [21] S. Bagheri, K. Shameli, S.B. Abd Hamid, *J. Chem-NY*, 2013 (2012).
- [22] T. Luttrell, S. Halpegamage, J. Tao, A. Kramer, E. Sutter, M. Batzill, *Scientific Reports*, 4 (2014) 4043.
- [23] L. Zhang, C. Ni, H. Jiu, H. Chen, G. Qi, *J. Mater. Sci-Mater. El.*, 28 (2017) 6601-6606.
- [24] J.L. Vivero-Escoto, Y.-D. Chiang, K.C. Wu, Y. Yamauchi, *Sci. Technol. Adv. Mat.*, 13 (2012) 013003.
- [25] T. Hongo, A. Yamazaki, *Micropor. Mesopor. Mat.*, 142 (2011) 316-321.

- [26] B. Elgh, N. Yuan, H.S. Cho, D. Magerl, M. Philipp, S.V. Roth, K.B. Yoon, P. Müller-Buschbaum, O. Terasaki, A.E. Palmqvist, *APL Materials*, 2 (2014) 113313.
- [27] H. Shibata, T. Ogura, T. Mukai, T. Ohkubo, H. Sakai, M. Abe, *J. Am. Chem. Soc.*, 127 (2005) 16396-16397.
- [28] C.-W. Wu, T. Ohsuna, M. Kuwabara, K. Kuroda, *J. Am. Chem. Soc.*, 128 (2006) 4544-4545.
- [29] D. Grosso, G. de AA Soler-Illia, F. Babonneau, C. Sanchez, P.A. Albouy, A. Brunet-Bruneau, A.R. Balkenende, *Adv. Mater.*, 13 (2001) 1085-1090.
- [30] B. Smarsly, D. Grosso, T. Brezesinski, N. Pinna, C. Boissière, M. Antonietti, C. Sanchez, *Chem. Mater.*, 16 (2004) 2948-2952.
- [31] Y. Bian, X. Wang, Z. Zeng, Z. Hu, *Surf. Interface Anal.*, 45 (2013) 1317-1322.
- [32] R. Keshavarzi, V. Mirkhani, M. Moghadam, S. Tangestaninejad, I. Mohammadpoor-Baltork, *J. Mater. Chem. A*, 3 (2015) 2294-2304.
- [33] M.E. Davis, *Nature*, 417 (2002) 813.
- [34] W. Li, Z. Wu, J. Wang, A.A. Elzatahry, D. Zhao, *Chem. Mater.*, 26 (2013) 287-298.
- [35] P. Müller, *Pure Appl. Chem*, 31 (1972) 578.
- [36] W. Zhou, H. Fu, *ChemCatChem*, 5 (2013) 885-894.
- [37] J. Ebelman, M. Bouquet, *Ann. Chim. Phys.*, 17 (1846) 54-73.
- [38] C.B. Carter, M.G. Norton, *Ceramic materials: science and engineering*, Springer Science & Business Media, 2007.
- [39] S. Gupta, M. Tripathi, *Open Chemistry*, 10 (2012) 279-294.
- [40] Q. Yin, J. Xiang, X. Wang, X. Guo, T. Zhang, *J. Exp. Nanosci.*, 11 (2016) 1127-1137.
- [41] L. Mahoney, R.T. Koodali, *Materials*, 7 (2014) 2697-2746.
- [42] S. Bagheri, Z.A.M. Hir, A.T. Yousefi, S.B.A. Hamid, *Micropor. Mesopor. Mat.*, 218 (2015) 206-222.
- [43] T. Kimura, *The Chemical Record*, 16 (2016) 445-457.
- [44] J. Tao, Y. Shen, F. Gu, J. Zhu, J. Zhang, *J. Mater. Sci. Technol.*, 23 (2007) 513-516.
- [45] T. Benkacem, N. Agoudjil, *Am J Appl Sci*, 5 (2008) 1437-1441.
- [46] J. Blanchard, M. In, B. Schaudel, C. Sanchez, *Eur. J. Inorg. Chem.*, 1998 (1998) 1115-1127.
- [47] D.M. Antonelli, J.Y. Ying, *Angew. Chem. Int. Ed.*, 34 (1995) 2014-2017.
- [48] I. Kartini, P. Meredith, J.D. Da Costa, G. Lu, *J. Sol-Gel Sci. Technol.*, 31 (2004) 185-189.
- [49] S. Yuan, Q. Sheng, J. Zhang, F. Chen, M. Anpo, *Mater. Lett.*, 58 (2004) 2757-2760.

- [50] N. Tanasković, Ž. Radovanović, V. Đokić, J. Krstić, S. Drmanić, D. Janačković, R. Petrović, *Superlattices Microstruct.*, 46 (2009) 217-222.
- [51] M.V. Swapna, K.R. Haridas, *J. Exp. Nanosci.*, 11 (2016) 540-549.
- [52] S.C. Zi, S. Chandren, L.S. Yuan, R. Razali, C.S. Ho, D. Hartanto, T.M.I. Mahlia, H. Nur, *Solid State Sciences*, 52 (2016) 83-91.
- [53] R. Ameta, S.C. Ameta, *Photocatalysis: Principles and Applications*, CRC Press, 2016.
- [54] S.Z. Islam, S. Nagpure, D.Y. Kim, S.E. Rankin, *Inorganics*, 5 (2017) 15.
- [55] H. Zhang, C. Liang, J. Liu, Z. Tian, G. Wang, W. Cai, *Langmuir*, 28 (2012) 3938-3944.
- [56] C. Dette, M.A. Pérez-Osorio, C.S. Kley, P. Punke, C.E. Patrick, P. Jacobson, F. Giustino, S.J. Jung, K. Kern, *Nano Lett.*, 14 (2014) 6533-6538.
- [57] R. Daghrir, P. Drogui, D. Robert, *Ind. Eng. Chem. Res.*, 52 (2013) 3581-3599.
- [58] A. Zaleska, *Recent Patents on Engineering*, 2 (2008) 157-164.
- [59] M. Zhou, J. Yu, B. Cheng, H. Yu, *Mater. Chem. Phys.*, 93 (2005) 159-163.
- [60] J. Zhu, F. Chen, J. Zhang, H. Chen, M. Anpo, *J. Photochem. Photobiol., A*, 180 (2006) 196-204.
- [61] J. Zhu, J. Ren, Y. Huo, Z. Bian, H. Li, *J. Phys. Chem. C*, 111 (2007) 18965-18969.
- [62] S. TANG, J. HE, Z. ZHANG, *J. Chin. Ceram. Soc.*, 40 (2012) 950-956.
- [63] P. Goswami, J.N. Ganguli, *Mater. Res. Bull.*, 47 (2012) 2077-2084.
- [64] M. Piumetti, F.S. Freyria, M. Armandi, F. Geobaldo, E. Garrone, B. Bonelli, *Catal. Today*, 227 (2014) 71-79.
- [65] Y. Wang, W. Duan, B. Liu, X. Chen, F. Yang, J. Guo, *J. Nanomater.*, 2014 (2014) 63.
- [66] C.W. Soo, J.C. Juan, C.W. Lai, S.B.A. Hamid, R.M. Yusop, *J. Taiwan Inst. Chem. Eng.*, (2016).
- [67] N.M. Nursam, J.Z. Tan, X. Wang, W. Li, F. Xia, R.A. Caruso, *ChemistrySelect*, 1 (2016) 4868-4878.
- [68] P. Mazierski, M. Nischk, M. Gołkowska, W. Lisowski, M. Gazda, M.J. Winiarski, T. Klimczuk, A. Zaleska-Medynska, *Appl. Catal., B*, 196 (2016) 77-88.
- [69] S. Sato, *Chem. Phys. Lett.*, 123 (1986) 126-128.
- [70] S.A. Ansari, M.M. Khan, M.O. Ansari, M.H. Cho, *New J. Chem.*, 40 (2016) 3000-3009.
- [71] F. Huang, A. Yan, H. Zhao, *Influences of Doping on Photocatalytic Properties of TiO₂ Photocatalyst*, *Semiconductor Photocatalysis-Materials, Mechanisms and Applications*, InTech, 2016.
- [72] R. Asahi, T. Morikawa, H. Irie, T. Ohwaki, *Chem. Rev.*, 114 (2014) 9824-9852.

- [73] A. Kachina, E. Puzenat, S. Ould-Chikh, C. Geantet, P. Delichere, P. Afanasiev, *Chem. Mater.*, 24 (2012) 636-642.
- [74] F. Spadavecchia, M. Ceotto, L.L. Presti, C. Aieta, I. Biraghi, D. Meroni, S. Ardizzone, G. Cappelletti, *Chin. J. Chem.* 32 (2014) 1195-1213.
- [75] C.W. Dunnill, I.P. Parkin, *Dalton Transactions*, 40 (2011) 1635-1640.
- [76] K. Zhang, X. Wang, X. Guo, T. He, Y. Feng, *J. Nanopart. Res.*, 16 (2014) 1-9.
- [77] J. Fang, F. Wang, K. Qian, H. Bao, Z. Jiang, W. Huang, *J. Phys. Chem. C*, 112 (2008) 18150-18156.
- [78] P. Mei, M. Henderson, A. Kassiba, A. Gibaud, *J. Phys. Chem. Solids*, 71 (2010) 1-6.
- [79] H.-L. WANG, X.-H. LIU, *J. Inorg. Mater.*, 29 (2014) 997-1002.
- [80] M. Zalas, *Catal. Today*, 230 (2014) 91-96.
- [81] W.C. Huang, J.-M. Ting, *Ceram. Int.*, 43 (2017) 9992-9997.
- [82] N. Pal, A. Bhaumik, *Adv. Colloid Interface Sci.*, 189 (2013) 21-41.
- [83] S.P. Ghuge, A.K. Saroha, *J. Environ. Manage.*, 211 (2018) 83-102.
- [84] J. Wei, Z. Sun, W. Luo, Y. Li, A.A. Elzatahry, A.M. Al-Enizi, Y. Deng, D. Zhao, *J. Am. Chem. Soc.*, 139 (2017) 1706-1713.
- [85] Q. Xiang, J. Yu, M. Jaroniec, *Chem. Commun.*, 47 (2011) 4532-4534.
- [86] B. Bonelli, S. Esposito, F.S. Freyria, *Mesoporous Titania: Synthesis, Properties and Comparison with Non-Porous Titania*, *Titanium Dioxide*, InTech, 2017.
- [87] G.J.A.A. Soler-Illia, P.C. Angelomé, M.C. Fuertes, D. Grosso, C. Boissiere, *Nanoscale*, 4 (2012) 2549-2566.
- [88] G.J. de AA Soler-Illia, C. Sanchez, *New J. Chem.*, 24 (2000) 493-499.
- [89] K. Zimny, J. Ghanbaja, C. Carteret, M.-J. Stébé, J.-L. Blin, *New J. Chem.*, 34 (2010) 2113-2117.
- [90] K. Zimny, T. Roques-Carmes, C. Carteret, M. Stébé, J. Blin, *J. Phys. Chem. C*, 116 (2012) 6585-6594.
- [91] G.J. de AA Soler-Illia, E. Scolan, A. Louis, P.-A. Albouy, C. Sanchez, *New J. Chem.*, 25 (2001) 156-165.
- [92] G.J.A.A. Soler-Illia, C. Sanchez, *New J. Chem.*, 24 (2000) 493-499.
- [93] L.-H. Kao, T.-C. Hsu, K.-K. Cheng, *Journal of colloid and interface science*, 341 (2010) 359-365.
- [94] S. Cao, Y. Zhao, T. Qu, P. Wang, S. Guan, Y. Xu, F. Rao, Y. Li, A. Chen, T. Iyoda, *RSC Advances*, 6 (2016) 55834-55841.
- [95] J. Veliscek-Carolan, R. Knott, T. Hanley, *J. Phys. Chem. C*, 119 (2015) 7172-7183.

- [96] I.-M. Hung, Y. Wang, L.-T. Lin, C.-F. Huang, *J. Porous Mater.*, 17 (2010) 509-513.
- [97] E.L. Crepaldi, G.J.d.A. Soler-Illia, D. Grosso, F. Cagnol, F. Ribot, C. Sanchez, *J. Am. Chem. Soc.*, 125 (2003) 9770-9786.
- [98] C.J. Brinker, G.W. Scherer, *Sol-gel science: the physics and chemistry of sol-gel processing*, Academic press, 2013.
- [99] H. Khan, D. Berk, *Catal. Lett.*, 144 (2014) 890-904.
- [100] J. Livage, M. Henry, C. Sanchez, *Prog. Solid State Chem.*, 18 (1988) 259-341.
- [101] L. Chen, B. Yao, Y. Cao, K. Fan, *J. Phys. Chem. C*, 111 (2007) 11849-11853.
- [102] M. Henderson, A. Gibaud, J.-F. Bardeau, J. White, *J. Mater. Chem.*, 16 (2006) 2478-2484.
- [103] M.J. Henderson, K. Zimny, J.-L. Blin, N. Delorme, J.-F.o. Bardeau, A. Gibaud, *Langmuir*, 26 (2009) 1124-1129.
- [104] L. Chen, Y.-j. Li, X. Peng, Z.-s. Li, M.-x. Zeng, *Trans. Nonferrous Met. Soc. China*, 24 (2014) 1072-1078.
- [105] R. Zhang, B. Tu, D. Zhao, *Chem. Eur. J.*, 16 (2010) 9977-9981.
- [106] H. Luo, C. Wang, Y. Yan, *Chem. Mater.*, 15 (2003) 3841-3846.
- [107] B. Tian, X. Liu, B. Tu, C. Yu, J. Fan, L. Wang, S. Xie, G.D. Stucky, D. Zhao, *Nature Mat.*, 2 (2003) 159.
- [108] K. Assaker, T. Benamor, L. Michelin, B. Lebeau, C. Marichal, M.-J. Stéb  , J.-L. Blin, *Micropor. Mesopor. Mat.*, 201 (2015) 43-49.
- [109] K. Assaker, C.d. Carteret, B.n.d. Lebeau, C. Marichal, L. Vidal, M.-J. St  b  , J.-L. Blin, *ACS Sustain. Chem. Eng.*, 2 (2013) 120-125.
- [110] J.-L. Blin, M.-J. St  b  , T. Roques-Carmes, *Colloids Surf., A*, 407 (2012) 177-185.
- [111] J.S. Yin, Z.L. Wang, *Adv. Mater.*, 11 (1999) 469-472.
- [112] Y. Wang, Z.-H. Jiang, F.-J. Yang, *Mater. Sci. Eng., B*, 134 (2006) 76-79.
- [113] X.-L. Yuan, J.-L. Zhang, M. Anpo, D.-N. He, *Res. Chem. Intermed.*, 36 (2010) 83-93.
- [114] T. Wang, X. Meng, G. Liu, K. Chang, P. Li, Q. Kang, L. Liu, M. Li, S. Ouyang, J. Ye, *J. Mater. Chem. A*, 3 (2015) 9491-9501.
- [115] S. Sajjad, S.A. Leghari, F. Chen, J. Zhang, *Chem. Eur. J.*, 16 (2010) 13795-13804.
- [116] K. Assaker, C. Carteret, T. Roques-Carmes, J. Ghanbaja, M.-J. St  b  , J.-L. Blin, *New J. Chem.*, 38 (2014) 2081-2089.
- [117] Z. Li, A.A. Haidry, B. Gao, T. Wang, Z. Yao, *Appl. Surf. Sci.*, 412 (2017) 638-647.
- [118] S. Anandan, T. Rao, R. Gopalan, Y. Ikuma, **J. Nanosci. Nanotechnol**, 14 (2014) 3181-3186.

- [119] Z. Li, A.A. Haidry, B. Dong, L. Sun, Q. Fatima, L. Xie, Z. Yao, J. Alloys Compd., 742 (2018) 814-821.
- [120] W.W. Anku, M.A. Mamo, P.P. Govender, Phenolic Compounds in Water: Sources, Reactivity, Toxicity and Treatment Methods, Phenolic Compounds-Natural Sources, Importance and Applications, InTech, 2017.
- [121] J. Plotnikow, Verlag Walter de Gruyter & co., Berlin, 1936.
- [122] M. Umar, H.A. Aziz, Photocatalytic degradation of organic pollutants in water, Organic Pollutants-Monitoring, Risk and Treatment, InTech, 2013.
- [123] J. Kou, C. Lu, J. Wang, Y. Chen, Z. Xu, R.S. Varma, Chem. Rev., 117 (2017) 1445-1514.
- [124] A.E. Machado, K.A. Borges, T.A. Silva, L.M. Santos, M.F. Borges, W.A. Machado, B.P. Caixeta, M.D. França, S.M. Oliveira, A.G. Trovó, Applications of Mesoporous Ordered Semiconductor Materials-Case Study of TiO₂, Solar Radiation Applications, InTech, 2015.
- [125] C.-Y. Wu, K.-J. Tu, J.-P. Deng, Y.-S. Lo, C.-H. Wu, Materials, 10 (2017) 566.
- [126] M. Alvaro, C. Aprile, M. Benitez, E. Carbonell, H. García, J. Phys. Chem. B, 110 (2006) 6661-6665.
- [127] J.A. Torres-Luna, N.R. Sanabria, J.G. Carriazo, Powder Technol., 302 (2016) 254-260.
- [128] S. Ahmed, M. Rasul, W.N. Martens, R. Brown, M. Hashib, Water, Air, Soil Pollut., 215 (2011) 3-29.
- [129] Y.-T. Lin, C.-H. Weng, H.-J. Hsu, Y.-H. Lin, C.-C. Shiesh, Int. J. Photoenergy, 2013 (2013).
- [130] Z. Wang, W. Cai, X. Hong, X. Zhao, F. Xu, C. Cai, Appl. Catal., B, 57 (2005) 223-231.
- [131] Z. Zhang, Z. Huang, X. Cheng, Q. Wang, Y. Chen, P. Dong, X. Zhang, Appl. Surf. Sci., 355 (2015) 45-51.
- [132] P.A. Mangrulkar, S.P. Kamble, M.M. Joshi, J.S. Meshram, N.K. Labhsetwar, S.S. Rayalu, Int. J. Photoenergy, 2012 (2012).
- [133] W. Zhou, F. Sun, K. Pan, G. Tian, B. Jiang, Z. Ren, C. Tian, H. Fu, Adv. Funct. Mater., 21 (2011) 1922-1930.
- [134] A. Alagarasi, P. Rajalakshmi, K. Shanthi, P. Selvam, Catal. Today, (2017).
- [135] R. Alnaizy, A. Akgerman, Adv. Environ. Res., 4 (2000) 233-244.
- [136] E. Grabowska, J. Reszczyńska, A. Zaleska, Water Res., 46 (2012) 5453-5471.
- [137] L.G. Devi, K.E. Rajashekhar, J. Mol. Catal. A: Chem., 334 (2011) 65-76.
- [138] Z. Zhou, H. Wang, Z. Zou, M. Du, J. Guo, Z. Yang, Mater. Res. Bull., 86 (2017) 287-294.

- [139] G.J.A.A. Soler-Illia, A. Louis, C. Sanchez, *Chem. Mater.*, 14 (2002) 750-759.
- [140] L. Robben, A.A. Ismail, D.W. Bahnemann, J.-C. Buhl, *Micropor. Mesopor. Mat.*, 143 (2011) 277-283.
- [141] K.S. Sing, D.H. Everett, R.A.W. Haul, L. Moscou, R.A. Pierotti, J. Rouquerol, T. Siemieniewska, *Pure Appl. Chem.*, 57 (1985) 603-619.
- [142] S. Naumov, A. Khokhlov, R. Valiullin, J. Kärger, P.A. Monson, *Phys. Rev. E*, 78 (2008) 060601.
- [143] R. López, R. Gómez, *J. Sol-Gel Sci. Technol.*, 61 (2012) 1-7.
- [144] Y. Cong, J. Zhang, F. Chen, M. Anpo, D. He, *J. Phys. Chem. C*, 111 (2007) 10618-10623.
- [145] F. Dong, W. Zhao, Z. Wu, *Nanotechnology*, 19 (2008) 365607.
- [146] R. Venkatkarthick, D.J. Davidson, S. Vasudevan, G. Sozhan, S. Ravichandran, *ChemistrySelect*, 2 (2017) 288-294.
- [147] T. Hongo, A. Yamazaki, *Microporous Mesoporous Mater.*, 142 (2011) 316-321.
- [148] D. Grosso, G.J.A.A. Soler-Illia, E.L. Crepaldi, F. Cagnol, C. Sinturel, A. Bourgeois, A. Brunet-Bruneau, H. Amenitsch, P.A. Albouy, C. Sanchez, *Chem. Mater.*, 15 (2003) 4562-4570.
- [149] Q. Dai, L. Shi, Y. Luo, J. Blin, D. Li, C. Yuan, B. Su, *J. Photochem. Photobiol., A*, 148 (2002) 295-301.
- [150] H.M. Kao, C.L. Chen, S.W. Chiao, *J. Chin. Chem. Soc.*, 52 (2005) 693-699.
- [151] M. Abdallah, N. Velikova, Y. Ivanova, Y. Dimitriev, *J. Chem. Technol. Metall.*, 48 (2013) 571-576.
- [152] R.G. Chaudhary, H.D. Juneja, R. Pagadala, N.V. Gandhare, M.P. Gharpure, *J. SAUDI. CHEM. SOC.*, 19 (2015) 442-453.
- [153] K.S. Sing, *Pure Appl. Chem.*, 57 (1985) 603-619.
- [154] G. Calleja, D.P. Serrano, R. Sanz, P. Pizarro, A. García, *Ind. Eng. Chem. Res.*, 43 (2004) 2485-2492.
- [155] J.-K. Park, J.-J. Myoung, J.-B. Kyong, H.-K. Kim, *Bull. Korean Chem. Soc.*, 24 (2003) 671-673.
- [156] J. Blanchard, F. Ribot, C. Sanchez, P.-V. Bellot, A. Trokiner, *J. Non-Cryst. Solids*, 265 (2000) 83-97.
- [157] W. Ren, Z. Ai, F. Jia, L. Zhang, X. Fan, Z. Zou, *Appl. Catal., B*, 69 (2007) 138-144.
- [158] M. Dimitrov, R. Ivanova, N. Velinov, J. Henych, M. Slušná, V. Štengl, J. Tolasz, I. Mitov, T. Tsoncheva, *Nano-Structures & Nano-Objects*, 7 (2016) 56-63.

- [159] S. Karnjanakom, A. Bayu, X. Hao, S. Kongparakul, C. Samart, A. Abudula, G. Guan, J. Mol. Catal. A: Chem., (2016).
- [160] G. Pecchi, P. Reyes, T. Lopez, R. Gomez, A. Moreno, J. Fierro, A. Martínez-Arias, J. Sol-Gel Sci. Technol., 27 (2003) 205-214.
- [161] T. Tong, J. Zhang, B. Tian, F. Chen, D. He, J. Hazard. Mater., 155 (2008) 572-579.
- [162] X. Li, P.-L. Yue, C. Kutal, New J. Chem., 27 (2003) 1264-1269.
- [163] M. Graetzel, R.F. Howe, J. Phys. Chem., 94 (1990) 2566-2572.
- [164] R. Janes, L. Knightley, C. Harding, Dyes and pigments, 62 (2004) 199-212.
- [165] C. Adán, A. Bahamonde, M. Fernández-García, A. Martínez-Arias, Appl. Catal., B, 72 (2007) 11-17.
- [166] O. Zuas, H. Budiman, Nano-Micro Letters, 5 (2013) 26-33.
- [167] Q. Wang, R. Jin, M. Zhang, S. Gao, J. Alloys Compd., 690 (2017) 139-144.
- [168] D. Zhang, J. Sol-Gel Sci. Technol., 58 (2011) 312-318.
- [169] M. Zhou, J. Yu, B. Cheng, J. Hazard. Mater., 137 (2006) 1838-1847.
- [170] B. Santara, B. Pal, P. Giri, J. Appl. Phys., 110 (2011) 114322.
- [171] N. Smirnova, I. Petrik, V. Vorobets, G. Kolbasov, A. Eremenko, Nanoscale Res. Lett., 12 (2017) 239.
- [172] T. Umebayashi, T. Yamaki, H. Itoh, K. Asai, J. Phys. Chem. Solids, 63 (2002) 1909-1920.
- [173] G. Liu, L. Wang, H.G. Yang, H.-M. Cheng, G.Q.M. Lu, J. Mater. Chem., 20 (2010) 831-843.
- [174] E. Grabowska, J. Reszczyńska, A. Zaleska, Water Res., 46 (2012) 5453-5471.
- [175] C.M. Teh, A.R. Mohamed, J. Alloys Compd., 509 (2011) 1648-1660.
- [176] W. Choi, A. Termin, M.R. Hoffmann, J. Phys. Chem., 98 (1994) 13669-13679.
- [177] S. Mozia, M. Tomaszewska, B. Kosowska, B. Grzmil, A.W. Morawski, K. Kałucki, Appl. Catal., B, 55 (2005) 195-200.
- [178] S.M. El-Sheikh, G. Zhang, H.M. El-Hosainy, A.A. Ismail, K.E. O'Shea, P. Falaras, A.G. Kontos, D.D. Dionysiou, J. Hazard. Mater., 280 (2014) 723-733.
- [179] X. Chen, C. Burda, J. Am. Chem. Soc., 130 (2008) 5018-5019.
- [180] F.N. Sayed, O. Jayakumar, R. Sasikala, R. Kadam, S.R. Bharadwaj, L. Kienle, U. Schürmann, S.r. Kaps, R. Adelung, J. Mittal, J. Phys. Chem. C, 116 (2012) 12462-12467.
- [181] J. Wang, D.N. Tafen, J.P. Lewis, Z. Hong, A. Manivannan, M. Zhi, M. Li, N. Wu, J. Am. Chem. Soc., 131 (2009) 12290-12297.

- [182] S.K. Kassahun, Z. Kiflie, D.W. Shin, S.S. Park, W.Y. Jung, Y.R. Chung, *J. Sol-Gel Sci. Technol.*, 82 (2017) 322-334.
- [183] B. Wawrzyniak, A.W. Morawski, B. Tryba, *Int. J. Photoenergy*, 2006 (2006).
- [184] B. Bharti, S. Kumar, H.-N. Lee, R. Kumar, *Scientific Reports*, 6 (2016) 32355.
- [185] M. Kawashita, N. Endo, T. Watanabe, T. Miyazaki, M. Furuya, K. Yokota, Y. Abiko, H. Kanetaka, N. Takahashi, *Colloids and Surfaces B: Biointerfaces*, 145 (2016) 285-290.
- [186] W. Qian, P.A. Greaney, S. Fowler, S.-K. Chiu, A.M. Goforth, J. Jiao, *ACS Sustain. Chem. Eng.*, 2 (2014) 1802-1810.
- [187] Y. Cong, J. Zhang, F. Chen, M. Anpo, *J. Phys. Chem. C*, 111 (2007) 6976-6982.
- [188] R. Asahi, T. Morikawa, T. Ohwaki, K. Aoki, Y. Taga, *science*, 293 (2001) 269-271.
- [189] X. Chen, C. Burda, *J. Phys. Chem. B*, 108 (2004) 15446-15449.
- [190] Y. Choi, T. Umebayashi, M. Yoshikawa, *J. Mater. Sci.*, 39 (2004) 1837-1839.
- [191] J. Trimboli, M. Mottern, H. Verweij, P.K. Dutta, *J. Phys. Chem. B*, 110 (2006) 5647-5654.

Curriculum Vitae

Ahmed Mudhafar Mohammed

Data, Place of Birth 07.11.1979, Mosul, Iraq

Status married, 3 children

Home address

Iraq: Nineveh, Mosul, Al-Sadiq Q. Lane 756, street no.756, house no. 123-33/345

Germany: Rigaer-Str.11, 18107 Rostock

ahmedmudhafar@yahoo.com

Work address

Iraq: Department of Chemistry, College of Education for Girls, University of Mosul

Germany: Leibniz-Institut für Katalyse e.V, Rostock, Germany

Albert-Einstein-Str. 29a, 18059 Rostock

ahmed.mudhafar@catalysis.de

ahmed.mohammed@uni-rostock.de

Academics

1997-2001 B.Sc. chemistry, rank 5th in a class of 44 students

College of Education, University of Mosul, Iraq

2002-2004 M.Sc. in inorganic chemistry

College of Education, University of Mosul, Iraq

2014-2018 PhD student

Leibniz-Institut für Katalyse e.V, Rostock, Germany

Languages

English, German, Arabic (Mother Tongue)

References

Prof. Dr. Peter Langer

Department of Organic Chemistry, Albert-Einstein St. 3a, 18059 Rostock, Germany.
Tel.: +49 (0)381 498 6410, E-mail: peter.langer@uni-rostock.de

Dr. Norbert Steinfeldt

Leibniz-Institut für Katalyse e.V., Albert-Einstein-Str. 29a, 18059 Rostock, Germany.
Tel.: +49 (0)381 1281 319, E-mail: norbert.steinfeldt@catalysis.de

Acknowledgments: 31

Researches

1 - "Preparation and Spectroscopic Characterization of Some Mixed Ligand Complexes of Homodinuclear Co (II), Ni (II) and Cu (II)". Kirkuk University Journal, Scientific Studies, Vol. 4, No. 3, 2009.

2 - "Preparation and studies of a new Schiff base complexes with Co(II), Ni(II) and Cu(II)". Publication in the Journal of Education and Science, Vol. 26, No.3, 2013.

3 - "Preparation of New Complexes of ligand 2- (2-butyl) Thio-5-phenyl-1,3,4-oxadiazole with Studying their Biological Activities". Publication in the Journal Baghdad of Sciences, Vol. 10, No.3, 2013.

4- "Preparation Complexes of ligand 2-cyclohexyl thio-5-phenyl-1,3,4-oxadiazole" (Finished unpublished).

4- "Effect of metal ion addition on structural characteristics and photocatalytic activity of ordered mesoporous titania" (Finished unpublished).

5- "Influence of solvent evaporation step on formation and photo-catalytic properties of mesoporous semi-crystalline titania framework" (Finished unpublished).

Participation in Conferences and Symposia

- 1 - The first Scientific Conference for pure Science held in the College of Science/ university of Kirkuk, 24-25 February 2009.
- 2 - The fourth scientific symposium under the title of “Bio safety in the context of food security” College of Education for Girls, University of Mosul, 8 April 2010.
- 3 - A member of the Preparatory Committee for the Sixth Scientific Symposium held in College of Education for Girls , University of Mosul, 22 September 2011.
- 4 - A member of the Preparatory Committee for the First National Conference of the science of chemistry, which was held in College of Science for Girls, University of Baghdad. 19-20 December 2012.
- 5 - The National Comprehensive Nano Technology , held by the Iraqi Association of Nanotechnology in collaboration research and development department and the University of Technology, 25 December 2012.
- 6 - The Second Women's Conference, which was held at Baghdad University, College of Science for Girls under the title “Women in Science and Iraq”, 26-28 March 2013.
- 7 - 49. Jahrestreffen Deutscher Katalytiker, 16-18 March 2016, Weimar, Germany.
Poster “Preparation , characterization and photocatalytic activity of mesoporous TiO_2 ”.
- 8 - 51. Jahrestreffen Deutscher Katalytiker, 14-16 March 2018, Weimar, Germany.
Poster “Effect of metal ions doping on ordered mesostructure and photoactivity of TiO_2 under UV- irradiation”.
- 9 - 12th International Symposium on the Scientific Bases for the Preparation of Heterogeneous Catalysts, 8-12 July 2018, Louvain-La-Neuve, Belgium. Poster “Influence of solvent evaporation step on formation of mesoporous semi-crystalline titania framework”.